

Microwave and Millimeter-Wave Sensors, Systems and Techniques for Electromagnetic Imaging and Materials Characterization

Guest Editors: Andrea Randazzo,
Kristen M. Donnell, and Yeou Song (Brian) Lee





**Microwave and Millimeter-Wave Sensors,
Systems and Techniques for Electromagnetic
Imaging and Materials Characterization**

**Microwave and Millimeter-Wave Sensors,
Systems and Techniques for Electromagnetic
Imaging and Materials Characterization**

Guest Editors: Andrea Randazzo, Kristen M. Donnell,
and Yeou Song (Brian) Lee



Copyright © 2012 Hindawi Publishing Corporation. All rights reserved.

This is a special issue published in “International Journal of Microwave Science and Technology.” All articles are open access articles distributed under the Creative Commons Attribution License, which permits unrestricted use, distribution, and reproduction in any medium, provided the original work is properly cited.

Editorial Board

Iltcho M. Angelov, Sweden
Herve Aubert, France
Giancarlo Bartolucci, Italy
Tanmay Basak, India
Eric Bergeault, France
Pazhoor V. Bijumon, Canada
Fabrizo Bonani, Italy
Mattia Borgarino, Italy
Maurizio Bozzi, Italy
Nuno Borges Carvalho, Portugal
Robert H. Caverly, USA
Yinchao Chen, USA
Wen-Shan Chen, Taiwan
Carlos E. Christoffersen, Canada
Paolo Colantonio, Italy
Carlos Collado, Spain
Ali Mohamed Darwish, Egypt
Afshin Daryoush, USA
Walter De Raedt, Belgium
Didier J. Decoster, France
Qianqian Fang, USA
Fabio Filicori, Italy
Manuel Freire, Spain
Edward Gebara, USA
Giovanni Ghione, Italy
Ramon Gonzalo, Spain
Gian Luigi Gragnani, Italy
Yong Xin Guo, Singapore
Mridula Gupta, India
Wenlong He, United Kingdom

Tzzy-Sheng Horng, Taiwan
Yasushi Itoh, Japan
Kenji Itoh, Japan
Yong-Woong Jang, Korea
Hideki Kamitsuna, Japan
Nemai Karmakar, Australia
Erik L. Kollberg, Sweden
Igor A. Kossyi, Russia
Slawomir Koziel, Iceland
Miguel Laso, Spain
Chang-Ho Lee, USA
Ernesto Limiti, Italy
Fujiang Lin, Singapore
Yo Shen Lin, Taiwan
Alayn Loayssa, Spain
Giampiero Lovat, Italy
Bruno Maffei, United Kingdom
Gianfranco F. Manes, Italy
Jan-Erik Mueller, Germany
Krishna Naishadham, USA
Kenjiro Nishikawa, Japan
Juan M. O'Callaghan, Spain
Abbas Sayed Omar, Germany
Beatriz Ortega, Spain
Sergio Pacheco, USA
Massimiliano Pieraccini, Italy
Sheila Prasad, USA
Xianming Qing, Singapore
Rdiger Quay, Germany
Mirco Raffetto, Italy

Antonio Raffo, Italy
Murilo A. Romero, Brazil
Luca Roselli, Italy
Arye Rosen, USA
Anders Rydberg, Sweden
Safieddin Safavi-Naeini, Canada
Salvador Sales, Spain
Alberto Santarelli, Italy
Jonathan B. Scott, New Zealand
Almudena Suarez, Spain
Riccardo Tascone, Italy
Smail Tedjini, France
Ichihiko Toyoda, Japan
Samir Trabelsi, USA
Chih Ming Tsai, Taiwan
Giorgio Vannini, Italy
Borja Vidal, Spain
Nakita Vodjdani, France
Jan Vrba, Czech Republic
Chien-Jen Wang, Taiwan
Huei Wang, Taiwan
Jean Pierre Wigner, France
Yong-Zhong Xiong, Singapore
Yansheng Xu, Canada
M. C E Yagoub, Canada
Kamya Y. Yazdandoost, Japan
Ning Hua Zhu, China
Herbert Zirath, Sweden

Contents

Microwave and Millimeter-Wave Sensors, Systems and Techniques for Electromagnetic Imaging and Materials Characterization, Andrea Randazzo, Kristen M. Donnell, and Yeou Song (Brian) Lee
Volume 2012, Article ID 132136, 2 pages

Swarm Optimization Methods in Microwave Imaging, Andrea Randazzo
Volume 2012, Article ID 491713, 12 pages

Wide Range Temperature Sensors Based on One-Dimensional Photonic Crystal with a Single Defect, Arun Kumar, Vipin Kumar, B. Suthar, A. Bhargava, Kh. S. Singh, and S. P. Ojha
Volume 2012, Article ID 182793, 5 pages

Complex Permittivity Measurements of Textiles and Leather in a Free Space: An Angular-Invariant Approach, B. Kapilevich, B. Litvak, M. Anisimov, D. Hardon, and Y. Pinhasi
Volume 2012, Article ID 375601, 7 pages

Buried Object Detection by an Inexact Newton Method Applied to Nonlinear Inverse Scattering, Matteo Pastorino and Andrea Randazzo
Volume 2012, Article ID 637301, 7 pages

Location and Shape Reconstruction of 2D Dielectric Objects by Means of a Closed-Form Method: Preliminary Experimental Results, Gian Luigi Gragnani and Maurizio Diaz Mendez
Volume 2012, Article ID 801324, 10 pages

Editorial

Microwave and Millimeter-Wave Sensors, Systems, and Techniques for Electromagnetic Imaging and Materials Characterization

Andrea Randazzo,¹ Kristen M. Donnell,² and Yeou Song (Brian) Lee³

¹ Applied Electromagnetics Group, Department of Naval, Electrical, Electronic, and Telecommunication Engineering, University of Genoa, 16145 Genoa, Italy

² Applied Microwave Nondestructive Testing Laboratory (amntl), Department of Electrical and Computer Engineering, Missouri University of Science and Technology, Rolla, MO 65409, USA

³ Department of Quality, Anritsu Company, Morgan Hill, CA 95037, USA

Correspondence should be addressed to Andrea Randazzo, andrea.randazzo@unige.it

Received 24 October 2012; Accepted 24 October 2012

Copyright © 2012 Andrea Randazzo et al. This is an open access article distributed under the Creative Commons Attribution License, which permits unrestricted use, distribution, and reproduction in any medium, provided the original work is properly cited.

Microwave and millimeter-wave sensors, systems, and techniques have been acquiring an ever-growing importance in the field of imaging and materials characterization. This interest is primarily motivated by the many advantages of microwaves and millimeter waves. First of all, these systems are capable of directly measuring quantities related to dielectric properties of inspected objects. Furthermore, nowadays microwave and millimeter-wave instrumentation is relatively low cost, especially with respect to other systems (e.g., X-rays). These systems are also relatively compact, allowing portability of the devices and consequently the possibility of performing in-situ measurements. Moreover, the systems are safe to the user as a result of the low transmission energy required for performing the inspection and the nonhazardous behavior of the radiation in the microwave and millimeter-wave frequency bands.

In recent years, several systems and techniques have been proposed in the scientific literature for electromagnetic imaging and materials characterization. Several applicative fields have been explored (e.g., nondestructive testing, biomedical imaging, and subsurface sensing), and novel solutions have been proposed. However, innovative apparatuses still must be developed, in order to mitigate the drawbacks of existing systems and to provide ever better measurement capabilities. Moreover, since the underlying mathematical model is commonly nonlinear and ill posed, novel solution algorithms and processing paradigms are

needed for extracting key information from the measured data and for presenting the inspection results to nontechnical users/personnel of these assessment systems.

This special issue reports state-of-the-art contributions to the research in this field, which consider different aspects and problems related to sensors, systems, and techniques applied to microwave and millimeter-wave imaging.

In the paper “*Wide range temperature sensors based on one-dimensional photonic crystal with a single defect*” by A. Kumar et al., the transmission characteristics of a one-dimensional photonic crystal structure with a defect have been studied. The authors analyzed the behavior of the refractive index as a function of temperature of the medium. It has been found that the average shift in central wavelength of defect modes can be utilized in the design of a temperature sensor.

The paper “*Complex permittivity measurements of textiles and leather in a free space: an angular-invariant approach*” by B. Kapilevich et al. describes a system for complex permittivity measurements of textiles and leathers in a free space at 330 GHz. The role of Rayleigh scattering is considered, and the incidence-angular invariance has been estimated experimentally. It has been found that if the incidence angle exceeds the angular-invariant limit of about 25–30 degrees, the uncertainty caused by the Rayleigh scattering drastically increases, thus, preventing accurate measurements of the real and imaginary parts of the dielectric properties.

In “*Buried object detection by an inexact newton method applied to nonlinear inverse scattering*” by M. Pastorino and A. Randazzo, an algorithm for buried object detection is proposed. The method is based on the regularized solution of the full nonlinear inverse scattering problem formulated in terms of integral equations involving the Green’s function for half-space geometries. An efficient two-step inexact Newton algorithm is employed. Capabilities and limitations of the method are evaluated by means of numerical simulations.

In “*Location and shape reconstruction of 2d dielectric objects by means of a closed-form method: preliminary experimental results*” by G. L. Gragnani and M. D. Mendez, an analytical approach for the identification of the location and shape of dielectric targets, starting from microwave measurements, is considered. A closed-form singular value decomposition of the scattering integral operator is derived and is used for determining the radiating components of the equivalent source density. The capabilities of the approach are demonstrated by considering real scattering data belonging to the Fresnel database. As a result of the closed-form solution, very short computational times have been obtained.

Finally, the application of swarm optimization methods to microwave imaging is reviewed in the paper “*Swarm optimization methods in microwave imaging*” by A. Randazzo. Swarm optimization methods are recently proposed stochastic algorithms inspired by the collective social behavior of natural entities (e.g., birds, ants, etc.). These algorithms have been proven to be quite effective in several applicative fields, such as intelligent routing, image processing, antenna synthesis, component design, and, clearly, microwave imaging. Recent approaches based on swarm methods are reviewed and critically discussed.

We wish to thank all the authors for their important contributions, the reviewers for their valuable suggestions, and the Editorial Board and Publisher for their fundamental support in the publication of this special issue.

*Andrea Randazzo
Kristen M. Donnell
Yeou Song (Brian) Lee*

Review Article

Swarm Optimization Methods in Microwave Imaging

Andrea Randazzo

Department of Naval, Electrical, Electronic, and Telecommunication Engineering, University of Genoa, Via Opera Pia 11A, 16145 Genova, Italy

Correspondence should be addressed to Andrea Randazzo, randazzo@dibe.unige.it

Received 8 August 2012; Accepted 21 September 2012

Academic Editor: Kristen M. Donnell

Copyright © 2012 Andrea Randazzo. This is an open access article distributed under the Creative Commons Attribution License, which permits unrestricted use, distribution, and reproduction in any medium, provided the original work is properly cited.

Swarm intelligence denotes a class of new stochastic algorithms inspired by the collective social behavior of natural entities (e.g., birds, ants, etc.). Such approaches have been proven to be quite effective in several applicative fields, ranging from intelligent routing to image processing. In the last years, they have also been successfully applied in electromagnetics, especially for antenna synthesis, component design, and microwave imaging. In this paper, the application of swarm optimization methods to microwave imaging is discussed, and some recent imaging approaches based on such methods are critically reviewed.

1. Introduction

Microwave imaging denotes a class of noninvasive techniques for the retrieval of information about unknown conducting/dielectric objects starting from samples of the electromagnetic field they scatter when illuminated by one or more external microwave sources [1]. Such techniques have been acquiring an ever growing interest thanks to their ability of directly retrieving the distributions of the dielectric properties of targets in a safe way (i.e., with nonionizing radiation) and with quite inexpensive apparatuses. In recent years, several works concerned those systems. In particular, their ability to provide excellent diagnostic capabilities has been assessed in several areas, including civil and industrial engineering [2], nondestructive testing and evaluation (NDT&E) [3], geophysical prospecting [4], and biomedical engineering [5].

The development of effective reconstruction procedures is, however, still a quite difficult task. The main difficulties are related to the underlying mathematical problem. In fact, the information about the target are contained in a complex way inside the scattered electric field. In particular, the governing equations turn out to be highly nonlinear and strongly ill posed. Consequently, inversion procedures are usually quite complex and time consuming, especially when high resolution images are needed.

In the literature several approaches have been proposed for solving this problem. In particular, two main classes of algorithms can be identified. Deterministic [6–21] and stochastic strategies [22–33]. Deterministic methods are usually fast and, when converge, they produce high quality reconstructions. However, their main drawback is that they are local approaches, that is, they usually require to be started with an initial guess “near” enough to the correct solution. Otherwise, such approaches can be trapped in local minima corresponding to false solutions. Moreover, in most cases, it is difficult to introduce a priori information in the reconstruction process. On the contrary, stochastic approaches are global optimization methods, that is, they are able to find the global solution of the problem. Furthermore, thanks to their flexibility, they usually easily allow the introduction of a priori information on the unknowns. The main drawback of this class of approaches is their computational burden. However, it should be noted that with the recent growth of computational resources, it can be envisioned that future generation computers will allow faster reconstructions.

Stochastic approaches are usually based on a population of trial solutions that is iteratively updated. Depending on how the population is modified at each iteration, different class of methods can be identified. The “classical” approaches

have been developed in order to simulate the evolutionary processes of biological entities. Such kind of methods are now very common in several areas of electromagnetic engineering and, in particular, in nondestructive testing and imaging. Among them, the most successful ones are the genetic algorithm (GA) [34] and the differential evolution (DE) method [35].

A new class of stochastic approaches has been recently introduced by mimicking the collective behavior of real entities such as particles, birds, and ants. Such approaches, usually referred as swarm methods [36, 37], have been proven to be quite effective in several applications, where they outperform standard evolutionary methods. Recently, they are becoming very popular in electromagnetics, too. Several applications, ranging from antenna synthesis to microwave component design, have been proposed in the literature. Moreover, several different approaches, such as the particle swarm optimization (PSO) [38, 39] and the ant colony algorithm (ACO) [40, 41], have been successfully applied to microwave imaging.

In the present paper, the application of swarm algorithms to microwave imaging is discussed, and some of the recent literature results are critically reviewed. The paper is organized as follows. In Section 2, the mathematical framework of optimization problems for microwave imaging is briefly recalled. Section 3 describes the considered swarm methods. Section 4 reviews the applications of such algorithms in the framework of microwave imaging. Finally, conclusions are drawn in Section 5.

2. Microwave Imaging as an Optimization Problem

Microwave imaging approaches aim at retrieving information about unknown objects (e.g., the full distribution of dielectric properties, the shape in the case of conducting targets, the position and size of an inclusion, etc.) starting from measures of the electromagnetic field, they scatter when illuminated by a known incident electric field.

Despite different equations are needed for modeling different problems (e.g., two-dimensional or three-dimensional problems, dielectric or perfectly conducting objects, and so on), it is usually possible to write a relationship between the desired unknown quantities and the measured field (at least in implicit form), that is, an equation of the form

$$F(x) = e, \quad (1)$$

where x is the unknown function describing the searched features of the object (e.g., $x = \epsilon_r$ when dealing with the reconstruction of the distribution of the dielectric permittivity), and e is the measured (vector or scalar) electric field, that is, the known data of the equation. Consequently, the inverse problem can be recast as an optimization problem by defining a cost function of the form

$$f(x) = w \|e - F(x)\|_2^2, \quad (2)$$

where w is a constant normalization parameter. In (2), the standard Euclidean 2-norm has been considered. This is

often a common choice in microwave imaging and allows the use of widely studied mathematical tools for the analysis of the convergence and regularization behaviors. However, different norms have been recently proposed, too (e.g., the norm of L^p Banach spaces [42]).

For illustrative purposes, the case of cylindrical dielectric targets embedded in free space is explicitly described in the following. The cylinder axis is assumed to be parallel to the z -axis. A time-harmonic (with angular frequency ω) transverse magnetic (TM) incident field is assumed. Similar expressions can be derived for other configurations (e.g., half-space and multilayer media, three-dimensional vector problems, etc.).

When dealing with inhomogeneous dielectric objects embedded in an infinite and homogeneous medium, the electromagnetic inverse scattering problem is governed by the following two operator equations [1]:

$$\begin{aligned} e_{\text{scatt}}(\mathbf{r}) &= G_{\text{ext}}(ce_{\text{tot}})(\mathbf{r}), \quad \mathbf{r} \in D_{\text{obs}}, \\ e_{\text{inc}}(\mathbf{r}) &= e_{\text{tot}}(\mathbf{r}) - G_{\text{int}}(ce_{\text{tot}})(\mathbf{r}), \quad \mathbf{r} \in D_{\text{inv}}, \end{aligned} \quad (3)$$

where $G_{\text{ext}}(\cdot)(\mathbf{r}) = -k^2 \int_{D_{\text{inv}}}(\cdot)g_0(\mathbf{r},\mathbf{r}')d\mathbf{r}'$, $\mathbf{r} \in D_{\text{obs}}$ (being D_{obs} the observation domain where the scattered electric field is collected), and $G_{\text{int}}(\cdot)(\mathbf{r}) = -k^2 \int_{D_{\text{inv}}}(\cdot)g_0(\mathbf{r},\mathbf{r}')d\mathbf{r}'$, $\mathbf{r} \in D_{\text{inv}}$ (being D_{inv} the investigation area where the target is located), are data and state operators whose kernel is the free-space Green's function g_0 (being $k = \omega\sqrt{\epsilon_0\mu_0}$ the free-space wavenumber), $c(\mathbf{r}) = \epsilon_r(\mathbf{r}) - 1$ is the contrast function (being ϵ_r the space dependent relative complex dielectric permittivity of the investigation area D_{inv}), e_{inc} and e_{tot} are the z -components of the incident and total electric fields inside the investigation area, and e_{scatt} is the z -component of the scattered electric field in the points of the observation domain D_{obs} [1].

In discrete setting, the two equations in (3) can be replaced by the following matrix equations:

$$\begin{aligned} \mathbf{e}_{\text{scatt}} &= \mathbf{G}_{\text{ext}} \text{diag}(\mathbf{c})\mathbf{e}_{\text{tot}}, \\ \mathbf{e}_{\text{inc}} &= \mathbf{e}_{\text{tot}} - \mathbf{G}_{\text{int}} \text{diag}(\mathbf{c})\mathbf{e}_{\text{tot}}, \end{aligned} \quad (4)$$

where \mathbf{c} is an array containing the N unknown coefficients of the expansion of c in a given set of basis functions, \mathbf{e}_{inc} and \mathbf{e}_{tot} are arrays of dimensions N containing the coefficients of the incident and total electric fields, and $\mathbf{e}_{\text{scatt}}$ is an array of M elements containing the coefficients used to represent the known scattered field in the measurement domain.

As in the continuous case, the equations in (4) represent an ill-conditioned nonlinear problem. Directly solving this problem is very difficult. However, as previously introduced, it is possible to recast its solution as the minimization of a proper cost function. Usually, the following functional is considered

$$\begin{aligned} f(\mathbf{x}) &= w_D \|\mathbf{e}_{\text{scatt}} - \mathbf{G}_{\text{ext}} \text{diag}(\mathbf{c})\mathbf{e}_{\text{tot}}\|_2^2 \\ &+ w_S \|\mathbf{e}_{\text{inc}} - \mathbf{e}_{\text{tot}} + \mathbf{G}_{\text{int}} \text{diag}(\mathbf{c})\mathbf{e}_{\text{tot}}\|_2^2, \end{aligned} \quad (5)$$

where w_D and w_S are weighting parameters, often chosen equal to $w_D = \|\mathbf{e}_{\text{scatt}}\|_2^{-2}$ and $w_S = \|\mathbf{e}_{\text{inc}}\|_2^{-2}$. In this case, the unknown array \mathbf{x} is composed by the elements of \mathbf{c} and \mathbf{e}_{tot} .

Clearly, other forms can be used, too. For example, the two equations can be combined together in order to obtain the following cost function:

$$f(\mathbf{x}) = w_D \left\| \mathbf{e}_{\text{scatt}} - \mathbf{G}_{\text{ext}} \text{diag}(\mathbf{c})(\mathbf{I} - \mathbf{G}_{\text{int}} \text{diag}(\mathbf{c}))^{-1} \mathbf{e}_{\text{inc}} \right\|_2^2, \quad (6)$$

which has the advantage of considering only the contrast function coefficients as unknowns. As a drawback, it needs a matrix inversion, leading to a high computational cost.

The cost function can be modified by introducing multiview and multifrequency information. In this case, the target is illuminated by several incident fields (e.g., generated by S sources located all around the objects and operating at F different frequencies), and the cost function becomes

$$f(\mathbf{x}) = w_D \sum_{f=1}^F \sum_{s=1}^S \left\| \mathbf{e}_{\text{scatt}}^{f,s} - \mathbf{G}_{\text{ext}}^{f,s} \text{diag}(\mathbf{c}) \mathbf{e}_{\text{tot}}^{f,s} \right\|_2^2 + w_S \sum_{f=1}^F \sum_{s=1}^S \left\| \mathbf{e}_{\text{inc}}^{f,s} - \mathbf{e}_{\text{tot}}^{f,s} + \mathbf{G}_{\text{int}}^{f,s} \text{diag}(\mathbf{c}) \mathbf{e}_{\text{tot}}^{f,s} \right\|_2^2, \quad (7)$$

where the indexes f and s denote that the corresponding quantities are related to the f th operating frequency and the s th illumination.

3. Swarm Optimization Algorithms

Swarm algorithms belong to the class of optimization methods, that is, they find the minimum of a given cost function $f(x)$. Similarly to other evolutionary approaches, they usually allow reaching the global optimum, thus avoiding to find a suboptimal solution corresponding to a local minima. Moreover, they are able to easily incorporate constraints on the search space. However, while evolutionary algorithms are inspired by the genetic adaptation of organisms, swarm methods exploit their collective social behavior.

In order to define a general framework for swarm methods, let us consider a cost function $f : S \subseteq \mathbb{R}^G \rightarrow [0, +\infty)$ to be minimized (or maximized). For sake of simplicity, the case of bound constraints (i.e., $l_g \leq x_g \leq u_g$, being l_g and u_g the lower and upper bounds on the g th component of \mathbf{x}) is considered in the following. However, the unknown array $\mathbf{x} = [x_1, x_2, \dots, x_G]^t \in S \subseteq \mathbb{R}^G$ can be subjected to arbitrary constraints.

Swarm algorithms are usually iterative methods based on a population of P trial solutions $\mathcal{P}_k = \{\mathbf{x}_p^{(k)}, p = 1, \dots, P\}$ (being k the iteration number) representing P agents inspired from real world (e.g., particles, birds, ants, etc.). The population is iteratively modified according to rules aimed at mimicking the natural behavior of those agents.

In the framework of electromagnetic imaging, the following swarm algorithms have been mainly considered.

- (i) Particle swarm optimization.
- (ii) Ant colony optimization.
- (iii) Artificial bee colony optimization.

Apart from the standard approaches, hybridization with other methods (e.g., local optimization methods, other evolutionary approaches, machine learning algorithms, etc.) has also been proposed in the literature.

In the following sections, some information about the basic versions of those methods are briefly recalled.

3.1. Particle Swarm Optimization (PSO). PSO is inspired by the behavior of flocks of birds and shoals of fish [38, 39]. Each entity moves through the space of solutions with a velocity that is related to the locations and cost function values of the members of the swarm. In particular, the basic PSO algorithm [38] considers a set of $p = 1, \dots, P$ “particles” characterized, at each iteration k , by their positions $\mathbf{x}_p^{(k)}$ and velocity $\mathbf{v}_p^{(k)}$. If no a priori information is available, usually the algorithm is initialized by using random values, that is,

$$\begin{aligned} \mathbf{x}_{p,g}^{(0)} &= l_g + (u_g - l_g) U(0, 1), \\ \mathbf{v}_{p,g}^{(0)} &= l_g^v + (u_g^v - l_g^v) U(0, 1), \\ g &= 1, \dots, G, \quad p = 1, \dots, P, \end{aligned} \quad (8)$$

where l_g and u_g are the lower and upper bounds for the g th component of particles’ positions, l_g^v and u_g^v are the lower and upper bounds for the g th component of the particles’ velocities, and $U(0, 1)$ is a function returning a random variable uniformly distributed between 0 and 1. Clearly, if some a priori information is available, the initialization scheme can be modified for taking it into account (e.g., in microwave imaging, when the aim is the identification of one or more localized objects, it is possible to generate random targets and use them as starting random solutions).

The trial solutions are iteratively updated by using the following two-step scheme (as also shown in the flow chart in Figure 1):

$$\begin{aligned} \mathbf{v}_p^{(k+1)} &= \omega^{(k)} \mathbf{v}_p^{(k)} + \eta_1 U(0, 1) (\mathbf{p}_p - \mathbf{x}_p^{(k)}) \\ &\quad + \eta_2 U(0, 1) (\mathbf{g} - \mathbf{x}_p^{(k)}), \\ \mathbf{x}_p^{(k+1)} &= \mathbf{x}_p^{(k)} + \mathbf{v}_p^{(k)}, \end{aligned} \quad (9)$$

where $\omega^{(k)}$ is the inertia parameter, η_1 and η_2 are acceleration coefficients, and \mathbf{p}_p and \mathbf{g} are the best solution achieved by the p th particle and by the whole swarm so far, respectively. The two acceleration terms in the velocity update can be thought as two elastic forces with random magnitude attracting the particles to the best solutions achieved so far by each entity and by the whole swarm, respectively. After the new solutions are generated the values of \mathbf{p}_p and \mathbf{g} are updated.

The procedure is iterated until some predefined stopping criteria is fulfilled. In particular, the stopping criteria can be composed by several conditions. Some of the most commonly used are the following.

- (i) Maximum number of iterations: the method is stopped when a given number of iteration k_{max} is reached.

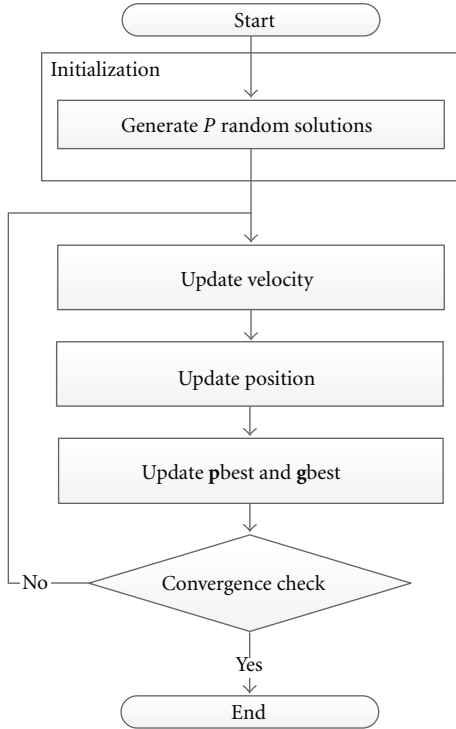
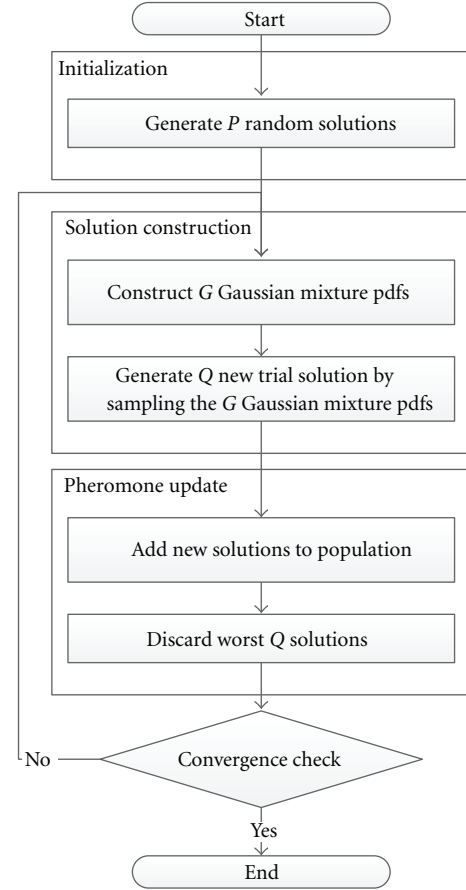


FIGURE 1: Flow chart of the PSO algorithm.

- (ii) Cost function threshold: the method is stopped when the value of cost function of the best trial solution falls below a given threshold f_{th} .
- (iii) Cost function improvement threshold: the method is stopped if the improvement of the cost function of the best individual after k_{th} iterations is below a fixed threshold Δf_{th} .

3.2. Ant Colony Optimization. Ant colony optimization (ACO) is a recently developed swarm optimization method based on the behavior of ants, and, in particular, on how they find the optimal path for reaching the food starting from their nest [40]. Initially, ants explore the area around their nest in a random manner searching for food. When a food source is found, ants evaluate it and bring back some food to the nest depositing a pheromone trail on the ground during the trip. The amount of pheromone depends on the quantity and quality of the food, and it is used to guide other ants to the food source. It has been found that the pheromone trails allow ants to find the shortest path between nest and food sources. On the basis of such behavior, ACO was initially designed for solving hard combinatorial problems, such as the traveling salesman problem [41]. Successively, the original algorithm has been extended for considering different applications. In particular, several efforts have been devoted to the extension to continuous domains, and some different versions of the algorithm have been proposed [43–45]. In the following, the $ACO_{\mathbb{R}}$ version [46] is described. Such algorithm can be considered as composed by three functional blocks, as shown in Figure 2: initialization, solution construction, and

FIGURE 2: Flow chart of the $ACO_{\mathbb{R}}$ algorithm.

pheromone update. The algorithm iterates until a predefined stopping criteria is satisfied.

In the initialization block, the initial population $\mathcal{P}_0 = \{\mathbf{x}_p^{(0)}, p = 1, \dots, P\}$ is created by generating P random trial solutions $\mathbf{x}_p^{(0)} = [x_{p,1}^{(0)}, \dots, x_{p,G}^{(0)}]^t$. Similarly to the PSO algorithm, when no a priori information is available and assuming boundary constraints, the g th components of the p th trial solution are generated by sampling a uniform distribution as defined in (8). In this case, too, if additional a priori information is available, it can be included in the initialization procedure.

The solution construction block is used to generate new trial solutions. In particular, at the k th iteration, Q new solutions $\tilde{\mathbf{x}}_q^{(k)}$, $q = 1, \dots, Q$ are generated by sampling a set of Gaussian mixture probability density functions. In particular, the probability density function of the g th component is built as

$$G_g^{(k)}(x) = \sum_{p=1}^P w_p \frac{1}{s_{p,g}^{(k)} \sqrt{2\pi}} e^{-\frac{(x - m_{p,g}^{(k)})^2}{2(s_{p,g}^{(k)})^2}}, \quad (10)$$

where the weighting parameters w_p , $p = 1, \dots, P$, are given by

$$w_p = \frac{1}{\rho P \sqrt{2\pi}} e^{-(p-1)^2 / 2\rho^2 P^2}, \quad p = 1, \dots, P, \quad (11)$$

and the mean, $m_{p,g}^{(k)}$, and standard deviation, $s_{p,g}^{(k)}$, of the Gaussian kernels are given by

$$m_{p,g}^{(k)} = x_{p,g}^{(k)}, \quad p = 1, \dots, P, g = 1, \dots, G,$$

$$s_{p,g}^{(k)} = \xi \sum_{i=1}^P \frac{|x_{p,g}^{(k)} - x_{i,g}^{(k)}|}{P-1}, \quad p = 1, \dots, P, g = 1, \dots, G. \quad (12)$$

In the previous equations, ρ is the pheromone evaporation rate, and ξ is a scaling parameter. Such quantities are key parameters of the ACO algorithm [46], and the best choice for their values depends on the specific application.

The pheromone update block is responsible of the population update. In particular, two mechanism are used to build the new population \wp_{k+1} of the $(k+1)$ th iteration:

- (i) positive update: a temporary population is created by adding newly created solutions to the solution archive. A pool of $P+Q$ trial solutions $\tilde{\wp}_{k+1} = \{x_{k,p}, p = 1, \dots, P\} \cup \{\tilde{x}_{k,q}, q = 1, \dots, Q\}$ is then obtained,
- (ii) negative update: the worst Q elements of $\tilde{\wp}_{k+1}$ (i.e., those characterized by the higher values of the cost function) are discarded. The remaining P solutions constitute the new population \wp_{k+1} .

In order to speed up this stage, usually the solution archive is ordered on the basis of the cost function, that is, $f(x_{k,1}) \leq f(x_{k,2}) \leq \dots \leq f(x_{k,P})$. The two previous blocks are iteratively applied since some predefined stopping criteria are fulfilled. In this case, too, the stopping criteria can be a combination of several different conditions.

3.3. Artificial Bee Colony Optimization. The artificial bee colony algorithm is a swarm optimization method introduced by Karaboga [47] and Karaboga and Basturk [48] and inspired by the foraging behavior of honey bees. In particular, ABC is based on the model proposed in [49], which defines two main self-organizing and collective intelligence behaviors: recruitment of foragers for working on rich food sources and abandonment of poor sources. In ABC, a colony of artificial bees search for rich artificial food sources (representing solutions of the considered optimization problem) by iteratively employing the following two strategies: movement towards better solutions by means of a neighbor search mechanism and abandonment of poor solutions that cannot be further improved.

In the following, an artificial colony, composed by C entities, is considered. Bees can be classified in three groups: employed (i.e., already working on a known food source), onlooker (i.e., waiting for a food source), and scout (i.e., randomly searching for new sources) bees. The trial solutions are the food sources associated with the employed bees. Let us denote by P the number of employed bees (corresponding to the number of trial solutions). Often, such number is set equal to $P = C/2$, and the number of onlooker bees is chosen equal to P . A block diagram of the method is shown in Figure 3.

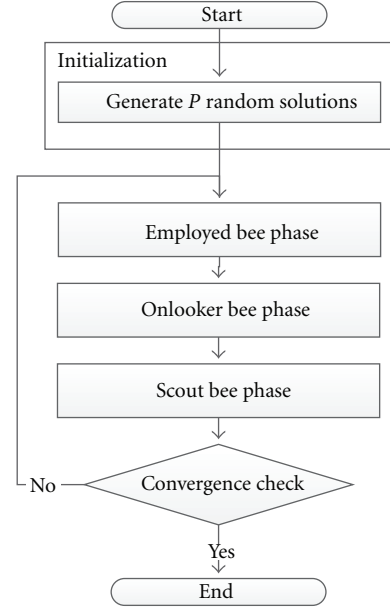


FIGURE 3: Flow chart of the ABC algorithm.

In the initialization phase, the P trial solution are randomly generated, for example, by using a relationship similar to that in (8). The cost function of all trial solutions is evaluated and stored. In the employed bee phase, the employed bees modify their trial solutions according to

$$x_{p,g}^{(k+1)} = x_{p,g}^{(k)} + U(0,1)(x_{p,g}^{(k)} - x_{h,g}^{(k)}), \quad (13)$$

where g and h are randomly chosen.

In the onlooker bee phase, each onlooker bee select a food source in a probabilistic way. In particular, the probability of choosing the p th food source is given by

$$p_p = \frac{f_{\text{fit}}(\mathbf{x}_p^{(k)})}{\sum_{p=1}^P f_{\text{fit}}(\mathbf{x}_p^{(k)})}, \quad (14)$$

where f_{fit} is a fitness function defined as $f_{\text{fit}}(\mathbf{x}) = 1/(f(\mathbf{x})+1)$. The food sources selected by the onlooker bees are further improved by using (13).

If a food source is not improved after a predefined number of iterations K_{lim} (food source limit), that is, $f(\mathbf{x}_p^{(k)}) \geq f(\mathbf{x}_p^{(k-q)})$ for $q = 1, \dots, K_{\text{lim}}$, it is abandoned by its employed bee. Such bee becomes a scout bee and starts searching for a new food source randomly. Consequently, in the scout bee phase, employed bees working on abandoned sources generate new trial solution in a random way (i.e., by using the same relationship used in the initialization phase). After a new solution is found, the scout bees are reverted to employed bees, and they start working on the new food sources. Clearly, at the beginning of the optimization process, no scout bees are present and consequently, for the first iterations, only the solutions initially discovered in the initialization phase are processed.

TABLE 1: Overview of swarm algorithms applications in microwave imaging.

Object type	Material	Illumination type	Method	Reference
1D profile	Dielectric	Time domain	PSO	[50–52]
2D cylinders	Dielectric	Time domain	PSO	[53, 54]
2D cylinders	Dielectric	Single frequency	PSO	[55–58]
2D cylinders	PEC	Single frequency	PSO	[59, 60]
3D objects	Dielectric	Single frequency	PSO	[58, 61]
3D objects	Dielectric	Single frequency	μ PSO	[62]
2D cylinders	Dielectric	Time domain	APSO	[63]
2D cylinders	PEC	Time domain	APSO	[64, 65]
2D cylinders	PEC	Single frequency	PSO-SA	[66]
2D cylinders	Dielectric	Single frequency	HSPO	[67]
2D cylinders	Dielectric	Single frequency	PSO-RBF	[68]
2D cylinders	Dielectric	Single frequency	IMSA-PSO	[69–73]
3D objects	Dielectric	Single frequency	IMSA-PSO	[74, 75]
2D cylinders	Dielectric	Single frequency	ACO	[28, 76]
2D cylinders	Dielectric	Single frequency	ACO-LSM	[77]
3D objects	Dielectric	Single frequency	ACO-LSM	[78, 79]
3D objects	Dielectric	Time domain	ABC	[80]
2D cylinders	Dielectric	Single frequency	ABC	This paper

4. Application of Swarm Optimization to Microwave Imaging

Swarm algorithms have been used for solving different types of microwave imaging problems. In particular, two-dimensional and three-dimensional dielectric and PEC targets have been considered in the literature. Moreover, both single-frequency, multifrequency, and time-domain incident radiation has been used. An overview of papers proposing swarm optimization methods in microwave imaging is given in Table 1. Specific details are provided in the following sections.

4.1. PSO. PSO has been extensively used in electromagnetic problems [39]. Several works proposed PSO, also with enhancement to the standard algorithm, for microwave imaging problems. In [50, 51], the reconstruction of one-dimensional dielectric profiles, illuminated by a Gaussian pulse (plane waves are assumed), is considered. Both noiseless and noisy data have been used. Two size of the populations are considered equal and twice the number of unknowns. The acceleration coefficients of the PSO are $\eta_1 = \eta_2 = 0.5$, and the inertia parameters is initially set to 1 and decreased linearly to 0.7 in 500 iterations (maximum number of iterations). A comparison with the DE is also provided. In the reported numerical results, the PSO shows slightly better convergence rate, but the DE allows obtaining a more precise reconstruction. A similar approach is proposed in [52], too.

In [53], the authors propose the use of the PSO for the localization of dielectric circular cylinders under a TM time-domain formulation. The unknowns are the position, size, and dielectric properties of the target. Good reconstructions are obtained by using five particles.

In [54], the reconstruction of homogeneous dielectric cylinders is considered. The external shape of the cylinder is described by using a spline representation. The unknowns are the parameters of the spline and the dielectric permittivity. The proposed approach is able to reconstruct such quantities with errors less than about 7% (shape) and 3% (permittivity) for signal-to-noise ratio above 10 dB.

In [55], the reconstruction of the distribution of the relative dielectric permittivity of 2D dielectric structures is concerned. A single-frequency multiview TM illumination is considered. The cost function defined in (7) is used. A population size of twice the unknowns number is used; the acceleration coefficients are randomly generated in the range $[0, 2]$, and the inertia parameter is set equal to 0.4. The reported results show that the PSO is able to provide good reconstruction of the considered objects. Moreover, comparisons with a genetic algorithm and with the conjugate gradient (CG) method are provided. For the considered case, PSO outperforms both GA and CG (the mean relative reconstruction errors are 1.7%, 1.8%, and 5.7%, resp.). A similar approach is proposed in [56], too, providing similar conclusions. In [57], the PSO is used to find the parameters of a crack in the outer layer of a two-layer dielectric cylinder. The direct solver is based on a finite difference frequency Domain (FDFD) scheme. Good agreements are obtained for several positions of the cracks. The same approach is also applied in [58] to the detection of a tumor inside a model of breast. Both 2D and 3D simplified configurations are assumed. The unknowns are the position and shape of the malignant inclusion.

The reconstruction of the shape of PEC cylinders is considered in [59, 60]. A cubic-spline-based representation is used for defining the shape of the cylinder. The target

is illuminated by TM waves impinging from 7 directions uniformly distributed around it and, for each illumination, the scattered field is collected in 32 points. Single-frequency operation is assumed. The maximum radius is approximately 1.5λ (being λ the wavelength in the background medium). Under such assumptions, good reconstructions have been obtained by considering 10 control points for the splines, $\eta_1 = \eta_2 = 0.5$, and population sizes ranging from 10 to 60. The inertia is initialized to 1.0 and decreased to 0.7 after 200 iterations (maximum number of iterations). A comparison with DE is also performed. Both algorithms provide good results, although DE, for the considered cases, usually produces lower values of the cost function and of the reconstruction error.

In [61], 3D objects are reconstructed. The measurement configuration simulates those employed for breast cancer detection, that is, four circular arrays of 36 antennas are located around a cubic investigation domain. In this reference, the PSO-based approach is able to retrieve a small centered inclusions.

In [62], a μ PSO algorithm is proposed for tackling the high dimensionality of the microwave imaging problems. Satisfactory reconstructions are obtained in the reconstruction of a 3D model of breast with a malignant inclusion by using only 5 particles. Comparisons with the standard PSO (with swarm size of 25 particles) show that the new approach is able to obtain comparable results, but with a smaller population size.

In [63], an asynchronous PSO (APSO) is proposed for the reconstruction of the location, shape, and permittivity of a dielectric cylinder illuminated by TM pulses. The direct solver is based on a finite difference time-domain (FDTD) scheme. The main difference with respect to the standard PSO is the population updating mechanism. In the APSO, the new best position is computed after every particle update, and it is used in the following updates immediately. Consequently, the swarm reacts more quickly. The same approach is used in [64, 65] for the identification of the shape of PEC cylinders in free space and inside a dielectric slab. In such cases, the APSO is able to correctly identify the shape of the targets with an error of about 5% (in presence of noise on the data) and it shows better performance with respect to standard PSO.

Some hybrid versions of the PSO have also been proposed in the literature. In [66], PSO is combined with simulated annealing (SA) for exploiting the exploration properties of PSO and the exploitation ability of SA. The reported results concern the reconstruction of the external shape of a cylinder under multiview TM illumination and show that the hybrid approach allows reaching better results than the standard one (reconstructions errors were 0.0014 and 0.072, resp.). In [67], a hybrid PSO (HPSO) is used for reconstructing dielectric cylinders under TM illuminations. The difference from the standard PSO is mainly related to the use of a particle swarm crossover for enhancing trial solutions. In [68], the PSO is combined with radial basis function (RBF) networks. In particular, the RBF is used to obtain an estimate of the dielectric properties of two-dimensional cylinders under single-frequency TM illumination. The PSO is employed to

efficiently training the RBF starting from a set of simulated configurations.

In [69–71], an integrated multiscale approach (IMSA) relying upon PSO is presented. In such technique, the investigation area is iteratively reconstructed at different scales. At every scale, the PSO is used to obtain a quantitative reconstruction of the distribution of the dielectric properties. A clustering techniques is used to identify the scatterers, and then the investigation area is refined in order to focus only on the objects. The proposed approach is tested by using several different two-dimensional targets illuminated by monochromatic TM incident waves. The reported results confirm that the integrated strategy is able to outperform its standard counterpart. Moreover, the new approach is also able to provide better results than those obtained by using the CG and GA (both in their standard form and inserted in a IMSA framework). As an example, a square hollow cylinder ($\epsilon_r = 1.5$, sides $L_{in} = 0.8\lambda$ and $L_{out} = 1.6\lambda$) contained in an investigation area of side 2.4λ and illuminated by plane waves impinging from 4 different directions (with the electric field measured in 21 points located on a circumference of radius 1.8λ for every view) is efficiently reconstructed in 4 steps. At each step, the PSO is executed with 20 particles, $\eta_1 = \eta_2 = 2.0$, $\omega^{(k)} = 0.4$, and $k_{max} = 2000$ (the mesh used to discretized the investigation area has size 36). The obtained reconstruction error is 3.8%. For the same configuration, the multiscale version of CG provides an error of 4.6%. An experimental validation with the Fresnel data [81] is also provided, confirming the capabilities of the approach when working in real environments. In [72, 73], the IMSA-PSO is tested on phaseless data (i.e., amplitude-only scattered field measures are available). In this case, too, good agreement with the actual profile are obtained. In [74, 75], the IMSA-PSO is also extended to the reconstruction of 3D objects.

4.2. Ant Colony Optimization-Based Imaging Algorithms. ACO has been used in several electromagnetic applications, in particular for design of antennas and microwave components [82, 83], for the allocation of base stations [84], and for microwave imaging. Concerning electromagnetic imaging, ACO has been applied both to the reconstruction of 2D cylindrical structures and 3D objects.

In [76], the ACO algorithm is applied to the reconstruction of multiple dielectric lossless cylinders under TM illumination. A two-dimensional formulation is assumed. Two representations of the dielectric properties are considered, pixelbased and splinebased. The number of unknowns, in the two cases, are 256 and 169, respectively. The population size is set equal to the number of unknowns and, at every iteration, $Q = P/10$ new solutions are created. The parameters of the ACO are set equal to $\rho = 0.1$ and $\xi = 0.85$ (according to the suggestions available in the literature). The iterations are stopped when a maximum number of iterations, $k_{max} = 2000$, is reached. The provided results show that in all cases the ACO-based approach is able to correctly reconstruct the targets with a mean relative error lower than 5%. Moreover, as expected, the spline representation allows for a faster convergence (thanks to the lower number of unknowns).

In [28], ACO is applied to a similar configuration (two-dimensional imaging of a two-layer dielectric cylinders). A comparison with GA and DE is provided. The reconstruction results show that in the considered case ACO “reaches a more accurate reconstruction than those obtained by the other two methods” and “requires a lower number of function evaluations.”

In [77], a hybrid method is proposed for two-dimensional imaging of multiple homogeneous dielectric targets. First, the shape of the targets is estimated by using the linear sampling method (LSM), which is a fast and efficient qualitative approach able to retrieve the support of the scatterers starting from the scattered field data. After this step, the ACO is applied to retrieve the values of the relative dielectric permittivity and the electric conductivity. In this way, the ACO only needs to find a few parameters (two for every objects identified by the LSM). The approach has been extended to three-dimensional targets in [78, 79], where the full vector problem with arbitrary homogeneous dielectric targets is taken into account. Single and multiple dielectric objects are reconstructed with good accuracy and with low computational efforts. As an example, for a rectangular parallelepiped of dimensions $0.66\lambda \times 0.33\lambda \times 0.5\lambda$, after the support estimation, mean relative reconstruction errors equal to 2.5% (dielectric permittivity) and 7% (electric conductivity) are obtained with 45.6 cost function evaluations (mean value).

4.3. Artificial Bee Colony-Based Imaging Algorithms. The ABC has been applied for breast cancer detection in [80]. A full three-dimensional configuration is considered. The breast is modeled both by using simplified structures and a realistic MRI-based phantom. ABC is employed for the reconstruction of the position, size, and dielectric properties of the malignant inclusion (supposed of spherical size and homogeneous). The problem size is thus $G = 6$. A population of $P = 10$ bees is employed. In the reported test cases, ABC is able to reach the convergence in less than 30 iteration. Moreover, the algorithm is able to estimate the position and size of the tumor with satisfactory accuracy (e.g., in the simplified case, the localization error is less than 10% and the size estimation error is less than 1 mm). A comparison with PSO, DE, and GA is also provided. In the considered case, ABC outperforms the other approaches (GA provided the worst results PSO and DE gave similar results).

An example of use of the ABC for the reconstruction of the full distribution of the dielectric properties of unknown objects is reported in the following. Cylindrical scatterers under TM illumination are considered. A multiview configuration is assumed, that is, $S = 8$ line-current sources uniformly spaced on a circumference of radius 1.5λ are sequentially used for illuminating the objects. The scattered electric field is collected in 51 points uniformly spaced on an angular sector of 270 degrees on the same circumference (positioned such that the source lies in the sector without measurement probes). The investigation domain is a square area of side 2λ . The input data (scattered electric field) are computed by using a numerical code based on the method of moments [85] with pulse basis and Dirac’s delta

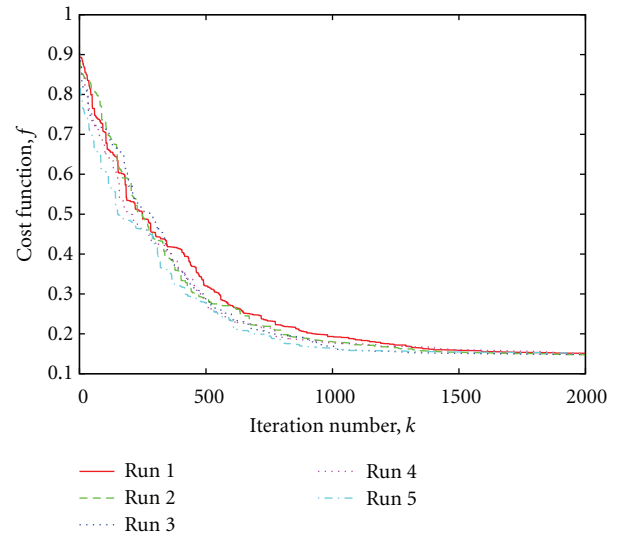


FIGURE 4: Cost function versus the iteration number. ABC-based inversion algorithm.

weighting functions. A finer mesh is used for solving the forward problem in order to avoid inverse crimes. Moreover, the computed electric field is corrupted with a Gaussian noise with zero mean value and variance corresponding to a signal-to-noise ratio of 25 dB. In the inversion procedure, the investigation area is discretized into $N = 256$ square subdomains, and the unknowns are the values of the relative dielectric permittivity in such cells. Two separate targets are located in the investigation area: a circular cylinder (radius 0.25λ , center $(-0.25\lambda, 0.25\lambda)$, relative dielectric permittivity 2.0) and a square cylinder (side 0.5λ , center $(0.25\lambda, -0.5\lambda)$, relative dielectric permittivity 1.5). The cost function (6), in its multiview version, is employed. The parameters of the ABC have been set equal to as follows: $C = 50$, $P = 25$, $K_{\text{lim}} = 100$, and $k_{\text{max}} = 2000$.

Some examples of the behavior of the cost function versus the iteration number are shown in Figure 4, which reports five different runs of the algorithms. As can be seen, in all cases, the method converges to a value of about 0.15. The corresponding mean relative reconstruction error is 3%. The same configuration has been considered in [76] and solved by using an ACO-based inversion approach. In the results provided in that paper, a mean relative error of about 4.5% is achieved with the ACO-based approach. Finally, an example of the reconstructed distribution of the dielectric properties obtained by the ABC approach is shown in Figure 5. As can be seen, the two objects are correctly shaped, and their permittivity is identified with quite good accuracy.

5. Conclusions

In this paper, the application of swarm intelligence algorithms, that is, stochastic algorithms inspired by the collective social behavior of agents (e.g., birds, ants, etc.), to the solution of microwave imaging problem has been reviewed.

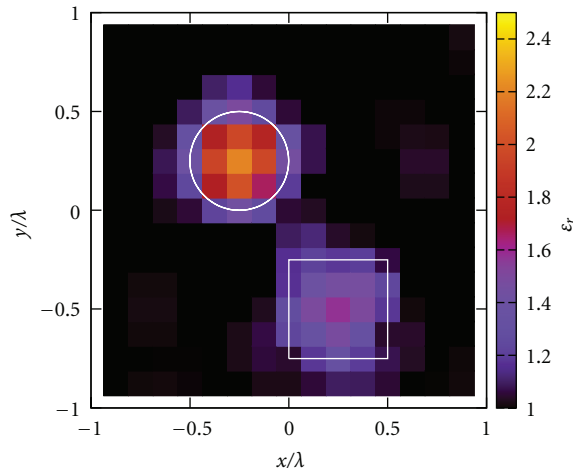


FIGURE 5: Example of reconstructed distribution of the dielectric permittivity. ABC-based inversion algorithm.

Such approaches have been proven to be very effective in several applications. The results available in the literature confirm the suitability of this class of optimization methods for microwave imaging, too.

References

- [1] M. Pastorino, *Microwave Imaging*, John Wiley, Hoboken, NJ, USA, 2010.
- [2] Y. J. Kim, L. Jofre, F. De Flaviis, and M. Q. Feng, "Microwave reflection tomographic array for damage detection of civil structures," *IEEE Transactions on Antennas and Propagation*, vol. 51, no. 11, pp. 3022–3032, 2003.
- [3] M. Benedetti, M. Donelli, G. Franceschini, M. Pastorino, and A. Massa, "Effective exploitation of the a priori information through a microwave imaging procedure based on the SMW for NDE/NDT applications," *IEEE Transactions on Geoscience and Remote Sensing*, vol. 43, no. 11, pp. 2584–2591, 2005.
- [4] L. Chommeloux, C. Pichot, and J. C. Bolomey, "Electromagnetic modeling for microwave imaging of cylindrical buried inhomogeneities," *IEEE Transactions on Microwave Theory and Techniques*, vol. 34, no. 10, pp. 1064–1076, 1986.
- [5] M. Pastorino, S. Caorsi, and A. Massa, "Numerical assessment concerning a focused microwave diagnostic method for medical applications," *IEEE Transactions on Microwave Theory and Techniques*, vol. 48, no. 1, pp. 1815–1830, 2000.
- [6] G. Bozza, C. Estatico, M. Pastorino, and A. Randazzo, "An inexact Newton method for microwave reconstruction of strong scatterers," *IEEE Antennas and Wireless Propagation Letters*, vol. 5, no. 1, pp. 61–64, 2006.
- [7] A. G. Tijhuis, K. Belkebir, A. C. S. Litman, and B. P. De Hon, "Theoretical and computational aspects of 2-D inverse profiling," *IEEE Transactions on Geoscience and Remote Sensing*, vol. 39, no. 6, pp. 1316–1330, 2001.
- [8] A. G. Tijhuis, K. Belkebir, A. C. S. Litman, and B. P. De Hon, "Multiple-frequency distorted-wave Born approach to 2D inverse profiling," *Inverse Problems*, vol. 17, no. 6, pp. 1635–1644, 2001.
- [9] G. Bozza, C. Estatico, A. Massa, M. Pastorino, and A. Randazzo, "Short-range image-based method for the inspection of strong scatterers using microwaves," *IEEE Transactions on Instrumentation and Measurement*, vol. 56, no. 4, pp. 1181–1188, 2007.
- [10] G. Bozza, C. Estatico, M. Pastorino, and A. Randazzo, "Application of an inexact-Newton method within the second-order Born approximation to buried objects," *IEEE Geoscience and Remote Sensing Letters*, vol. 4, no. 1, pp. 51–55, 2007.
- [11] C. Estatico, G. Bozza, A. Massa, M. Pastorino, and A. Randazzo, "A two-step iterative inexact-Newton method for electromagnetic imaging of dielectric structures from real data," *Inverse Problems*, vol. 21, no. 6, pp. S81–S94, 2005.
- [12] Z. Q. Zhang and Q. H. Liu, "Three-dimensional nonlinear image reconstruction for microwave biomedical imaging," *IEEE Transactions on Biomedical Engineering*, vol. 51, no. 3, pp. 544–548, 2004.
- [13] P. Mojabi and J. LoVetri, "Overview and classification of some regularization techniques for the Gauss-Newton inversion method applied to inverse scattering problems," *IEEE Transactions on Antennas and Propagation*, vol. 57, no. 9, pp. 2658–2665, 2009.
- [14] A. Litman, D. Lesselier, and F. Santosa, "Reconstruction of a two-dimensional binary obstacle by controlled evolution of a level-set," *Inverse Problems*, vol. 14, no. 3, pp. 685–706, 1998.
- [15] R. Autieri, G. Ferraiuolo, and V. Pascasio, "Bayesian regularization in nonlinear imaging: reconstructions from experimental data in nonlinearized microwave tomography," *IEEE Transactions on Geoscience and Remote Sensing*, vol. 49, no. 2, pp. 801–813, 2011.
- [16] C. Gilmore, P. Mojabi, and J. LoVetri, "Comparison of an enhanced distorted born iterative method and the multiplicative-regularized contrast source inversion method," *IEEE Transactions on Antennas and Propagation*, vol. 57, no. 8, pp. 2341–2351, 2009.
- [17] M. El-Shenawee, O. Dorn, and M. Moscoso, "An adjoint-field technique for shape reconstruction of 3-D penetrable object immersed in lossy medium," *IEEE Transactions on Antennas and Propagation*, vol. 57, no. 2, pp. 520–534, 2009.
- [18] P. Lobel, L. Blanc-Féraud, C. Pichet, and M. Barlaud, "A new regularization scheme for inverse scattering," *Inverse Problems*, vol. 13, no. 2, pp. 403–410, 1997.
- [19] T. M. Habashy and A. Abubakar, "A general framework for constraint minimization for the inversion of electromagnetic measurements," *Progress In Electromagnetics Research*, vol. 46, pp. 265–312, 2004.
- [20] P. M. Van Den Berg and A. Abubakar, "Contrast source inversion method: state of art," *Journal of Electromagnetic Waves and Applications*, vol. 15, no. 11, pp. 1503–1505, 2001.
- [21] A. Randazzo, G. Oliveri, A. Massa, and M. Pastorino, "Electromagnetic inversion with the multiscaling inexact Newton method-experimental validation," *Microwave and Optical Technology Letters*, vol. 53, no. 12, pp. 2834–2838, 2011.
- [22] S. Caorsi, A. Costa, and M. Pastorino, "Microwave imaging within the second-order born approximation: stochastic optimization by a genetic algorithm," *IEEE Transactions on Antennas and Propagation*, vol. 49, no. 1, pp. 22–31, 2001.
- [23] C.-C. Chiu and P. T. Liu, "Image reconstruction of a perfectly conducting cylinder by the genetic algorithm," *IEE Proceedings-Microwaves, Antennas and Propagation*, vol. 143, no. 3, p. 249, 1996.
- [24] A. Qing, C. K. Lee, and L. Jen, "Electromagnetic inverse scattering of two-dimensional perfectly conducting objects by real-coded genetic algorithm," *IEEE Transactions on Geoscience and Remote Sensing*, vol. 39, no. 3, pp. 665–676, 2001.
- [25] S. Caorsi, A. Massa, M. Pastorino, M. Raffetto, and A. Randazzo, "Detection of buried inhomogeneous elliptic cylinders

- by a memetic algorithm," *IEEE Transactions on Antennas and Propagation*, vol. 51, no. 10, pp. 2878–2884, 2003.
- [26] M. Pastorino, S. Caorsi, A. Massa, and A. Randazzo, "Reconstruction algorithms for electromagnetic imaging," *IEEE Transactions on Instrumentation and Measurement*, vol. 53, no. 3, pp. 692–699, 2004.
- [27] L. Garnero, A. Franchois, J. P. Hugonin, C. Pichot, and N. Joachimowicz, "Microwave imaging-complex permittivity reconstruction by simulated annealing," *IEEE Transactions on Microwave Theory and Techniques*, vol. 39, no. 11, pp. 1801–1807, 1991.
- [28] M. Pastorino, "Stochastic optimization methods applied to microwave imaging: a review," *IEEE Transactions on Antennas and Propagation*, vol. 55, no. 3, pp. 538–548, 2007.
- [29] Y. Rahmat-Samii and E. Michielssen, *Electromagnetic Optimization by Genetic Algorithms*, John Wiley & Sons, New York, NY, USA, 1999.
- [30] J. M. Johnson and Y. Rahmat-Samii, "Genetic algorithms in engineering electromagnetics," *IEEE Antennas and Propagation Magazine*, vol. 39, no. 4, pp. 7–21, 1997.
- [31] R. L. Haupt, "Introduction to genetic algorithms for electromagnetics," *IEEE Antennas and Propagation Magazine*, vol. 37, no. 2, pp. 7–15, 1995.
- [32] A. Massa, M. Pastorino, and A. Randazzo, "Reconstruction of two-dimensional buried objects by a differential evolution method," *Inverse Problems*, vol. 20, no. 6, pp. S135–S150, 2004.
- [33] D. S. Weile and E. Michielssen, "genetic algorithm optimization applied to electromagnetics: a review," *IEEE Transactions on Antennas and Propagation*, vol. 45, no. 3, pp. 343–353, 1997.
- [34] D. E. Goldberg, *Genetic Algorithms in Search, Optimization, and Machine Learning*, Addison-Wesley Professional, Reading, Mass, USA, 1st edition, 1989.
- [35] K. V. Price, "An introduction to differential evolution," in *New Ideas in Optimization*, pp. 79–108, McGraw-Hill, Maidenhead, UK, 1999.
- [36] E. Bonabeau, M. Dorigo, and G. Theraulaz, *Swarm Intelligence?: From Natural to Artificial Intelligence*, Oxford University Press, New York, NY, USA, 1999.
- [37] C. Blum and D. Merkle, *Swarm Intelligence Introduction and Applications*, Springer, London, UK, 2008.
- [38] J. F. Kennedy, R. C. Eberhart, and Y. Shi, *Swarm Intelligence*, Morgan Kaufmann Publishers, San Francisco, Calif, USA, 2001.
- [39] J. Robinson and Y. Rahmat-Samii, "Particle swarm optimization in electromagnetics," *IEEE Transactions on Antennas and Propagation*, vol. 52, no. 2, pp. 397–407, 2004.
- [40] M. Dorigo, V. Maniezzo, and A. Colorni, "Ant system: optimization by a colony of cooperating agents," *IEEE Transactions on Systems, Man, and Cybernetics B*, vol. 26, no. 1, pp. 29–41, 1996.
- [41] M. Dorigo and L. M. Gambardella, "Ant colony system: a cooperative learning approach to the traveling salesman problem," *IEEE Transactions on Evolutionary Computation*, vol. 1, no. 1, pp. 53–66, 1997.
- [42] C. Estatico, M. Pastorino, and A. Randazzo, "A novel microwave imaging approach based on regularization in L_p Banach spaces," *IEEE Transactions on Antennas and Propagation*, vol. 60, no. 7, pp. 3373–3381, 2012.
- [43] G. Bilchev and I. C. Parmee, "The ant colony metaphor for searching continuous design spaces," in *Proceedings of the Selected Papers from AISB Workshop on Evolutionary Computing*, pp. 25–39, Sheffield, UK, 1995.
- [44] J. Dréo and P. Siarry, "A new ant colony algorithm using the heterarchical concept aimed at optimization of multimimima continuous functions," in *Proceedings of the 3rd International Workshop on Ant Algorithms (ANTS '02)*, pp. 216–221, London, UK, 2002.
- [45] N. Monmarché, G. Venturini, and M. Slimane, "On how *Pachycondyla apicalis* ants suggest a new search algorithm," *Future Generation Computer Systems*, vol. 16, no. 8, pp. 937–946, 2000.
- [46] K. Socha and M. Dorigo, "Ant colony optimization for continuous domains," *European Journal of Operational Research*, vol. 185, no. 3, pp. 1155–1173, 2008.
- [47] D. Karaboga, "An idea based on honey bee swarm for numerical optimization," Tech. Rep. TR06, Erciyes University, Kayseri, Turkey, 2005.
- [48] D. Karaboga and B. Basturk, "Artificial Bee Colony (ABC) optimization algorithm for solving constrained optimization problems," in *Foundations of Fuzzy Logic and Soft Computing*, P. Melin, O. Castillo, L. T. Aguilar, J. Kacprzyk, and W. Pedrycz, Eds., vol. 4529, pp. 789–798, Springer, Berlin, Germany.
- [49] V. Tereshko and A. Loengarov, "Collective decision making in honey-bee foraging dynamics," *Computing and Information Systems*, vol. 9, no. 3, pp. 1–7, 2005.
- [50] A. Semnani, M. Kamyab, and I. T. Rekanos, "Reconstruction of one-dimensional dielectric scatterers using differential evolution and particle swarm optimization," *IEEE Geoscience and Remote Sensing Letters*, vol. 6, no. 4, pp. 671–675, 2009.
- [51] A. Semnani and M. Kamyab, "Comparison of differential evolution and particle swarm optimization in one-dimensional reconstruction problems," in *Proceedings of the Asia Pacific Microwave Conference (APMC '08)*, pp. 1–4, Hong Kong, December 2008.
- [52] A. M. Emad Eldin, E. A. Hashish, and M. I. Hassan, "Inversion of lossy dielectric profiles using particle swarm optimization," *Progress In Electromagnetics Research M*, vol. 9, pp. 93–105, 2009.
- [53] A. Fhager, A. Voronov, C. Chen, and M. Persson, "Methods for dielectric reconstruction in microwave tomography," in *Proceedings of the 2nd European Conference on Antennas and Propagation (EuCAP '07)*, pp. 1–6, Edinburgh, UK, November 2007.
- [54] C.-H. Huang, C. C. Chiu, C. L. Li, and K. C. Chen, "Time domain inverse scattering of a two-dimensional homogenous dielectric object with arbitrary shape by particle swarm optimization," *Progress in Electromagnetics Research*, vol. 82, pp. 381–400, 2008.
- [55] S. Caorsi, M. Donelli, A. Lommi, and A. Massa, "Location and imaging of two-dimensional scatterers by using a particle swarm algorithm," *Journal of Electromagnetic Waves and Applications*, vol. 18, no. 4, pp. 481–494, 2004.
- [56] H. Zhang, X. D. Zhang, J. Ji, and Y. J. Yao, "Electromagnetic imaging of the 2-D media based on Particle Swarm algorithm," in *Proceedings of the 6th International Conference on Natural Computation (ICNC '10)*, pp. 262–265, Yantai, China, August 2010.
- [57] S. H. Zainud-Deen, W. M. Hassen, and K. H. Awadalla, "Techniques, crack detection using a hybrid finite difference frequency domain and particle swarm optimization," in *Proceedings of the National Radio Science Conference (NRSC '09)*, pp. 1–8, Cairo, Egypt, March 2009.
- [58] S. H. Zainud-Deen, W. M. Hassen, E. M. Ali, K. H. Awadalla, and H. A. Sharshar, "Breast cancer detection using a hybrid finite difference frequency domain and particle swarm optimization techniques," in *Proceedings of the 25th National Radio Science Conference (NRSC '08)*, pp. 1–8, Tanta, Egypt, March 2008.

- [59] I. T. Rekanos and M. Kanaki, "Microwave imaging of two-dimensional conducting scatterers using particle swarm optimization," in *Electromagnetic Fields in Mechatronics, Electrical and Electronic Engineering*, A. Krawczyk, S. Wiak, and L. M. Fernandez, Eds., pp. 84–89, IOS Press, Amsterdam, The Netherlands, 2006.
- [60] I. T. Rekanos, "Shape reconstruction of a perfectly conducting scatterer using differential evolution and particle swarm optimization," *IEEE Transactions on Geoscience and Remote Sensing*, vol. 46, no. 7, pp. 1967–1974, 2008.
- [61] T. Huang and A. S. Mohan, "Application of particle swarm optimization for microwave imaging of lossy dielectric objects," in *Proceedings of the IEEE Antennas and Propagation Society International Symposium and USNC/URSI Meeting*, vol. 1B, pp. 852–855, Washington, DC, USA, July 2005.
- [62] T. Huang and A. Sanagavarapu Mohan, "A microparticle swarm optimizer for the reconstruction of microwave images," *IEEE Transactions on Antennas and Propagation*, vol. 55, no. 3, pp. 568–576, 2007.
- [63] C.-L. Li, C. C. Chiu, and C. H. Huang, "Time domain inverse scattering for a homogenous dielectric cylinder by asynchronous particle swarm optimization," *Journal of Testing and Evaluation*, vol. 39, no. 3, 2011.
- [64] C. Wei, C. H. Sun, J. O. Wu, C. C. Chiub, and M. K. Wu, "Inverse scattering for the perfectly conducting cylinder by asynchronous particle swarm optimization," in *Proceedings of the 3rd IEEE International Conference on Communication Software and Networks*, pp. 410–4412, Xi'an, China, 2011.
- [65] C.-H. Sun, C. C. Chiu, and C. L. Li, "Time-domain inverse scattering of a two-dimensional metallic cylinder in slab medium using asynchronous particle swarm optimization," *Progress In Electromagnetics Research M*, vol. 14, pp. 85–100, 2010.
- [66] B. Mhamdi, K. Grayaa, and T. Aguilu, "Microwave imaging for conducting scatterers by hybrid particle swarm optimization with simulated annealing," in *Proceedings of the 8th International Multi-Conference on Systems, Signals and Devices (SSD '11)*, pp. 1–6, Sousse, Tunisia, March 2011.
- [67] G. R. Huang, W. J. Zhong, and H. W. Liu, "Microwave imaging based on the AWE and HPSO incorporated with the information obtained from born approximation," in *Proceedings of the International Conference on Computational Intelligence and Software Engineering (CiSE '10)*, pp. 1–4, Wuhan, Chin, December 2010.
- [68] B. Mhamdi, K. Grayaa, and T. Aguilu, "An inverse scattering approach using hybrid PSO-RBF network for microwave imaging purposes," in *Proceedings of the 16th IEEE International Conference on Electronics, Circuits and Systems (ICECS '09)*, pp. 231–234, Hammamet, Tunisia, December 2009.
- [69] M. Donelli, G. Franceschini, A. Martini, and A. Massa, "An integrated multiscaling strategy based on a particle swarm algorithm for inverse scattering problems," *IEEE Transactions on Geoscience and Remote Sensing*, vol. 44, no. 2, pp. 298–312, 2006.
- [70] M. Donelli and A. Massa, "Computational approach based on a particle swarm optimizer for microwave imaging of two-dimensional dielectric scatterers," *IEEE Transactions on Microwave Theory and Techniques*, vol. 53, no. 5, pp. 1761–1776, 2005.
- [71] D. Franceschini and A. Massa, "An integrated stochastic multi-scaling strategy for microwave imaging applications," in *Proceedings of the IEEE Antennas and Propagation Society International Symposium and USNC/URSI Meeting*, pp. 209–212, Washington, DC, USA, July 2005.
- [72] G. Franceschini, M. Donelli, R. Azaro, and A. Massa, "Inversion of phaseless total field data using a two-step strategy based on the iterative multiscaling approach," *IEEE Transactions on Geoscience and Remote Sensing*, vol. 44, no. 12, pp. 3527–3539, 2006.
- [73] R. Azaro, D. Franceschini, G. Franceschini, L. Manica, and A. Massa, "A two-step strategy for a multi-scaling inversion of phaseless measurements of the total field," in *Proceedings of the IEEE Antennas and Propagation Society International Symposium, APS 2006*, pp. 1073–1076, Albuquerque, NM, USA, July 2006.
- [74] M. Donelli, D. Franceschini, P. Rocca, and A. Massa, "Three-dimensional microwave imaging problems solved through an efficient multiscaling particle swarm optimization," *IEEE Transactions on Geoscience and Remote Sensing*, vol. 47, no. 5, pp. 1467–1481, 2009.
- [75] D. Franceschini, G. Franceschini, M. Donelli, P. Rocca, and A. Massa, "Imaging three-dimensional bodies by processing multi-frequency data through a multiscale swarm intelligence based method," in *Proceedings of the IEEE Antennas and Propagation Society International Symposium (AP-S '07)*, pp. 409–412, Honolulu, Hawaii, USA, June 2007.
- [76] M. Pastorino and A. Randazzo, "Nondestructive analysis of dielectric bodies by means of an Ant Colony Optimization method," in *Swarm Intelligence for Electric and Electronic Engineering*, G. Fornarelli and L. Mescia, Eds., IGI Global, Hershey, Pa, USA, 2012.
- [77] M. Brignone, G. Bozza, A. Randazzo, R. Aramini, M. Piana, and M. Pastorino, "Hybrid approach to the inverse scattering problem by using ant colony optimization and no-sampling linear sampling," in *Proceedings of the IEEE International Symposium on Antennas and Propagation and USNC/URSI National Radio Science Meeting (APSURSI '08)*, pp. 1–4, San Diego, Calif, USA, July 2008.
- [78] G. Bozza, M. Brignone, M. Pastorino, M. Piana, and A. Randazzo, "An inverse scattering based hybrid method for the measurement of the complex dielectric permittivities of arbitrarily shaped homogenous targets," in *Proceedings of the IEEE Instrumentation and Measurement Technology Conference (I2MTC '09)*, pp. 719–723, Singapore, May 2009.
- [79] M. Brignone, G. Bozza, A. Randazzo, M. Piana, and M. Pastorino, "A hybrid approach to 3D microwave imaging by using linear sampling and ACO," *IEEE Transactions on Antennas and Propagation*, vol. 56, no. 10, pp. 3224–3232, 2008.
- [80] M. Donelli, I. Craddock, D. Gibbins, and M. Sarafianou, "A three-dimensional time domain microwave imaging method for breast cancer detection based on an evolutionary algorithm," *Progress In Electromagnetics Research M*, vol. 18, pp. 179–195, 2011.
- [81] K. Belkebir and M. Saillard, "Special section: testing inversion algorithms against experimental data," *Inverse Problems*, vol. 17, no. 6, p. 1565, 2001.
- [82] K. Tenglong, Z. Xiaoying, W. Jian, and D. Yihan, "A modified ACO algorithm for the optimization of antenna layout," in *Proceedings of the 2011 International Conference on Electrical and Control Engineering*, pp. 4269–4272, Yichang, China, 2011.
- [83] G. Weis, A. Lewis, M. Randall, and D. Thiel, "Pheromone pre-seeding for the construction of RFID antenna structures using ACO," in *Proceedings of the 6th IEEE International Conference on e-Science, eScience 2010*, pp. 161–167, Brisbane, Australia, December 2010.

- [84] I. Vilovic, N. Burum, Z. Sipus, and R. Nad, "PSO and ACO algorithms applied to location optimization of the WLAN base station," in *Proceedings of the 19th International Conference on Applied Electromagnetics and Communications (ICECom '07)*, pp. 1–5, Dubrovnik, Croatia, September 2007.
- [85] R. Harrington, *Field Computation by Moment Methods*, IEEE Press, Piscataway, NJ, USA, 1993.

Research Article

Wide Range Temperature Sensors Based on One-Dimensional Photonic Crystal with a Single Defect

Arun Kumar,¹ Vipin Kumar,² B. Suthar,³ A. Bhargava,⁴ Kh. S. Singh,² and S. P. Ojha⁵

¹AITTM, Amity University, NOIDA 201303, India

²Department of Physics, Digamber Jain (P.G.) College, Baraut 250611, India

³Department of Physics, Govt. College of Engineering & Technology, Bikaner 334004, India

⁴Nanophysics Laboratory, Department of Physics, Govt. Dungar College, Bikaner 334001, India

⁵Director General, IIMT Group of Colleges, Noida 201303, India

Correspondence should be addressed to Vipin Kumar, vrpcommon@gmail.com

Received 21 March 2012; Revised 9 June 2012; Accepted 27 June 2012

Academic Editor: Yeou Song (Brian) Lee

Copyright © 2012 Arun Kumar et al. This is an open access article distributed under the Creative Commons Attribution License, which permits unrestricted use, distribution, and reproduction in any medium, provided the original work is properly cited.

Transmission characteristics of one-dimensional photonic crystal structure with a defect have been studied. Transfer matrix method has been employed to find the transmission spectra of the proposed structure. We consider a Si/air multilayer system and refractive index of Si layer has been taken as temperature dependent. As the refractive index of Si layer is a function of temperature of medium, so the central wavelength of the defect mode is a function of temperature. Variation in temperature causes the shifting of defect modes. It is found that the average change or shift in central wavelength of defect modes is 0.064 nm/K. This property can be exploited in the design of a temperature sensor.

1. Introduction

Since the last two and half decades, investigations on various properties of photonic crystals, particularly photonic bandgap materials, have become an area of interest for many researchers [1–6]. It was observed that periodic modulation of the dielectric functions significantly modifies the spectral properties of the electromagnetic waves. The transmission and reflection spectra of such structures are characterized by the presence of allowed and forbidden photonic bands similar to the electronic band structure of periodic potentials. For this reason, such a new class of artificial optical material with periodic dielectric modulation is known as photonic bandgap (PBG) material [3]. Fundamental optical properties like band structure, reflectance, group velocity and the rate of spontaneous emission, and so forth can be controlled effectively by changing the spatial distribution of the dielectric function [4, 5]. This fact has opened up important possibilities for the design of novel optical and optoelectronic devices. Conventional photonic crystals have periodic modulation of homogeneous refractive

indices, and they are artificially fabricated with periods that are comparable to the wavelength of the electromagnetic waves. These photonic crystals lead to formation of photonic bandgaps or stop bands, in which propagation of electromagnetic waves of certain wavelengths is prohibited. A one-dimensional photonic crystal (1D PC) structure has many interesting applications such as dielectric reflecting mirrors, optical switches, filters, and optical limiters. It has also been demonstrated theoretically and experimentally that 1D PCs can have absolute omnidirectional PBGs [7–11].

In addition to the existence of wide bandgaps in some properly designed PCs, the feature of a tunable PBG is an interesting property of such PCs. The PBG can be tuned by means of some external agents [12]. For instance, it can be changed by the operating temperature and we call it T-tuning. A superconductor/dielectric PC belongs to this class of PC. This happens because of the temperature-dependent London perturbation length in the superconducting materials [13–15]. Using a liquid crystal as one of the constituents in a PC, the T-tuning optical response is also obtainable [16]. Recently, PCs containing semiconductor as

one of the constituents have also been investigated by many researchers. PCs with intrinsic semiconductor belong to T-tuning devices because the dielectric constant of an intrinsic semiconductor is strongly dependent on temperature [17].

Although these applications can be realized using pure PCs, but doped or defective PCs may be more useful, just as semiconductor doped by impurities is more important than the pure ones for various applications. The idea of doped PCs comes from the consideration of the analogy between electromagnetism and solid state physics, which lead to the study of band structures of periodic materials and further to the possibility of the occurrence of localized modes in the bandgap when a defect is introduced in the lattice. These defect-enhanced structures are called doped photonic crystals and present some resonant transmittance peaks in the bandgap corresponding to the occurrence of the localized states [18], due to the change of the interference behavior of the incident waves. Defect(s) can be introduced into perfect PCs by changing the thickness of the layer [19], inserting another dielectric into the structure [20], or removing a layer from it [21, 22].

The introduction of the defect states within PCs has been perceived as a new dimension in the study of photonic crystals, especially in 2D and 3D PCs, due to numerous possible applications that can be achieved by using them. In 2D or 3D PCs, it has been known that a point defect can act as a micro cavity, a line defect like a waveguide, and a planar defect like a perfect mirror [6]. Similar to 2D or 3D PCs, the introduction of the defect layers in 1D PCs can also create localized defect modes within the PBGs. Due to the simplicity in 1D PC fabrications over 2D and 3D PCs, the defect mode can be easily introduced within 1D PCs. Such PCs with defect(s) can be exploited for the design of various applications such as in the design of TE/TM filters and splitters [23], in the fabrication of lasers [24], and in light emitting diodes [25]. The existence of defect mode in 1D PCs depends upon a number of parameters such as refractive indices of the layers, filling fraction, the thickness of defect layer, and the angle of incidence. If all other parameters are kept constant and the refractive index of the material is changed, then any change in refractive index of a material results to a change or shift the position of the defect mode in the reflection/transmission spectra. In this present communication, a wide range temperature sensor based on one-dimensional photonic crystal with a single defect has been proposed.

Here, we consider the Si/air multilayer system with a defect in the form of a single Si layer in the middle. Si is taken as one of the constituents of a one-dimensional photonic crystal. Since the refractive index of Si depends on temperature [17], so any change in the temperature of the constituent material will change the refractive index of the material, and hence the wavelength corresponding to the middle of the defect mode will also change or shift. By measuring this change or shift in the position of defect mode, the change in the temperature can be measured, so it can work as a temperature sensor. In this present work, we will restrict our study for normal incidence only.

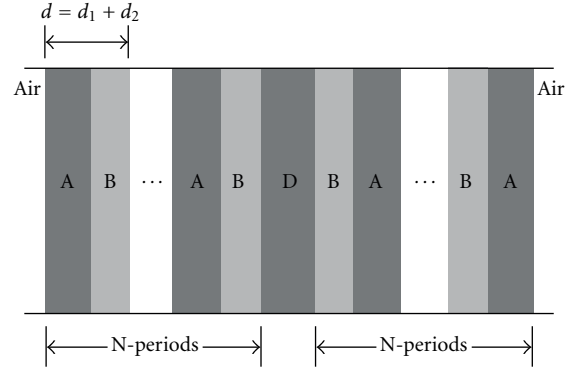


FIGURE 1: Schematic diagram of 1-D photonic crystal with defect.

2. Theoretical Analysis

The schematic representation of one-dimensional photonic crystal with defect is represented in Figure 1.

We consider $\text{air}/(AB)^N D (BA)^N / \text{air}$, in which A and B represent the layers of high and low refractive index materials, and D is the defect layer. To compute the defect mode in the transmission spectrum, we employ the transfer matrix method (TMM) [26, 27]. In this method, the transfer matrix for each layer can be written as

$$M_j = Z_j P_j Z_j^{-1}, \quad (1)$$

where j stands for A, B, or D layers and Z_j and P_j are called the dynamical matrix, and the propagation matrix, respectively. The dynamical matrix is given by the following equations:

$$Z_j = \begin{pmatrix} 1 & 1 \\ n_j \cos \theta_j & -n_j \cos \theta_j \end{pmatrix}, \text{ for TE mode of polarization,}$$

$$Z_j = \begin{pmatrix} \cos \theta_j & \cos \theta_j \\ n_j & -n_j \end{pmatrix}, \text{ for TM mode of polarization,}$$
(2)

where θ_j is the ray angle in the layers and n_j is the refractive index of the layers. Also, the propagation matrix P_j can be defined as

$$P_j = \begin{pmatrix} e^{i\delta_j} & 0 \\ 0 & e^{-i\delta_j} \end{pmatrix}, \quad (3)$$

where the phase is written as

$$\delta_j = \frac{2\pi d_j}{\lambda} n_j \cos \theta_j. \quad (4)$$

The transfer matrix, for the structure (Figure 1), embedded in air, $\text{air}/(AB)^N D (BA)^N / \text{air}$ can be written as

$$M = \begin{pmatrix} M_{11} & M_{12} \\ M_{21} & M_{22} \end{pmatrix} = Z_0^{-1} (M_A M_B)^N M_D (M_A M_B)^N Z_0, \quad (5)$$

where Z_0 is called the dynamical matrix for air.

The transmittance (T) and reflectance (R) can be calculated by using the matrix elements M_{11} and M_{21} given in (5) as follows:

$$T = \left| \frac{1}{M_{11}} \right|^2, \quad R = \left| \frac{M_{21}}{M_{11}} \right|^2. \quad (6)$$

In the next section, structural parameters of the device have been defined.

3. Proposed Structure and Structural Parameters

We choose Si for the materials A and D, air for material B, and $N = 5$ in Figure 1. Silicon and air have been taken as the high and the low refractive index materials, respectively, and an additional silicon layer (D) as the defect layer. The geometrical parameters are so chosen that the thicknesses of high and low refractive index materials are $d_1 = 600$ nm, $d_2 = 1200$ nm and the thickness of defect layer is taken 1800 nm. The thermal expansion coefficient for silicon layer is $2.6 \times 10^{-6}/\text{K}$, which is negligible small quantity. So we neglect the thermal expansion of Si layer in our computation.

The refractive index of air is independent of temperature and wavelength. But the refractive index of silicon layer is taken as a function of both wavelength and temperature. The refractive index of Silicon (Si) in the ranges 1.2 to 14 μm and 20–1600 K is represented as [17]

$$n^2(\lambda, T) = \varepsilon(T) + \frac{e^{-3\Delta L(T)/L_{293}}}{\lambda^2} \times (0.8948 + 4.3977 \times 10^{-4}T + 7.3835 \times 10^{-8}T^2), \quad (7)$$

where

$$\varepsilon(T) = 11.4445 + 2.7739 \times 10^{-4}T + 1.7050 \times 10^{-6}T^2 - 8.1347 \times 10^{-10}T^3,$$

$$\frac{\Delta L(T)}{L_{293}} = -0.071 + 1.887 \times 10^{-6}T + 1.934 \times 10^{-9}T^2 - 4.554 \times 10^{-13}T^3 \quad \text{for } 293 \text{ K} \leq T \leq 1600 \text{ K},$$

$$\frac{\Delta L(T)}{L_{293}} = -0.021 - 4.149 \times 10^{-7}T - 4.620 \times 10^{-10}T^2 + 1.482 \times 10^{-11}T^3 \quad \text{for } 20 \text{ K} \leq T \leq 293 \text{ K}. \quad (8)$$

The plot of the refractive index as the function of wavelength and temperature is shown in Figure 2. From Figure 2, it is clear that the refractive index of silicon layer increases with the increase in temperature. Therefore, the refractive index contrast increases with temperature.

In the next section, we will compute the transmission spectra of photonic crystal with defect by using (6) as shown in Figure 1.

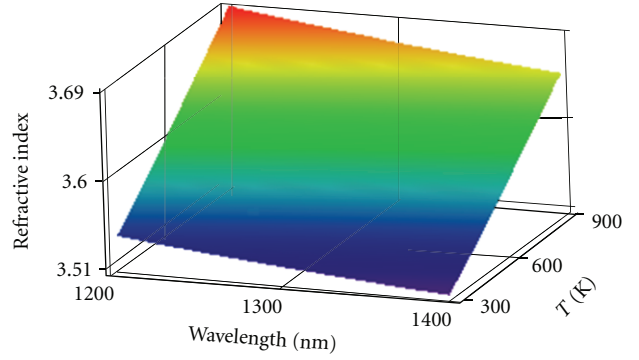


FIGURE 2: Variation of refractive index of Si as a function of wavelength and temperature.

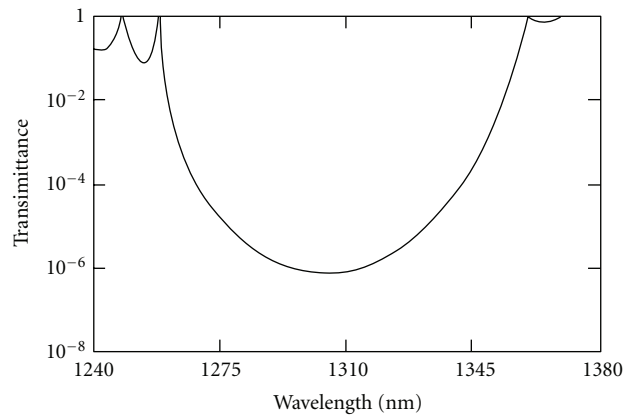


FIGURE 3: Transmittance for an ideal PC of $(\text{Si}/\text{air})^{10}$ at 100 K temperature.

4. Result and Discussion

In this section, we present the working principle of the proposed temperature sensor. The transmission spectra of the ideal PC $(\text{Si}/\text{air})^{10}$ at 100 K temperature for normal incidence are shown in Figure 3. If a defect which is in the form of silicon layer is introduced in this PC, then a defect mode appears inside the bandgap. The transmission spectra of the PC with a defect $[(\text{Si}/\text{air})^5\text{Si}(\text{air}/\text{Si})^5]$ at 100 K temperature are shown in Figure 4. As shown in this figure a defect mode has a mid-wavelength centered at 1288.3 nm. Thus, from this figure it is clear that if the incident radiation of wavelengths ranging from 1275 nm to 1350 nm is incident normally on the proposed structure at 100 K, then it will pass only 1288.3 nm wavelength and all other wavelengths will be reflected. More interestingly, this defect mode can be shifted to the longer wavelength region by the variation of temperature. The transmission spectra of the proposed structure at various temperature are shown in Figure 5, and the corresponding data is tabulated in Table 1. From Figure 5 and Table 1, it is clear that the transmission peak centered at 1288.3 nm at 100 K has been shifted to 1300.08 nm, 1312.9 nm, and 1326.8 nm corresponding to temperatures at 300 K, 500 K, and 700 K, respectively. Further, it is also clear that as the temperature of the structure increases,

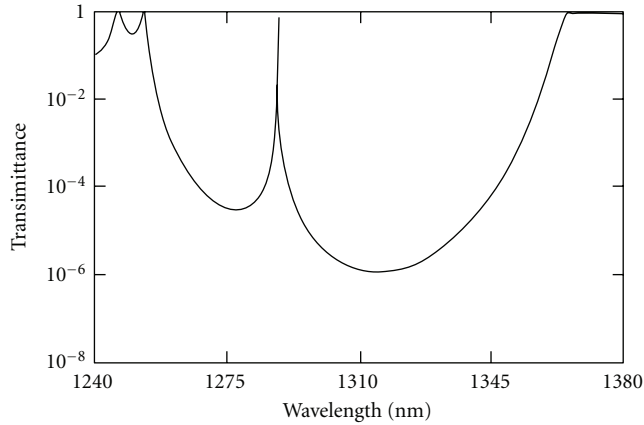


FIGURE 4: The defect mode for a PC with defect of $[(\text{Si}/\text{air})^5\text{Si}(\text{air}/\text{Si})^5]$ at 100 K temperature.

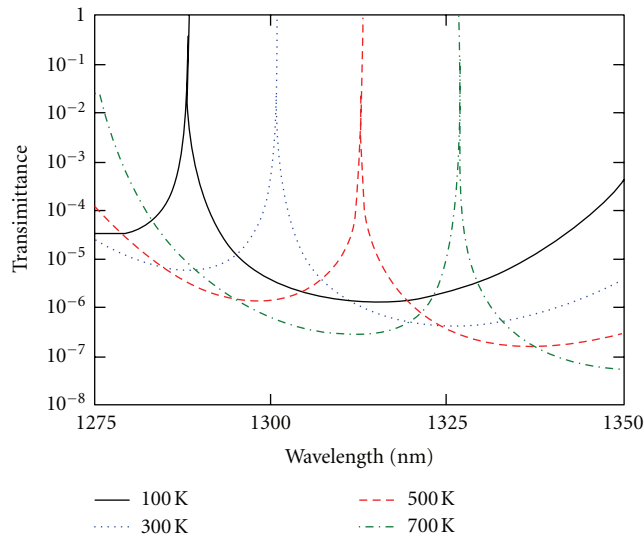


FIGURE 5: Transmission spectra of proposed structure at different temperature.

the defect mode of transmission shifts towards the higher wavelength region. The dependence of defect modes on temperature is due to the dependence of refractive index on temperature as given in (7). The shifting behavior can be explained by using the phase relation given by (4). According to this equation, as refractive index $n(\lambda, T)$ increases with temperature, the wavelength must increase accordingly to keep the phase δ unchanged. The variation of central wavelength of defect modes with temperature is shown in Figure 6. It is found that the central wavelength of defect modes changes approximately linearly with temperature. The average change in central wavelength of defect mode is 0.064 nm/K. This change in central wavelength is almost 9 times more than the previous reported work [28]. So the proposed structure is more sensitive to temperature variation. Earlier studies on defect filters reported response time of the order of \sim ms to \sim ps range with different techniques [29, 30]. Gan et al. achieved a response rise time

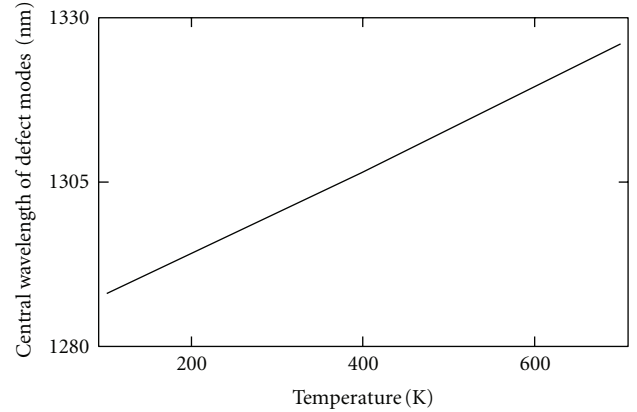


FIGURE 6: The variation of central wavelength of defect modes with temperature.

TABLE 1: Central wavelength of defect modes.

Temperature (K)	Central wavelength of defect mode (nm)
100	1288.3
300	1300.8
500	1312.9
700	1326.8

of $7 \mu\text{s}$ and a fall time of $14 \mu\text{s}$ for silicon photonic structures [31]. For the proposed temperature sensor, the response time for silicon will decide slow or fast response. Thus, by measuring the change or shift in the central wavelength of the defect mode, we can measure the temperature in a wide range. Hence, the proposed structure may be used as a temperature sensor in a wide range.

5. Conclusion

In the present communication, a simple design of temperature sensor has been proposed. The proposed structure is based on the one-dimensional photonic structure with defect. It is found that introduction of defect in the conventional one-dimensional photonic crystal creates a defect mode. Silicon has been chosen as one of the constituents of the device, because refractive index of the Si depends on the temperature. It is found that centre of this defect mode depends on the temperature of the device and it change linearly with temperature. An average change or shift in the central wavelength of defect mode is 0.064 nm/K. So, we can use the proposed device as a temperature sensor. The proposed device may also have many applications in different optical systems.

References

- [1] S. John, "Strong localization of photons in certain disordered dielectric superlattices," *Physical Review Letters*, vol. 58, no. 23, pp. 2486–2489, 1987.
- [2] E. Yablonovitch, "Inhibited spontaneous emission in solid-state physics and electronics," *Physical Review Letters*, vol. 58, no. 20, pp. 2059–2062, 1987.

- [3] C. Soukoulis, *Photonic Band Gap Materials*, Kluwer Academic, Dordrecht, The Netherlands, 1996.
- [4] J. A. M. Rojas, J. Alpuente, J. Piñeiro, and R. Sánchez, "Rigorous full vectorial analysis of electromagnetic wave propagation in ID inhomogeneous media," *Progress in Electromagnetics Research*, vol. 63, pp. 89–105, 2006.
- [5] E. Yablonovitch and T. J. Gmitter, "Photonic band structure: the face-centered-cubic case," *Physical Review Letters*, vol. 63, no. 18, pp. 1950–1953, 1989.
- [6] H. Y. Lee and T. Yao, "Design and evaluation of omnidirectional one-dimensional photonic crystals," *Journal of Applied Physics*, vol. 93, no. 2, pp. 819–830, 2003.
- [7] J. P. Dowling, "Mirror on the wall: you're omnidirectional after all!" *Science*, vol. 282, no. 5395, pp. 1841–1842, 1998.
- [8] E. Yablonovitch, "Engineered omnidirectional external-reflectivity spectra from one-dimensional layered interference filters," *Optics Letters*, vol. 23, no. 21, pp. 1648–1649, 1998.
- [9] D. N. Chigrin, A. V. Lavrinenko, D. A. Yarotsky, and S. V. Gaponenko, "Observation of total omnidirectional reflection from a one-dimensional dielectric lattice," *Applied Physics A*, vol. 68, no. 1, pp. 25–28, 1999.
- [10] B. Suthar, V. Kumar, Kh. S. Singh, and A. Bhargava, "Tuning of photonic band gaps in one dimensional chalcogenide based photonic crystal," *Optics Communications*, vol. 285, no. 6, pp. 1505–1509, 2012.
- [11] V. Kumar, Kh. S. Singh, S. K. Singh, and S. P. Ojha, "Broadening of omnidirectional photonic band gap in Si-based one dimensional photonic crystals," *Progress in Electromagnetics Research M*, vol. 14, pp. 101–111, 2010.
- [12] B. Suthar, V. Kumar, A. Kumar, Kh. S. Singh, and A. Bhargava, "Thermal expansion of photonic band gap for one dimensional photonic crystal," *Progress in Electromagnetics Research Letters*, vol. 32, pp. 81–90, 2012.
- [13] O. L. Berman, Y. E. Lozovik, S. L. Eiderman, and R. D. Coalson, "Superconducting photonic crystals: numerical calculations of the band structure," *Physical Review B*, vol. 74, no. 9, Article ID 092505, 2006.
- [14] H. Takeda and K. Yoshino, "Tunable photonic band schemes in two-dimensional photonic crystals composed of copper oxide high-temperature superconductors," *Physical Review B*, vol. 67, no. 24, Article ID 245109, 6 pages, 2003.
- [15] W. H. Lin, C. J. Wu, T. J. Yang, and S. J. Chang, "Terahertz multichanneled filter in a superconducting photonic crystal," *Optics Express*, vol. 18, no. 26, pp. 27155–27166, 2010.
- [16] P. Halevi, J. A. Reyes-Avendaño, and J. A. Reyes-Cervantes, "Electrically tuned phase transition and band structure in a liquid-crystal-infilled photonic crystal," *Physical Review E*, vol. 73, no. 4, Article ID 040701(R), 4 pages, 2006.
- [17] H. H. Li, "Refractive index of silicon and germanium and its wavelength and temperature derivatives," *The Journal of Physical Chemistry*, vol. 9, no. 3, pp. 561–658, 1980.
- [18] G. Guida, A. de Lustrac, and P. Priou, "An introduction to Photonic Band Gap (PBG) materials," *Progress in Electromagnetics Research Letters*, vol. 41, pp. 1–20, 2003.
- [19] B. Suthar and A. Bhargava, "Temperature-dependent tunable photonic channel filter," *IEEE Photonics Technology Letters*, vol. 24, no. 5, Article ID 6096365, pp. 338–340, 2012.
- [20] C. M. Soukoulis, "Photonic band gaps and localization," in *Proceedings of the NATO Advanced Research Workshop*, Plenum Press, London, UK, May 1993.
- [21] D. R. Smith, R. Dalichaouch, N. Kroll, S. Schultz, S. L. McCall, and P. M. Platzman, "Photonic band structure and defects in one and two dimensions," *Journal of the Optical Society of America B*, vol. 10, no. 2, pp. 314–321, 1993.
- [22] V. Kumar, Kh. S. Singh, and S. P. Ojha, "Abnormal behaviour of one-dimensional photonic crystal with defect," *Optik*, vol. 122, no. 13, pp. 1183–1187, 2011.
- [23] Z. M. Jiang, B. Shi, D. T. Zhao, J. Liu, and X. Wang, "Silicon-based photonic crystal heterostructure," *Applied Physics Letters*, vol. 79, no. 21, pp. 3395–3397, 2001.
- [24] W. D. Zhou, J. Sabarinathan, P. Bhattacharya et al., "Characteristics of a photonic bandgap single defect microcavity electroluminescent device," *IEEE Journal of Quantum Electronics*, vol. 37, no. 9, pp. 1153–1160, 2001.
- [25] M. W. Feise, I. V. Shadrivov, and Y. S. Kivshar, "Bistable diode action in left-handed periodic structures," *Physical Review E*, vol. 71, no. 3, Article ID 037602, 4 pages, 2005.
- [26] P. Yeh, *Optical Waves in Layered Media*, John Wiley and Sons, New York, NY, USA, 1988.
- [27] M. Born and E. Wolf, *Principle of Optics*, Pergamon, Oxford, UK, 4th edition, 1970.
- [28] W. C. L. Hopman, P. Pottier, D. Yulistira et al., "Quasi-one-dimensional photonic crystal as a compact building-block for refractometric optical sensors," *IEEE Journal on Selected Topics in Quantum Electronics*, vol. 11, no. 1, pp. 11–16, 2005.
- [29] S. Toyoda, N. Ooba, A. Kaneko, M. Hikita, T. Kurihara, and T. Maruno, "Wideband polymer thermo-optic wavelength tunable filter with fast response for WDM systems," *Electronics Letters*, vol. 36, no. 7, pp. 658–660, 2000.
- [30] X. Hu, Q. Gong, Y. Liu, B. Cheng, and D. Zhang, "Ultrafast tunable filter in two-dimensional organic photonic crystal," *Optics Letters*, vol. 31, no. 3, pp. 371–373, 2006.
- [31] F. Gan, T. Barwicz, M. A. Popović et al., "Maximizing the thermo-optic tuning range of silicon photonic structures," in *Proceeding of the IEEE International Conference on Photonics in Switching*, August 2007.

Research Article

Complex Permittivity Measurements of Textiles and Leather in a Free Space: An Angular-Invariant Approach

B. Kapilevich, B. Litvak, M. Anisimov, D. Hardon, and Y. Pinhasi

Department Electrical and Electronics Engineering, Ariel University Center of Samaria, Ariel 40700, Israel

Correspondence should be addressed to B. Kapilevich, boriskap@ariel.ac.il

Received 5 March 2012; Accepted 15 May 2012

Academic Editor: Andrea Randazzo

Copyright © 2012 B. Kapilevich et al. This is an open access article distributed under the Creative Commons Attribution License, which permits unrestricted use, distribution, and reproduction in any medium, provided the original work is properly cited.

The paper describes the complex permittivity measurements of textiles and leathers in a free space at 330 GHz. The destructive role of the Rayleigh scattering effect is considered and the angular-invariant limit for an incidence angle has been found out experimentally within 25–30 degrees. If incidence angle exceeds this critical parameter, the uncertainty caused by the Rayleigh scattering is drastically increased preventing accurate measurements of the real and imaginary parts of a bulky material. The phenomenon must be taken into consideration in predicting shielding effectiveness of materials covering hidden object in concealed threat detection with millimeter-wave radar systems.

1. Introduction

Submillimeter and THz waves demonstrate a reasonable penetration depth in certain common materials, such as fabric, plastic, and wood. Therefore, they are good candidates for detecting various hidden objects such as concealed weapons, drugs, and explosives. In the last decade, there has been a growing demand in mm, sub-mm, and THz imaging systems for homeland security applications [1, 2]. In particular, efficiency of these systems depends on shielding effectiveness of materials screening the detected object [3].

Complex permittivity $\epsilon(f)$ is widely used for characterization of dielectric materials. It is frequency-dependent quantity, resulting in attenuation and phase shifts of electromagnetic wave propagating in media. In a slab structure, the permittivity can be acquired from the transmission and reflection coefficients. Knowledge of the dielectric properties of these materials is important in predicting overall performance of mm-wave imagers because a penetration depth is governed by these characteristics. There are a lot of microwave methods suggested for measuring complex permittivity [4], but free-space approach is more suitable in sub-mm range since the sample size has reasonable dimensions in order to avoid undesirable edge diffraction effect. However, the drawback of most free-space measuring systems is the ripples (or parasitic resonances) in the measured data caused

by multiple reflections from sample surfaces and antennas that cannot be accurately predicted in the theoretical models. As a result, various smoothing algorithms based on heuristic criteria must be used to overcome degrading measurement accuracy [5, 6].

An isotropic slab in air [7] is the basic theoretical model employed for retrieving the complex permittivity from the measured data. However, approximation of textiles having typical woven fabric nature and leather materials with nonregular surface's shaping by uniform dielectric slab is incorrect. Indeed, texture and surface roughness maybe comparable with wavelength and responsible for the Rayleigh scattering that may drastically degrade the measurement accuracy. One to overcome the problem is the development of special data smoothing algorithms [8] needed to avoid undesirable rapid oscillations caused by the parasitic standing wave interference between R_x and T_x antennas as well as other factors. As a result, the originally measured transmittance cannot be used for validation of the best-fitting permittivity without additional specific processing.

Assuming that textiles and leathers are isotropic materials, they must have invariant values of complex permittivity regardless of an incidence angle. The deviations of real and imaginary parts of the dielectric constant can be considered as a measure of a nonuniformity of the thickness and

surface's shape of the dielectric slab approximating a real sample. This parameter has statistical nature and should be characterized by standard deviation of the measured material characteristics in angular domain. In the present study, the matched THz power meter (MPM) has been used in the transmittance measurements at 330 GHz resulting in a minimization of destructive role of the parasitic standing wave interference [9]. High directivity Gaussian beam horn-lens antenna was employed in order to suppress undesirable spillover effect during variations of the sample's position.

2. Theoretical Basis of the Model

Assume that dielectric slab of thickness d is illuminated by plane wave with incident angle θ_0 . The field reflection r and transmission t coefficients being basic physical parameters measured in free-space method can be presented in general form via proper Fresnel's formulas [10] as nonlinear functions of d , θ_0 , the frequency f , and the relative complex dielectric constant $\epsilon'_r - j\epsilon''_r$:

$$t = \frac{(1 - \rho_0^2) e^{-jk_z(f)d}}{1 - \rho_0^2 e^{-j2k_z(f)d}} = \frac{(1 - \rho_0^2) e^{-(\alpha+j\beta) \cos(\theta)d}}{1 - \rho_0^2 e^{-2(\alpha+j\beta) \cos(\theta)d}}, \quad (1)$$

$$r = \rho_0 \cdot \frac{1 - e^{-j2k_z(f)d}}{1 - \rho_0^2 e^{-j2k_z(f)d}} = \rho_0 \cdot \frac{1 - e^{-2(\alpha+j\beta) \cos(\theta)d}}{1 - \rho_0^2 e^{-2(\alpha+j\beta) \cos(\theta)d}},$$

where

$$\rho_0 = \begin{cases} \frac{\sqrt{\epsilon_0} \cos(\theta_0) - \sqrt{\epsilon_r} \cos(\theta)}{\sqrt{\epsilon_0} \cos(\theta_0) + \sqrt{\epsilon_r} \cos(\theta)} & \text{TE wave} \\ \frac{\sqrt{\epsilon_0} \cos(\theta) - \sqrt{\epsilon_r} \cos(\theta_0)}{\sqrt{\epsilon_0} \cos(\theta) + \sqrt{\epsilon_r} \cos(\theta_0)} & \text{TM wave.} \end{cases} \quad (2)$$

According to the generalized Snell's law, we can write the following for lossy dielectric medium:

$$tg(\theta) = \frac{\sin(\theta_0)}{\text{Re} \left\{ \sqrt{\frac{(\epsilon'_r - j\epsilon''_r) - \sin^2(\theta_0)}{\epsilon_r}} \right\}}. \quad (3)$$

If the experimental setup is equipped by a vector network analyzer (VNA), the magnitude and phase of r and t can be measured. Otherwise the power transmission and reflection coefficients are available only

$$|t|^2 = \frac{(1 - \rho_0^2)^2 e^{-2\alpha \cos(\theta)d}}{[1 - \rho_0^2 e^{-2\alpha \cos(\theta)d}]^2 + 4\rho_0^2 e^{-2\alpha \cos(\theta)d} \sin^2[\beta \cos(\theta)d]},$$

$$|r|^2 = \rho_0^2 \frac{[1 - e^{-2\alpha \cos(\theta)d}]^2 + 4e^{-2\alpha \cos(\theta)d} \sin^2[\beta \cos(\theta)d]}{[1 - \rho_0^2 e^{-2\alpha \cos(\theta)d}]^2 + 4\rho_0^2 e^{-2\alpha \cos(\theta)d} \sin^2[\beta \cos(\theta)d]}. \quad (4)$$

The real and imaginary parts of the dielectric constant as a function of incidence angle were evaluated from the

measured transmittance using the numerical root-finding algorithm applied to the system of nonlinear equations:

$$\begin{aligned} |t(f, d, \theta_1, \epsilon'_r, \epsilon''_r)|^2 &= T_{p1}, \\ |t(f, d, \theta_2, \epsilon'_r, \epsilon''_r)|^2 &= T_{p2}, \end{aligned} \quad (5)$$

where T_{p1} and T_{p2} are power transmission coefficients measured at the incidence angles θ_1 and θ_2 , respectively, d is the thickness of a dielectric slab. Then, the proper standard deviations were determined for textile and leather samples in order to characterize angular invariances of the measured parameters. This model is used below for extracting complex permittivity from the measured data.

3. The Experimental Setup

In order to avoid an undesirable cross-polarization effect, all the measurements are suggested to perform with a parallel polarization, for which MPM is well matched as it is operating near the Brewster angle of the absorbing RF power thin-film sensor as shown in Figure 1. For absorbing thin film element of the power meter (Thomas Keating THz Power Meter, <http://www.terahertz.co.uk/>) this angle is equal to 55.5 degrees. The input window of the power meter must be aligned at the Brewster angle in order to reach the best matching condition.

Figure 2 shows the photo of the experimental setup assembled for the material characterization near $f = 330$ GHz. The THz source consists of the X-Band Synthesizer with power amplifier at its output that drives multistage multiplier (4 sections) with the total multiplication factor $32 = 4 \times 2 \times 2 \times 2$. Output signal about 10 mW is radiated by the horn-lens antenna (1.3 deg beam width and 42 dB gain). Other details concerning the source can be found in [1]. Energy propagating through the dielectric slab is captured by absorbing thin film of THz power meter and after processing is displayed on the PC monitor. The tested material is fixed by special frame maintained on programmable rotary joint model URS-75-BPP (Newport).

The measurement procedure includes the two steps:

- (i) calibration-measurement of the transmitted signal without material under test (P_0);
- (ii) measurements of the transmitted signal as a function of incident angle in a presence of material under test (P_1);

the ratio P_1/P_0 is the power transmittance needed to extract the complex permittivity.

4. Results of Transmittance Measurements and Reconstruction Complex Permittivity

Several types of the textiles have been tested. The specifications of these materials are summarized in the Table 1. Also,

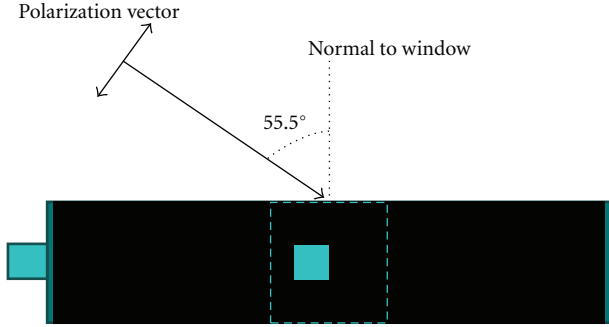


FIGURE 1: The position the MPM's head aligned at the Brewster angle 55.5 degrees to the incoming beam in order to minimize reflections from the input window.

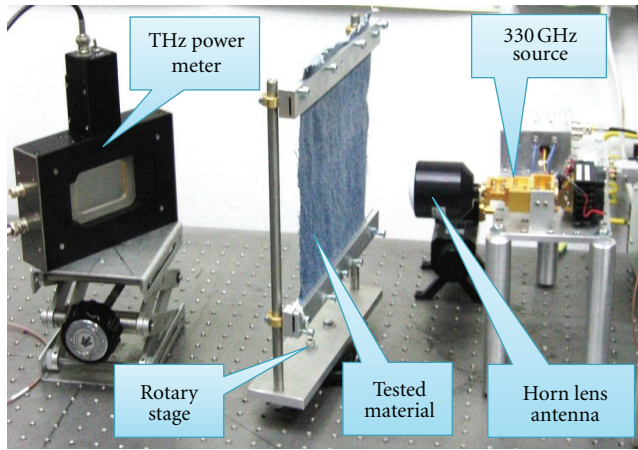


FIGURE 2: Photo of the experimental setup.

several types of leathers have been tested, see Table 2. Figures 3 and 4 show the measured transmittances as a function of incidence angle for textile and leather samples, respectively. The polarization is matched with polarization of the power meter.

The reconstructing procedure needed to restore complex permittivity from the transmittance measurements has been described in [9]. The solution of the system of nonlinear equations (5) requires knowledge of the two independent transmittances for corresponding incidence angles. The latter can be arbitrary but we have fixed one of them assuming that $\theta_1 = 0$ while the second angle was varied in range $5 \leq \theta_2 \leq 50$ degrees. Tables 3 and 4 summarize the restored real and imaginary parts of dielectric constants of the textile's samples for different incidence angles. The similar data are given in the Tables 5 and 6 for leather's samples.

Both textile and leather samples have demonstrated variations of complex permittivity for different incidence angles due to nonuniform thickness, surface roughness, specific texture and non-ideal flatness. All these factors have statistical nature and can be characterized by standard deviation presented in the last lines of the Tables 3–6.

5. Angular-Invariant Limits of the Incidence Angle

In order to estimate the angular-invariant limits of the incident angle we assume that surface the roughness of textile's and leather's samples satisfies to the Rayleigh scattering condition [11]:

$$\Delta h < \frac{\lambda}{8 \cos \theta_i}, \quad (6)$$

where Δh is roughness variation, θ_i is incidence angle, and λ is free space wavelength. Figure 5 illustrates schematically forward scattered rays "generated" by roughness surface.

Since the roughness variation Δh and incidence angle θ_i are interrelated due to expression (6), we can expect that the uncertainty in a determination of the complex permittivity should be increased with increasing θ_i , too. The question is what is the acceptable range of incidence angles θ_i invariant to the bulky complex permittivity of the material under test-textile and leather in our case? To answer the question we need to compare the measured transmittance of a real material having rough surface with the calculated transmittance of the smoothed dielectric slab made from the same bulky material. The results of such comparison are shown in Figure 6 (textile's sample number 3, $\epsilon'_r = 2.72$ and $\epsilon''_r = 0.068$) and Figure 7 (leather's sample number 0, $\epsilon'_r = 3.4$ and $\epsilon''_r = 0.127$), where the lines marked by symbol $\square\square\square$ correspond to the measured transmittance while the solid lines depict the calculated data. The averaged values of the real and imaginary parts of the dielectric constants given in the Tables 3–6 were substituted to the theoretical model described by (4). The comparison theory and experiments reveals an existence of the critical incidence angle, θ_c . The latter is determined by the angular-invariance limit of the forward Rayleigh scattering as well as operating wavelength. The materials discussed have the critical angles about 25 degrees for leather's sample and 30 degrees for textile's one. If an incidence angle is greater than the critical one ($\theta_i > \theta_c$), the measurement of the bulk permittivity will be quite problematic due to violating the angular-invariant limit. On the other hand, there is a critical roughness variation Δh , too. Using (6), this parameter was found to be equal to about 0.15 mm for operating frequency 330 GHz and $\theta_c = 30^\circ$. These estimates seem to be realistic for the typical kinds of textiles and leathers.

It would be important to derive an existence of the angular-invariant limit from a theoretical model. Such a model must unify both deterministic and statistic properties of real structure of materials under test. Microwave properties of the common weave architectures used in woven fabric structural composites have been investigated in [12] using deterministic approach. Other perspective way is an application of the concept of the fractional Brownian motion appropriately describing natural surfaces [13] assuming that surface profiles can be approximated by the Weierstrass-Mandelbrot (WM) fractal functions. However, some entry parameters needed for real-world calculations such as the

TABLE 1: The summary of textile's samples under test.

Material	Sample no. 1 (denim)	Sample no. 2	Sample no. 3	Sample no. 4	Sample no. 5	Sample no. 6 (wool scarf)	Sample no. 7 (stockinet)	Sample no. 8 (satin)
General view of samples under testing								
Thickness d , mm	0.8	0.45	0.25	0.7	0.25	1.6	0.65	0.2
Power transmittance at normal incidence	77%	87%	92%	86%	88.8%	35%	67%	91%

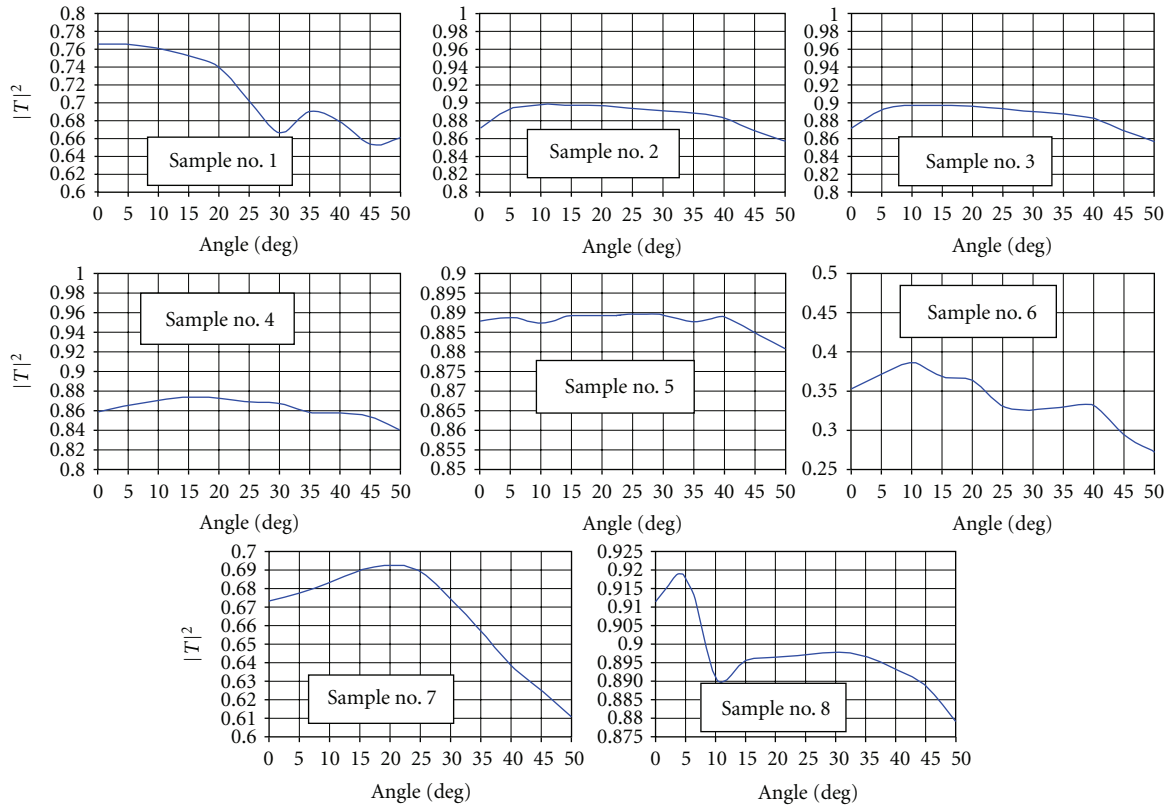


FIGURE 3: Measured power transmittance of the textile's samples as a function of incidence angle.

TABLE 2: The summary of leather's samples under test.

Material	Sample no. 0 (natural leather)	Sample no. 1 (artificial leather)	Sample no. 2 (artificial leather)	Sample no. 3 (artificial leather)	Sample no. 4 (artificial leather)	Sample no. 5 (artificial leather)
General view of samples under testing						
Thickness d , mm	1.15	0.95	1	0.6	0.8	0.6
Power transmittance at normal incidence	48%	63%	68%	81.5%	71%	77%

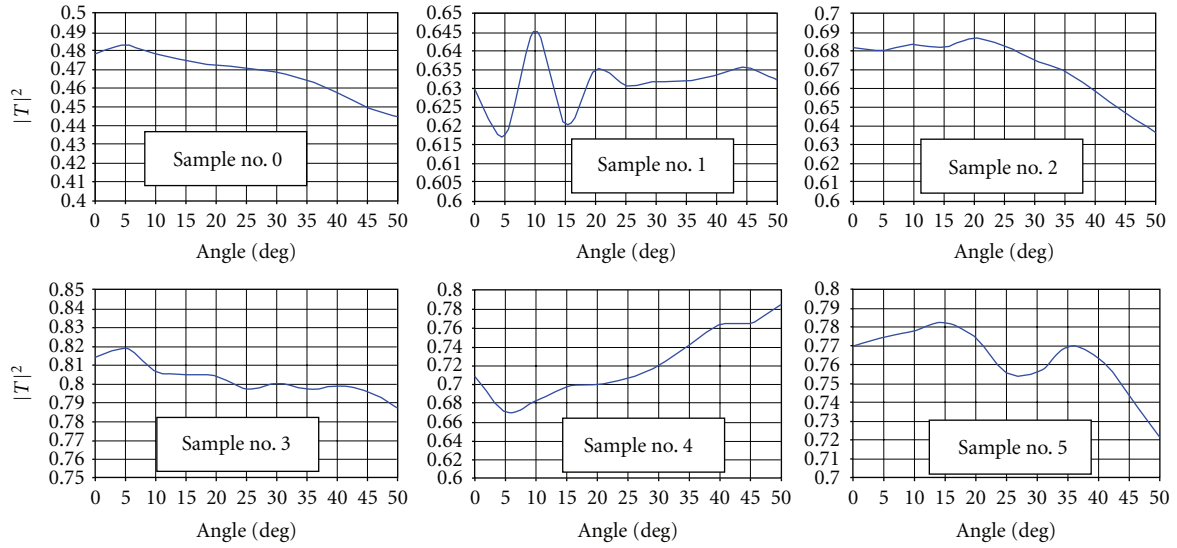


FIGURE 4: Measured power transmittance of the leather’s samples as a function of incidence angle.

TABLE 3: Real part of the permittivity evaluated for the textile’s samples: $\theta_1 = 0$ and different incidence angles θ_2 .

Incidence angle, θ_2 degrees	Sample no. 1 (Denim)	Sample no. 2	Sample no. 3	Sample no. 4	Sample no. 5	Sample no. 6 (wool scarf)	Sample no. 7 (stock-inet)	Sample no. 8 (satin)
5	2.83	2.77	2.73	3.65	2.54	3.2	3.15	2.73
10	2.71	2.71	2.7	3.76	2.43	3.21	3.13	2.69
15	2.67	2.92	2.74	3.67	2.41	3.23	3.17	2.73
20	2.7	2.76	2.77	3.67	2.49	3.12	3.17	2.75
25	2.73	2.68	2.79	3.65	2.51	3.11	3.2	2.76
30	2.69	2.5	2.75	3.67	2.54	3.14	3.34	2.75
35	2.67	2.26	2.7	3.66	2.54	3.17	3.34	2.76
40	2.75	2.84	2.75	3.68	2.58	3.2	3.22	2.76
45	2.78	2.95	2.59	3.66	2.68	3.22	3.26	2.75
50	2.79	3.01	2.71	3.58	2.68	3.23	3.21	2.76
Averaged, ϵ'_r	2.73	2.74	2.72	3.66	2.54	3.18	3.22	2.74
Standard deviation	0.054	0.253	0.0623	0.0458	0.0956	0.0452	0.0737	0.0216

TABLE 4: Imaginary part of the permittivity evaluated for the textile’s samples: $\theta_1 = 0$ and different incidence angles θ_2 .

Incidence angle, θ_2 degrees	Sample no. 1 (cotton jeans)	Sample no. 2	Sample no. 3	Sample no. 4	Sample no. 5	Sample no. 6 (wool scarf)	Sample no. 7 (stock-inet)	Sample no. 8 (satin)
5	0.0715	0.033	0.07	0.041	0.065	0.133	0.054	0.074
10	0.0633	0.029	0.057	0.028	0.06	0.13	0.057	0.072
15	0.0603	0.0103	0.06	0.038	0.045	0.134	0.041	0.071
20	0.0634	0.033	0.062	0.043	0.048	0.145	0.042	0.072
25	0.071	0.0397	0.065	0.044	0.052	0.158	0.054	0.072
30	0.0781	0.011	0.068	0.044	0.061	0.159	0.076	0.073
35	0.074	0.011	0.071	0.044	0.072	0.159	0.1	0.074
40	0.079	0.019	0.08	0.043	0.077	0.161	0.119	0.077
45	0.0858	0.06	0.085	0.044	0.089	0.172	0.126	0.08
50	0.0866	0.065	0.069	0.047	0.092	0.175	0.13	0.086
Averaged, ϵ''_r	0.073	0.031	0.068	0.042	0.066	0.15	0.08	0.075
Standard deviation	0.0092	0.0222	0.0097	0.0056	0.0172	0.0162	0.0356	0.0049

TABLE 5: Real part of the permittivity evaluated for the leather's samples: $\theta_1 = 0$ and different incidence angles θ_2 .

Incidence angle, θ_2 degrees	Sample no. 0	Sample no. 1	Sample no. 2	Sample no. 3	Sample no. 4	Sample no. 5
5	2.91	3.3	2.95	2.18	2.7	2.48
10	3.31	2.97	3.03	2.03	2.71	2.75
15	3.39	3.17	3.03	2.05	2.73	2.66
20	3.42	2.99	3.08	2.16	2.96	2.51
25	3.45	3.02	3.04	2.11	3.03	2.33
30	3.44	3.03	3.05	2.26	3.09	2.45
35	3.46	3.06	3.05	2.28	3.19	2.45
40	3.5	3.12	3.03	2.28	3.23	2.43
45	3.58	3.17	2.9	2.26	3.25	2.43
50	3.54	3.21	2.92	2.13	3.28	2.45
Averaged, ϵ'_r	3.4	3.104	3.008	2.17	3.02	2.49
Standard deviation	0.178	0.102	0.058	0.094	0.220	0.1221

TABLE 6: Imaginary part of the permittivity for the leather's samples: $\theta_1 = 0$ and different incidence angles θ_2 .

Incidence angle, θ_2 degrees	Sample no. 0	Sample no. 1	Sample no. 2	Sample no. 3	Sample no. 4	Sample no. 5
5	0.118	0.093	0.078	0.066	0.088	0.084
10	0.109	0.072	0.08	0.062	0.086	0.065
15	0.115	0.079	0.081	0.063	0.083	0.075
20	0.118	0.061	0.08	0.066	0.096	0.09
25	0.12	0.067	0.079	0.065	0.096	0.088
30	0.125	0.071	0.079	0.069	0.091	0.088
35	0.131	0.077	0.078	0.069	0.084	0.087
40	0.14	0.083	0.079	0.067	0.076	0.088
45	0.148	0.089	0.079	0.0676	0.0751	0.088
50	0.15	0.098	0.083	0.067	0.069	0.095
Averaged, ϵ''_r	0.127	0.079	0.08	0.066	0.084	0.085
Standard deviation	0.0135	0.0111	0.0014	0.0023	0.0086	0.0084

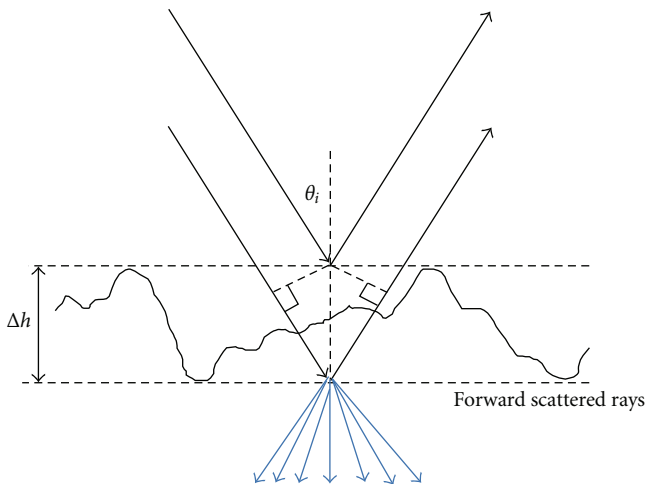
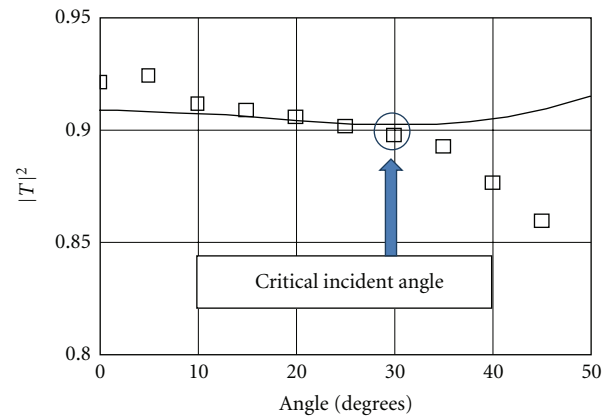


FIGURE 5: Illustration of the forward Rayleigh scattering effect in presence of a roughness surface.

vertical height profile scaling factor, random variables which account for the amplitude, and the phase behavior of each tone, and others [14] must be specified for materials

FIGURE 6: Comparison calculated (solid line) and measured (symbol $\square\square\square$) transmittances as a function of an incidence angle (the textile's sample #3, $\epsilon'_r = 2.72$ and $\epsilon''_r = 0.068$).

under test which is not trivial problem. Anyway, we hope that the above experiments will be an additional stimulus for developing proper models combining deterministic and statistic approaches, too.

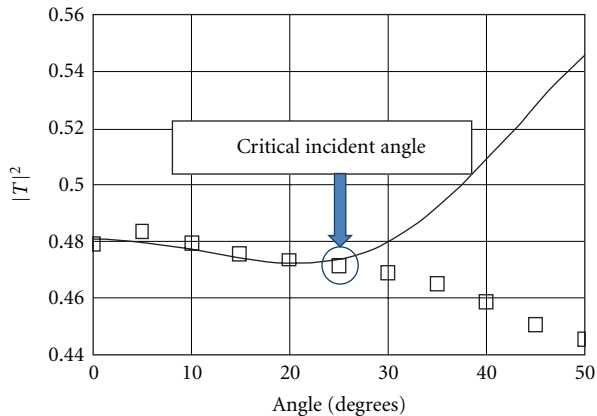


FIGURE 7: Comparison calculated (solid line) and measured (symbol \square) transmittances as a function of an incidence angle (the leather's sample no. 0, $\epsilon'_r = 3.4$ and $\epsilon''_r = 0.127$).

6. Conclusions

The complex permittivities of textiles and leathers were measured at 330 GHz using the absolute THz power meter with thin-film sensor operating near the Brewster angle in order to provide a minimum multiple-reflection effect. The incidence-angular invariance has been estimated experimentally and existence of a critical incidence angle was found out. It is not recommended to carry out free-space permittivity measurements if the incidence angle exceeds the critical one (25–30 degrees in our case) since the forward Rayleigh scattering effect may drastically degrade the measurement accuracy.

Acknowledgments

Authors would like to thank Dr. J Polivka for fruitful discussions and A. Shulzinger and S. Neporent for assistance in the design and assembling the measuring setup used in the experiments discussed.

References

- [1] B. Kapilevich, Y. Pinhasi, R. Arusi et al., "330 GHz FMCW image sensor for homeland security applications," *Journal of Infrared, Millimeter, and Terahertz Waves*, vol. 31, no. 11, pp. 1370–1381, 2010.
- [2] B. Kapilevich and M. Einat, "Detecting hidden objects on human body using active millimeter wave sensor," *IEEE Sensors Journal*, vol. 10, no. 11, Article ID 5482043, pp. 1746–1752, 2010.
- [3] S. Van den Bulcke, A. Franchois, and D. De Zutter, "2.5 D quantitative millimeter wave imaging of a hidden object on a simplified human body model using value picking regularization," *Journal of Infrared, Millimeter, and Terahertz Waves*, vol. 31, no. 12, pp. 1478–1490, 2010.
- [4] L. F. Chen, C. K. Ong, C. P. Neo, V. V. Varadan, and V. K. Varadan, *Microwave Electronics: Measurement and Material Characterization*, John Wiley & Sons, New York, NY, USA, 2004.

- [5] N. Gagnon, J. Shaker, L. Roy, A. Petosa, and P. Berini, "Low-cost free-space measurement of dielectric constant at Ka band," *IEE Proceedings: Microwaves, Antennas and Propagation*, vol. 151, no. 3, pp. 271–276, 2004.
- [6] K. M. Hock, "Error correction for diffraction and multiple scattering in free-space microwave measurement of materials," *IEEE Transactions on Microwave Theory and Techniques*, vol. 54, no. 2, pp. 648–659, 2006.
- [7] W. D. Burnside and K. W. Burgener, "High frequency scattering by a thin lossless dielectric slab," *IEEE Transactions on Antennas and Propagation*, vol. AP-31, no. 1, pp. 104–110, 1983.
- [8] S. W. Harmer, N. Rezgui, N. Bowering, Z. Luklinska, and G. Ren, "Determination of the complex permittivity of textiles and leather in the 14–40 GHz millimetre-wave band using a free-wave transmittance only method IET Microw," *IEEE Transactions on Antennas and Propagation*, vol. 2, no. 6, pp. 606–614, 2008.
- [9] B. Kapilevich, Y. Pinhasi, and B. Litvak, "Measurement of complex permittivity of lossy materials in free space using matched THz power meter?" *The International Journal on Infrared Millimeter THz Waves*, vol. 32, no. 12, pp. 1446–1456, 2011.
- [10] S. V. Marshall and G. G. Skitek, *Electromagnetic Concepts and Applications*, Prentice-Hall, New York, NY, USA, 2nd edition, 1987.
- [11] S. R. Saunders and A. Aragon-Zavala, *Antennas and Propagation for Wireless Communication Systems*, John Wiley, New York, NY, USA, 2007.
- [12] M. S. Mirotznik, S. Yarlagadda, R. McCauley, and P. Pa, "Broadband electromagnetic modeling of woven fabric composites," *IEEE Transactions on Microwave Theory and Techniques*, vol. 60, no. 1, pp. 158–169, 2012.
- [13] B. B. Mandelbrot, *The Fractal Geometry of Nature*, W. H. Freeman, New York, NY, USA, 1983.
- [14] G. Franceschetti, A. Iodice, D. Riccio, and G. Ruello, "Fractal surfaces and electromagnetic extended boundary conditions," *IEEE Transactions on Geoscience and Remote Sensing*, vol. 40, no. 5, pp. 1018–1031, 2002.

Research Article

Buried Object Detection by an Inexact Newton Method Applied to Nonlinear Inverse Scattering

Matteo Pastorino and Andrea Randazzo

Department of Naval, Electrical, Electronic, and Telecommunication Engineering, University of Genoa, Via Opera Pia 11A, 16145 Genova, Italy

Correspondence should be addressed to Matteo Pastorino, matteo.pastorino@unige.it

Received 20 March 2012; Revised 11 June 2012; Accepted 12 June 2012

Academic Editor: Kristen M. Donnell

Copyright © 2012 M. Pastorino and A. Randazzo. This is an open access article distributed under the Creative Commons Attribution License, which permits unrestricted use, distribution, and reproduction in any medium, provided the original work is properly cited.

An approach to reconstruct buried objects is proposed. It is based on the integral equations of the electromagnetic inverse scattering problem, written in terms of the Green's function for half-space geometries. The full nonlinearity of the problem is exploited in order to inspect strong scatterers. After discretization of the continuous model, the resulting equations are solved in a regularization sense by means of a two-step inexact Newton algorithm. The capabilities and limitations of the method are evaluated by means of some numerical simulations.

1. Introduction

Subsurface imaging is an important subject in several applicative areas, including seismic and geophysical prospecting, nondestructive, testing and medical diagnostics [1–39]. Electromagnetic techniques are widely applied to face this problem. Ground penetrating radar [40] is the basic instrumentation able to retrieve discontinuities in the lower subspace (the ground). Processing of GPR data can allow an improvement in the detection and localization capabilities of the system. In some cases, neural network-based approaches have been adopted [41]. Moreover, inverse-scattering-based techniques have been proposed, too. By using these methods, the measured values of the field scattered by the discontinuities present in the lower half space are “inverted” in order to obtain the spatial distributions of dielectric parameters (e.g., the dielectric permittivity and the electric conductivity) inside a fixed inspection domain. Approaches of this kind have been proposed, for example, for the detection of water leaking from pipes [42]. If an accurate model of the buried scatterers is available, it would be possible to retrieve information about the buried objects in terms of their dielectric parameters.

The present authors developed in [43] an inverse-scattering-based method for buried object imaging under the second-order Born approximation (SOBA) [21, 44–48]. By using the SOBA, the reconstruction of buried objects has been obtained with a better accuracy with respect to linearized approximations. In particular, due to the nonlinear nature of the scattering equations, in which the electric field inside the inspected region is an unknown quantity as well as the spatial distributions of the dielectric properties of the medium, the SOBA allows to approximately retrieve the field distribution, too.

However, in order to detect strong discontinuities, the exact nonlinear inverse scattering formulation must be considered. This approach has been faced in [49, 50], in which strong scatterers have been reconstructed in free space under tomographic imaging conditions. The approach proposed in [49], which is based on the use an inexact Newton method, has been experimentally tested in [51]. The same method has been successfully applied in [52] within the contrast source formulation (under free-space conditions).

In the present paper, the approach developed in [43] for buried object detection under the SOBA is extended to treat strong scatterers. In this case, the exact nonlinear inverse

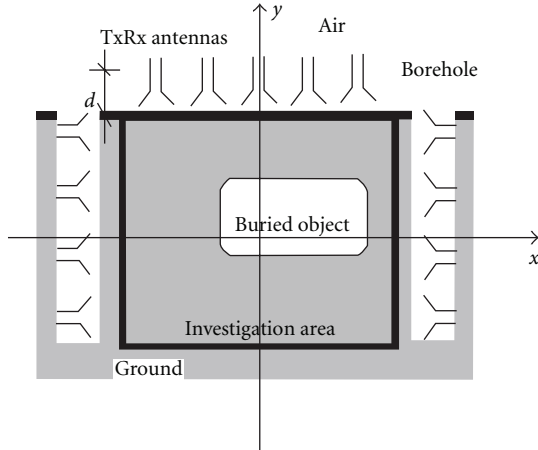


FIGURE 1: Geometrical configuration of the problem.

scattering formulation, in terms of the half-space Green's function, is taken into account. In particular, starting from the integral equations for the scattered field for cylindrical objects, slides of the spatial distributions of the dielectric parameters are reconstructed by numerically solving these equations in a regularization sense.

The paper is organized as follows. In Section 2 the mathematical formulation of the approach is reported. In Section 3, the application of the inexact Newton method is described. Numerical results are reported in Section 4, and conclusions are drawn in Section 5.

2. Mathematical Formulation

Let us consider a cylindrical object buried in a homogeneous-half-space medium (Figure 1). A 2D transverse-magnetic (TM) configuration is assumed. The dielectric properties of the buried object are assumed to be independent of the z coordinate. The transmitting and receiving antennas are located in the transverse plane and generate a z -polarized electric field in both the half spaces (this field is independent of the axial coordinate, too).

The dielectric characteristics of the investigation domain S , in the lower half space, are described by the so-called *object function*, which is defined as

$$\tau(\mathbf{r}) = j\omega[\epsilon(\mathbf{r}) - \epsilon_b], \quad (1)$$

where $\epsilon(\mathbf{r})$ is the complex dielectric permittivity at point \mathbf{r} , and ϵ_b denotes the dielectric permittivity of the soil.

The investigation area is illuminated by V line-current sources, with angular frequency ω (in the following, the $e^{j\omega t}$ time dependence is assumed and omitted). A mixed illumination configuration (partially borehole and partially from the top), which allows direct comparisons with the results reported in [43], is exploited. Under such assumptions, also the scattered electric field is z -polarized and independent of z . Consequently, only the transverse plane can be considered for the imaging procedure.

The scattered electric field, $u_{\text{scatt}}^{(\nu)}$, $\nu = 1, \dots, V$, is collected for any incident wave in M measurement points $\mathbf{s}_m^{(\nu)}$, which constitute the so-called observation domain O . The dielectric properties of S can be related to the scattered field by means of the following set of nonlinear integral equations:

$$u_{\text{scatt}}^{(\nu)}(\mathbf{r}) = G_{\text{lower}}^{\text{upper}} \tau u_{\text{tot}}^{(\nu)}(\mathbf{r}), \quad \mathbf{r} \in O, \quad (2)$$

$$u_{\text{tot}}^{(\nu)}(\mathbf{r}) = u_{\text{inc}}^{(\nu)}(\mathbf{r}) + G_{\text{lower}}^{\text{lower}} \tau u_{\text{tot}}^{(\nu)}(\mathbf{r}), \quad \mathbf{r} \in S,$$

where $G_{\text{lower}}^{\text{upper}}(\cdot)(\mathbf{r}) = j\omega\mu_0 \int_S(\cdot)g_{\text{HS}}(\mathbf{r}, \mathbf{r}')d\mathbf{r}'$, $\mathbf{r} \in O$ and $G_{\text{lower}}^{\text{lower}}(\cdot)(\mathbf{r}) = j\omega\mu_0 \int_S(\cdot)g_{\text{HS}}(\mathbf{r}, \mathbf{r}')d\mathbf{r}'$, $\mathbf{r} \in S$ are the data and state operators, where g_{HS} is the half-space Green's function [43] (superscripts in the operators recall where they are calculated, whereas subscripts recall where they are integrated).

Equations (2) can be rewritten in a compact operator form as

$$\text{HS}(\mathbf{x}) = \mathbf{y}, \quad (3)$$

where $\mathbf{x} = [\tau \ u_{\text{tot}}^{(1)} \ \dots \ u_{\text{tot}}^{(V)}]^t$ is an array containing the values of the object function and of the total electric field inside the investigation area for any illumination. In (3), $\mathbf{y} = [u_{\text{scatt}}^{(1)} \ \dots \ u_{\text{scatt}}^{(V)} \ u_{\text{inc}}^{(1)} \ \dots \ u_{\text{inc}}^{(V)}]^t$ is an array containing the values of the scattered electric field acquired by the measurement probes in the upper half space and the values of the incident electric field inside the investigation area. The half-space operator HS can be expressed, according to (2), as

$$\text{HS}(\mathbf{x}) = \begin{bmatrix} G_{\text{lower}}^{\text{upper}} \tau u_{\text{tot}}^{(1)} \\ \vdots \\ G_{\text{lower}}^{\text{upper}} \tau u_{\text{tot}}^{(V)} \\ u_{\text{tot}}^{(1)} - G_{\text{lower}}^{\text{lower}} \tau u_{\text{tot}}^{(1)} \\ \vdots \\ u_{\text{tot}}^{(V)} - G_{\text{lower}}^{\text{lower}} \tau u_{\text{tot}}^{(V)} \end{bmatrix}. \quad (4)$$

As it is well known, the inverse problem (4) is non-linear and ill-posed. Consequently, nonlinear regularizing methods must be used.

3. Regularized Solution of (3)

Due to the mentioned ill posedness, (3) must be solved in a regularized sense. The inexact Newton regularizing scheme developed in [49, 50] is applied here. This method includes two nested loops, in which a linearization (with respect to the current solution guess \mathbf{x}_k) of the operator HS is constructed (*outer loop*) and solved by means of the truncated Landweber method (*inner loop*). Exactly as in [49], the algorithm performs the following steps.

- (1) For $k = 0$ (k denotes the outer iteration index), a starting guess \mathbf{x}_0 is chosen (initialization phase).
- (2) The following linearized version of equation is constructed

$$\text{HS}'_{\mathbf{x}_k} \mathbf{h} = \mathbf{y}_k, \quad (5)$$

where $\mathbf{h} = [h_\tau \ h_u^{(1)} \ \dots \ h_u^{(V)}]^t$, $\mathbf{y}_k = \mathbf{y} - \text{HS}(\mathbf{x}_k)$, and $\text{HS}'_{\mathbf{x}_k}$ is the Fréchet derivative of HS at point \mathbf{x}_k . A regularized solution $\hat{\mathbf{h}}_k$ to (5) is obtained by applying an iterative truncated Landweber algorithm, for which we have

$$\begin{aligned} \mathbf{h}_{k,0} &= \mathbf{0}, \\ \mathbf{h}_{k,l+1} &= \mathbf{h}_{k,l} - \gamma \text{HS}'_{\mathbf{x}_k}{}^* \left(\text{HS}'_{\mathbf{x}_k} \mathbf{h}_{k,l} - \mathbf{y}_k \right), \end{aligned} \quad (6)$$

where $\text{HS}'_{\mathbf{x}_k}{}^*$ is the adjoint operator of $\text{HS}'_{\mathbf{x}_k}$.

- (3) The current solution is updated by using the following relation:

$$\mathbf{x}_{k+1} = \mathbf{x}_k + \hat{\mathbf{h}}_k. \quad (7)$$

- (4) A predefined stopping rule is finally applied. If this criterion is not satisfied, a fixed maximum number of outer iterations, k_{\max} , is performed. In both cases, at any iteration, the procedure can be stopped, otherwise steps (2)–(4) are repeated.

It should be noted that step (2) is actually the inner loop of the algorithm, whereas steps (1)–(3) constitute the outer loop.

4. Numerical Results

The developed method has been tested by means of numerical simulations. The working frequency has been set equal to 300 MHz (i.e., similar to that used in ground penetrating radars). A homogeneous lossy soil characterized by a relative dielectric permittivity $\epsilon_{r_b} = 4$ and an electric conductivity $\sigma_b = 0.01$ S/m has been considered (in order to simulate a dry sandy soil [53]). Similar to [43], a mixed measurement configuration is assumed, where reflection and cross-borehole operating modes are mixed together in order to acquire as much information as possible. Correspondingly, the antennas are located at points (Cartesian coordinates)

$$\mathbf{r}_n^{\text{ant}} = \begin{cases} \left(-\frac{2}{3}\lambda_0, -\frac{4}{3}\lambda_0 + (n-1)\frac{2\lambda_0}{21} \right), & n = 1, \dots, 15, \\ \left(-\frac{2}{3}\lambda_0 + (n-15)\frac{2\lambda_0}{21}, 0 \right), & n = 16, \dots, 28, \\ \left(\frac{2}{3}\lambda_0, -(n-29)\frac{2\lambda_0}{21} \right), & n = 29, \dots, 43, \end{cases} \quad (8)$$

where λ_0 is the free-space wavelength in the upper medium. A subset of these antennas act both as transmitter (TX) and receiver (RX). When an antenna operates in TX mode, all the remaining ones collect the scattered electric field (i.e., they work in RX mode). Consequently, for every illumination, $M = 42$ field samples are collected. In particular, in the cases reported in the following, $V = 7$ antennas are used. They are located at positions denoted by the indexes given by $n = 7(\nu - 1) + 1$, $\nu = 1, \dots, V$.

The investigation area is a square domain of dimensions $\lambda_0 \times \lambda_0$, whose upper side coincides with the air-ground interface. In order to numerically solve the equations involved in the inverse-scattering problem, such domain has been discretized into $N = 20 \times 20$ square subdomains.

The scattered field values used as input data for the considered simulations have been numerically obtained by using a computational code based on the method of moments [54]. In order to avoid the so-called *inverse crime*, a finer discretization (such as the ratio of the cell dimensions in the direct and inverse problems is not an integer number) has been used for the computation of the synthetic data. Moreover, in order to simulate a more realistic scenario, a Gaussian noise with zero mean value and variance corresponding to a signal-to-noise ratio $\text{SNR} = 25$ dB has also been added to the computed data.

In all the simulations reported in this section, the initialization phase has been always performed by assuming an empty investigation domain in the lower half space. Consequently, in this phase, the object function is equal to zero, and the total electric field is assumed equal to the one transmitted in the lower half space.

The first reported case concerns the reconstruction of a single circular cylinder of radius $a = 0.2\lambda_0$ centered at $\mathbf{r}^{\text{obj}} = (0.2\lambda_0, -0.5\lambda_0)$. The dielectric properties of the cylinder are $\epsilon_{r_{\text{obj}}} = 5.6$ and $\sigma_{\text{obj}} = 0.01$ S/m. The parameters of the inexact Newton algorithm are the following: maximum number of inner iterations, $k_{\text{LW}_{\max}} = 30$; maximum number of outer iterations, $k_{\text{IN}_{\max}} = 100$. Figure 2 reports the behavior of two error parameters for different values of the number of outer iterations of the iterative procedure. In particular, the two parameters are defined as

$$\begin{aligned} r_{\text{data}} &= \frac{\|u^{\text{actual}} - u^{\text{calc}}\|_2}{\|u^{\text{actual}}\|_2}, \\ r_{\text{solution}} &= \frac{\|\tau^{\text{actual}} - \tau^{\text{rec}}\|_2}{\|\tau^{\text{actual}}\|_2}, \end{aligned} \quad (9)$$

with τ^{actual} and τ^{rec} being the actual and reconstructed permittivity distributions (at the current iteration) and u^{actual} and u^{calc} the measured and computed values of the electric field data (at the current iteration, too). As can be seen from Figure 2, the plot of the “residual” on the data (the error parameter r_{data}) decreases monotonically as expected. Moreover, the plot of the solution “residual” (the error parameter r_{solution}) shows a typical *semiconvergence* behavior, that is, after a certain value of the iteration number the reconstruction quality degrades [55, 56].

The final image of the distribution of the relative dielectric permittivity inside the investigation region (corresponding to the optimum iteration number) is shown in Figure 3. As can be seen, the method is able to correctly retrieve the dielectric profile of the investigation area. In particular, both the shape of the buried inclusion and the value of its dielectric permittivity are correctly identified.

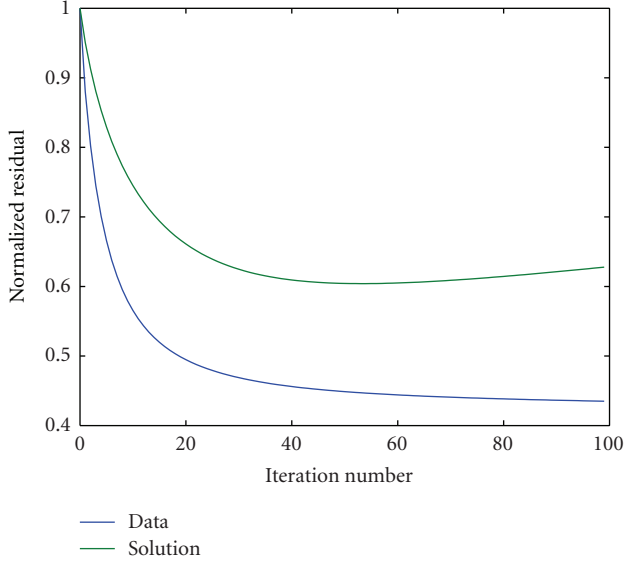


FIGURE 2: Data and solution residuals versus the outer iteration number (error parameters of (9)). Single circular cylinder buried in a lossy half space.

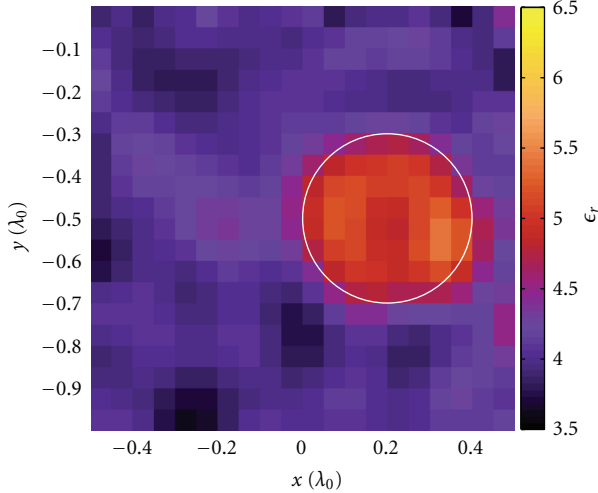


FIGURE 3: Reconstructed distribution of the relative dielectric permittivity. Single circular cylinder buried in a lossy half space.

For the present case, an analysis of the effects of the noise has also been performed. In particular, the mean relative error on the reconstruction, defined as the L_1 -norm

$$e = \frac{1}{N} \sum_{n=1}^N \frac{|\epsilon_n^{\text{actual}} - \epsilon_n^{\text{rec}}|}{|\epsilon_n^{\text{actual}}|} \quad (10)$$

has been calculated. In (10), $\epsilon_n^{\text{actual}}$ and ϵ_n^{rec} denote the values of the original and reconstructed complex permittivity inside the n th discretization subdomain of the investigation region. Moreover, the optimal value of the outer iteration have been evaluated, too. The obtained results are reported in Table 1.

As expected, as the noise level increases, the reconstruction “quality” decreases. However, even in presence of strong

TABLE 1: Mean relative errors and optimal iteration numbers versus the signal-to-noise ratio. Single circular cylinder buried in a lossy half space.

SNR	25	20	15	10
Mean relative error	0.065	0.078	0.085	0.12
Optimum outer iteration number	53	34	14	5

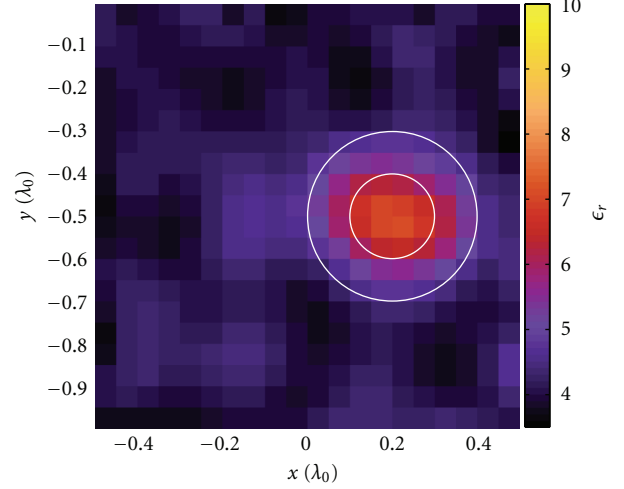


FIGURE 4: Reconstructed distribution of the relative dielectric permittivity. Double-layer circular cylinder buried in a lossy half space.

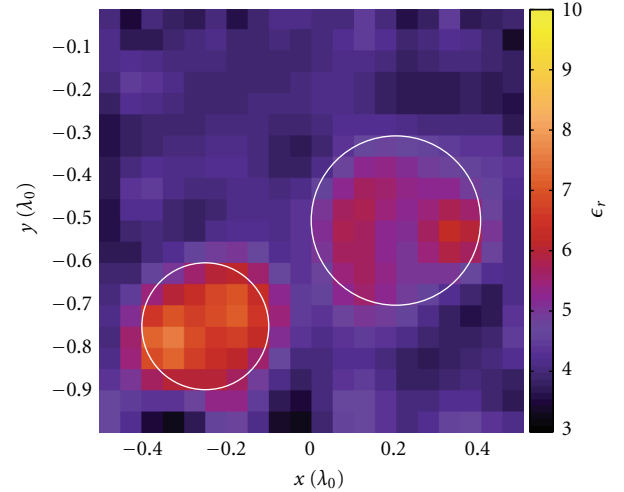


FIGURE 5: Reconstructed distribution of the relative dielectric permittivity. Two separate circular cylinders buried in a lossy half space.

noise levels, the method is able to yield rather good reconstructions (e.g., the error parameter e is equal to about 8% error for SNR = 15 dB).

In the second set of simulations, the reconstruction of a more complex configuration has been considered. In particular, the presence of a double-layer circular cylinder has been assumed. The outer layer has radius $a_1 = 0.2\lambda_0$ and is characterized by a relative dielectric permittivity $\epsilon_{r_1} = 5.6$ and an electric conductivity $\sigma_1 = 0.01$ S/m, whereas

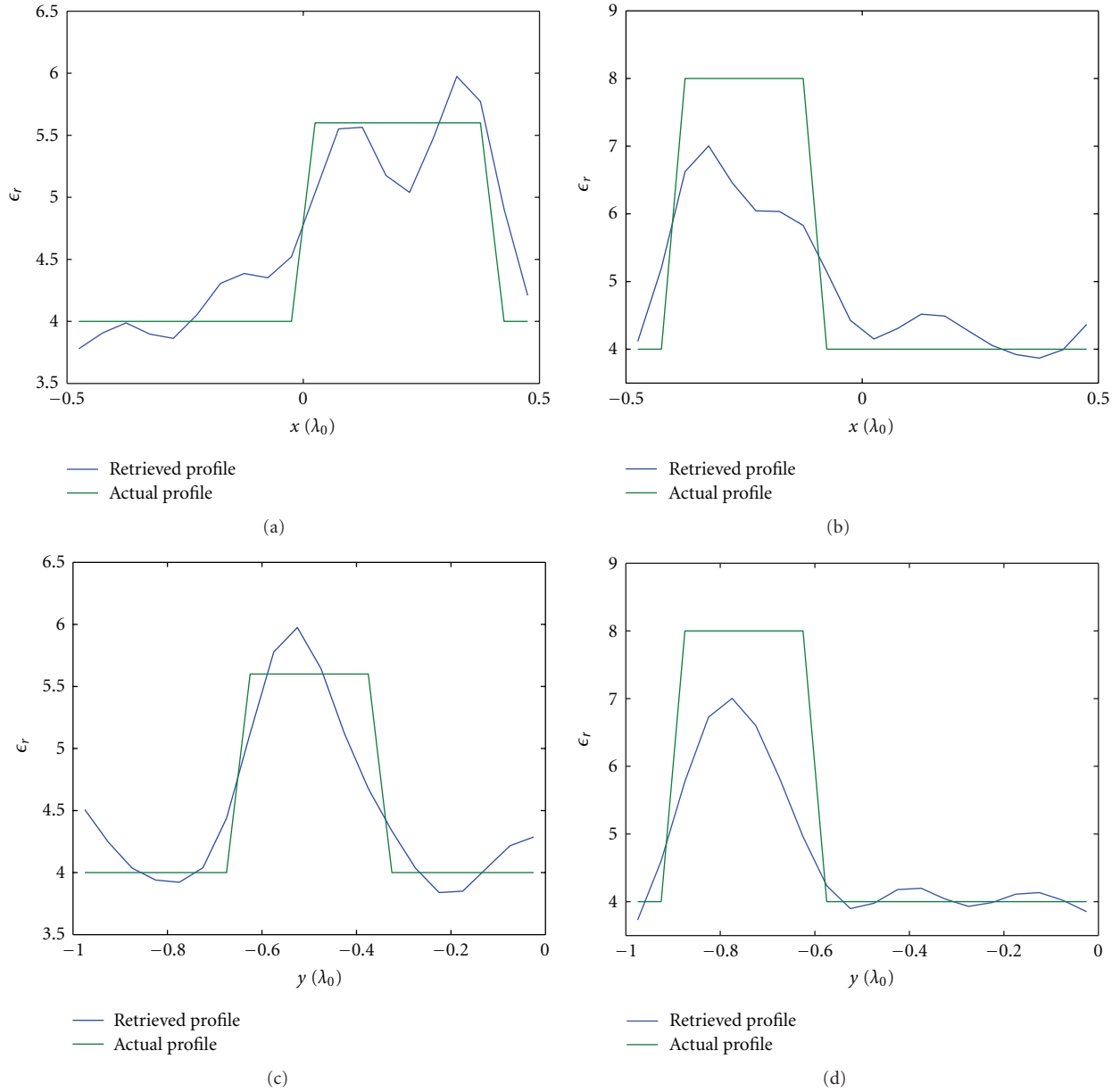


FIGURE 6: Horizontal cuts ((a) $y = -0.525\lambda_0$ and (b) $y = -0.775\lambda_0$) and vertical cuts ((c) $x = 0.325\lambda_0$ and (d) $x = -0.325\lambda_0$) of the reconstructed distribution of the relative dielectric permittivity (Figure 4). Two circular cylinders buried in a lossy half space.

the inner one has a radius $a_2 = 0.1\lambda_0$ and is characterized by a relative dielectric permittivity $\epsilon_{r_2} = 8$ and an electric conductivity $\sigma_2 = 0.01$ S/m. The object is centered at $\mathbf{r}^{\text{obj}} = (0.2\lambda_0, -0.5\lambda_0)$. The parameters of the inexact Newton method are the same as the ones adopted in the first case. The reconstructed distribution of the relative dielectric permittivity (final image) is shown in Figure 4. As can be seen, the object is correctly located, and the values of the dielectric properties are identified with a quite good accuracy.

Finally, the reconstruction of two separate circular cylinders have been considered. The radii of the two cylinders are $a_1 = 0.2\lambda_0$ and $a_2 = 0.15\lambda_0$. They are buried with

centers located at points $\mathbf{r}_1^{\text{obj}} = (0.2\lambda_0, -0.5\lambda_0)$ and $\mathbf{r}_2^{\text{obj}} = (-0.25\lambda_0, -0.75\lambda_0)$. The dielectric properties of the two scatterers are the following: $\epsilon_{r_1} = 5.6$, $\epsilon_{r_2} = 8$, and $\sigma_1 = \sigma_2 = 0.01$ S/m. The signal-to-noise ratio is $\text{SNR} = 25$ dB. The parameters of the iterative inversion algorithm are the same as in the previous cases. The reconstructed distribution of the relative dielectric permittivity is shown in Figure 5. This image corresponds to the optimal solution. As can be seen, also in this quite complex case, the method is able to correctly reconstruct the investigated scene. In particular, the two objects are clearly identified and separated. Moreover, both shapes and dielectric properties of the two targets are estimated with quite good accuracies

(although for the second cylinder the dielectric permittivity is slightly underestimated). In order to better assess the reconstruction accuracy, Figure 6 gives the profiles of the retrieved distribution of Figure 5 along some cuts parallel to the coordinate axes.

5. Conclusion

In this paper, a previously proposed approach for the imaging of buried objects has been extended to inspect strong scatterers, for which the exact nonlinear equations of the inverse scattering problem must be considered. The developed method is based on a two-step inexact Newton method, which allows us to obtain a regularized solution of the (discretized) integral equations relating the samples of scattered electric field collected in the upper half space to the distributions of the dielectric parameters inside the test domain located in the ground. The reported preliminary results of numerical simulations seem to indicate the validity of the proposed approach, which needs further evaluation assessments, including an experimental validation, which will be the subject of future research activity in this area.

References

- [1] T. J. Cui and W.C. Chew, "Inverse-scattering methods for three-dimensional targets buried in the lossy earth," in *Proceedings of the IEEE International Symposium on Antennas and Propagation*, vol. 3, pp. 1776–1779, 2000.
- [2] C. J. Lin and C. C. Chiu, "Inverse scattering of buried inhomogeneous dielectric material coated on a conductor," in *Proceedings of the 5th International Kharkov Symposium on Physics and Engineering of Microwaves, Millimeter, and Submillimeter Waves (MSMW '04)*, pp. 281–283, June 2004.
- [3] R. Persico, R. Bernini, and F. Soldovieri, "The role of the measurement configuration in inverse scattering from buried objects under the born approximation," *IEEE Transactions on Antennas and Propagation*, vol. 53, no. 6, pp. 1875–1887, 2005.
- [4] C. J. Lin and C. C. Chiu, "Inverse scattering of buried complex object by TE wave illumination," in *Proceedings of the IEEE International Symposium on Microwave, Antenna, Propagation and EMC Technologies for Wireless Communications (MAPE '05)*, pp. 784–787, August 2005.
- [5] A. N. Askarpour and R. Faraji-Dana, "Inverse scattering of 2-D dielectric objects buried in multilayer media using complex images green's function in born iteration method," in *Proceedings of the IEEE Antennas and Propagation Society International Symposium (APS '06)*, pp. 1085–1088, July 2006.
- [6] C. C. Chiu and Y. W. Kiang, "Electromagnetic inverse scattering of a conducting cylinder buried in a lossy half-space," *IEEE Transactions on Antennas and Propagation*, vol. 40, no. 12, pp. 1562–1563, 1992.
- [7] X. Chen, K. R. Shao, Y. Guo, J. Zhu, and J. D. Lavers, "A inverse scattering technique for objects buried in planar layered media based on an estimation of distribution algorithm," in *Proceedings of the 14th Biennial IEEE Conference on Electromagnetic Field Computation (CEFC '10)*, May 2010.
- [8] L. Crocco, M. D'Urso, and T. Isernia, "New models and tools for forward and inverse scattering from buried dielectric targets," in *Proceedings of the 10th International Conference Ground Penetrating Radar (GPR '04)*, pp. 59–62, June 2004.
- [9] K. Belkebir, R. E. Kleinman, and C. Pichot, "Microwave imaging—location and shape reconstruction from multi-frequency scattering data," *IEEE Transactions on Microwave Theory and Techniques*, vol. 45, no. 4, pp. 469–476, 1997.
- [10] L. Xu, S. K. Davis, S. C. Hagness, D. W. van der Weide, and B. D. Van Veen, "Microwave imaging via space-time beamforming: experimental investigation of tumor detection in multilayer breast phantoms," *IEEE Transactions on Microwave Theory and Techniques*, vol. 52, no. 8, pp. 1856–1865, 2004.
- [11] T. J. Cui, A. A. Aydiner, W. C. Chew, D. L. Wright, and D. V. Smith, "Three-dimensional imaging of buried objects in very lossy earth by inversion of VETEM data," *IEEE Transactions on Geoscience and Remote Sensing*, vol. 41, no. 10, pp. 2197–2210, 2003.
- [12] M. Lambert and D. Lesselier, "Binary-constrained inversion of a buried cylindrical obstacle from complete and phaseless magnetic fields," *Inverse Problems*, vol. 16, no. 3, pp. 563–576, 2000.
- [13] G. C. Giakos, M. Pastorino, F. Russo, S. Chiwdhury, N. Shah, and W. Davros, "Noninvasive imaging for the new century," *IEEE Instrumentation & Measurement Magazine*, vol. 2, pp. 32–35, 1999.
- [14] R. Zoughi, *Microwave Nondestructive Testing and Evaluation*, Kluwer Academic, Amsterdam, The Netherlands, 2000.
- [15] D. Lesselier and J. Bowler, "Foreword to the special section on electromagnetic and ultrasonic nondestructive evaluation," *Inverse Problems*, vol. 18, no. 6, pp. 1–2, 2002.
- [16] S. Kharkovsky and R. Zoughi, "Microwave and millimeter wave nondestructive testing and evaluation," *IEEE Instrumentation and Measurement Magazine*, vol. 10, no. 2, pp. 26–38, 2007.
- [17] C. C. Chen, J. T. Johnson, M. Sato, and A. G. Yarovoy, "Guest editorial foreword to the special issue on subsurface sensing using Ground-Penetrating Radar (GPR)," *IEEE Transactions on Geoscience and Remote Sensing*, vol. 45, no. 8, p. 2419, 2007.
- [18] O. Dorn and D. Lesselier, "Special issue on electromagnetic inverse problems: emerging methods and novel applications," *Inverse Problems*, vol. 26, no. 7, 2010.
- [19] A. Baussard, E. L. Miller, and D. Lesselier, "Adaptive multiscale reconstruction of buried objects," *Inverse Problems*, vol. 20, no. 6, supplement, pp. S1–S15, 2004.
- [20] A. Massa, M. Pastorino, and A. Randazzo, "Reconstruction of two-dimensional buried objects by a differential evolution method," *Inverse Problems*, vol. 20, no. 6, supplement, pp. S135–S150, 2004.
- [21] M. Pastorino, *Microwave Imaging*, John Wiley & Sons, Hoboken, NJ, USA, 2010.
- [22] C. H. Kuo and M. Moghaddam, "Electromagnetic scattering from a buried cylinder in layered media with rough interfaces," *IEEE Transactions on Antennas and Propagation*, vol. 54, no. 8, pp. 2392–2401, 2006.
- [23] A. Bréard, G. Perrusson, and D. Lesselier, "Hybrid differential evolution and retrieval of buried spheres in subsoil," *IEEE Geoscience and Remote Sensing Letters*, vol. 5, pp. 788–792, 2008.
- [24] A. Tabatabaenejad and M. Moghaddam, "Inversion of subsurface properties of layered dielectric structures with random slightly rough interfaces using the method of simulated annealing," *IEEE Transactions on Geoscience and Remote Sensing*, vol. 47, no. 7, pp. 2035–2046, 2009.
- [25] M. El-Shenawee, O. Dorn, and M. Moscoso, "An adjoint-field technique for shape reconstruction of 3-D penetrable object immersed in lossy medium," *IEEE Transactions on Antennas and Propagation*, vol. 57, no. 2, pp. 520–534, 2009.

- [26] P. M. Meaney, M. W. Fanning, D. Li, S. P. Poplack, and K. D. Paulsen, "A clinical prototype for active microwave imaging of the breast," *IEEE Transactions on Microwave Theory and Techniques*, vol. 48, no. 1, pp. 1841–1853, 2000.
- [27] G. Bozza, M. Brignone, and M. Pastorino, "Application of the no-sampling linear sampling method to breast cancer detection," *IEEE Transactions on Biomedical Engineering*, vol. 57, no. 10, pp. 2525–2534, 2010.
- [28] G. Bellizzi, O. Bucci, and I. Catapano, "Microwave cancer imaging exploiting magnetic nanoparticles as contrast agent," *IEEE Transactions on Biomedical Engineering*, vol. 58, pp. 2528–2536, 2011.
- [29] H. Harada, D. J. N. Wall, T. Takenaka, and M. Tanaka, "Conjugate gradient method applied to inverse scattering problem," *IEEE Transactions on Antennas and Propagation*, vol. 43, no. 8, pp. 784–792, 1995.
- [30] P. M. van den Berg and A. Abubakar, "Contrast source inversion method: state of art," *Journal of Electromagnetic Waves and Applications*, vol. 15, no. 11, pp. 1503–1505, 2001.
- [31] I. T. Rekanos, "Shape reconstruction of a perfectly conducting scatterer using differential evolution and particle swarm optimization," *IEEE Transactions on Geoscience and Remote Sensing*, vol. 46, no. 7, pp. 1967–1974, 2008.
- [32] A. Litman, D. Lesselier, and F. Santosa, "Reconstruction of a two-dimensional binary obstacle by controlled evolution of a level-set," *Inverse Problems*, vol. 14, no. 3, pp. 685–706, 1998.
- [33] R. Ferrayé, J. Y. Dauvignac, and C. Pichot, "Reconstruction of complex and multiple shape object contours using a level set method," *Journal of Electromagnetic Waves and Applications*, vol. 17, no. 2, pp. 153–181, 2003.
- [34] A. Abubakar and T. M. Habashy, "Constrained parametric minimization for the inversion of electromagnetic measurements in the earth," in *Proceedings of the Progress in Electromagnetics Research Symposium (PIERS '04)*, pp. 49–52, March 2004.
- [35] D. Colton, H. Haddar, and M. Piana, "The linear sampling method in inverse electromagnetic scattering theory," *Inverse Problems*, vol. 19, no. 6, supplement, pp. S105–S137, 2003.
- [36] L. Pan, X. Chen, Y. Zhong, and S. P. Yeo, "Comparison among the variants of subspace-based optimization method for addressing inverse scattering problems: transverse electric case," *Journal of the Optical Society of America A*, vol. 27, no. 10, pp. 2208–2215, 2010.
- [37] Y. Zhong, X. Chen, and K. Agarwal, "An improved subspace-based optimization method and its implementation in solving three-dimensional inverse problems," *IEEE Transactions on Geoscience and Remote Sensing*, vol. 48, no. 10, pp. 3763–3768, 2010.
- [38] J. De Zaeytijd, A. Franchois, C. Eyraud, and J. M. Geffrin, "Full-wave three-dimensional microwave imaging with a regularized Gauss-Newton method-theory and experiment," *IEEE Transactions on Antennas and Propagation*, vol. 55, no. 11, pp. 3279–3292, 2007.
- [39] C. Gilmore, P. Mojabi, and J. LoVetri, "Comparison of an enhanced distorted born iterative method and the multiplicative-regularized contrast source inversion method," *IEEE Transactions on Antennas and Propagation*, vol. 57, no. 8, pp. 2341–2351, 2009.
- [40] D. J. Daniels, *Ground Penetrating Radars*, IEE, London, UK, 2nd edition, 2004.
- [41] R. Mittra, M. Ji-Fu, and Y. Wenhua, "Identifying buried objects using the neural network approach," in *Proceedings of the IEEE Antennas and Propagation Society International Symposium*, pp. 2596–2599, 1999.
- [42] L. Crocco, G. Prisco, F. Soldovieri, and N. J. Cassidy, "Advanced forward modeling and tomographic inversion for leaking water pipes monitoring," in *Proceedings of the 4th International Workshop on Advanced Ground Penetrating Radar (IWAGPR '07)*, pp. 127–131, June 2007.
- [43] G. Bozza, C. Estatico, M. Pastorino, and A. Randazzo, "Application of an inexact-Newton method within the second-order Born approximation to buried objects," *IEEE Geoscience and Remote Sensing Letters*, vol. 4, no. 1, pp. 51–55, 2007.
- [44] R. Pierri and G. Leone, "Inverse scattering of dielectric cylinders by a second-order born approximation," *IEEE Transactions on Geoscience and Remote Sensing*, vol. 37, no. 1, pp. 374–382, 1999.
- [45] A. Brancaccio, V. Pascazio, and R. Pierri, "Quadratic model for inverse profiling: the one-dimensional case," *Journal of Electromagnetic Waves and Applications*, vol. 9, no. 5-6, pp. 673–696, 1995.
- [46] C. Estatico, M. Pastorino, and A. Randazzo, "An inexact-Newton method for short-range microwave imaging within the second-order born approximation," *IEEE Transactions on Geoscience and Remote Sensing*, vol. 43, no. 11, pp. 2593–2605, 2005.
- [47] S. Caorsi, A. Costa, and M. Pastorino, "Microwave imaging within the second-order born approximation: stochastic optimization by a genetic algorithm," *IEEE Transactions on Antennas and Propagation*, vol. 49, no. 1, pp. 22–31, 2001.
- [48] G. Bozza, C. Estatico, M. Pastorino, and A. Randazzo, "A regularization approach to microwave imaging under the second-order Born approximation with real data," in *Proceedings of the IEEE International Workshop on Imaging Systems and Techniques, Niagara Falls*, pp. 14–19, Ontario, Canada, May 2005.
- [49] G. Bozza, C. Estatico, M. Pastorino, and A. Randazzo, "An inexact Newton method for microwave reconstruction of strong scatterers," *IEEE Antennas and Wireless Propagation Letters*, vol. 5, no. 1, pp. 61–64, 2006.
- [50] G. Bozza, C. Estatico, A. Massa, M. Pastorino, and A. Randazzo, "Short-range image-based method for the inspection of strong scatterers using microwaves," *IEEE Transactions on Instrumentation and Measurement*, vol. 56, no. 4, pp. 1181–1188, 2007.
- [51] C. Estatico, G. Bozza, A. Massa, M. Pastorino, and A. Randazzo, "A two-step iterative inexact-Newton method for electromagnetic imaging of dielectric structures from real data," *Inverse Problems*, vol. 21, no. 6, supplement, pp. S81–S94, 2005.
- [52] G. Bozza and M. Pastorino, "An inexact Newton-based approach to microwave imaging within the contrast source formulation," *IEEE Transactions on Antennas and Propagation*, vol. 57, no. 4, pp. 1122–1132, 2009.
- [53] H. M. Jol, *Ground Penetrating Radar: Theory and Applications*, Elsevier Science, Oxford, UK, 2009.
- [54] J. H. Richmond, "Scattering by a dielectric cylinder of arbitrary cross shape," *IEEE Transactions on Antennas and Propagation*, vol. 13, pp. 334–341, 1965.
- [55] M. Bertero and P. Boccacci, *Introduction to Inverse Problems in Imaging*, IOP, Bristol, UK, 1998.
- [56] G. Bozza, C. Estatico, M. Pastorino, and A. Randazzo, "A numerical assessment of the semiconvergence behavior in an inverse-scattering approach to electromagnetic imaging," in *Proceedings of the IEEE Instrumentation and Measurement Technology Synergy of Science and Technology in Instrumentation and Measurement (IMTC '07)*, Warsaw, Poland, May 2007.

Research Article

Location and Shape Reconstruction of 2D Dielectric Objects by Means of a Closed-Form Method: Preliminary Experimental Results

Gian Luigi Gragnani and Maurizio Diaz Mendez

Diten, University of Genoa, Via Opera Pia 11A, 16145 Genoa, Italy

Correspondence should be addressed to Gian Luigi Gragnani, gianluigi.gragnani@unige.it

Received 30 March 2012; Accepted 31 May 2012

Academic Editor: Andrea Randazzo

Copyright © 2012 G. L. Gragnani and M. Diaz Mendez. This is an open access article distributed under the Creative Commons Attribution License, which permits unrestricted use, distribution, and reproduction in any medium, provided the original work is properly cited.

An analytical approach to location and shape reconstruction of dielectric scatterers, that was recently proposed, is tested against experimental data. Since the cross-sections of the scatterers do not depend on the z coordinate, a 2D problem can be formulated. A closed-form singular value decomposition of the scattering integral operator is derived and is used to determine the radiating components of the equivalent source density. This is a preliminary step toward a more complete solution, which will take into account the incident field inside the investigation domain in order to provide the dielectric features of the scatterer and also the nonradiating sources. Reconstructions of the equivalent sources, performed on some scattering data belonging to the Fresnel database, show the capabilities of the method and, thanks to the closed-form solution, results are obtained in a very short computation time.

1. Introduction

In the last decades, inverse electromagnetic scattering and near field imaging have been widely studied research topics [1]. Actually, electromagnetic imaging [2] is a very promising technique in many practical application fields. The more consolidated applications perhaps are those related to the use of ground penetrating radar, but a lot more are at present used or in advanced state of development. For example, it has been suggested that microwave imaging could be successfully used as a diagnostic technique in several areas, including civil and industrial engineering [3–5], nondestructive testing and evaluation [6–9], geophysical prospecting [10], and biomedical engineering [11–14]. Microwave imaging has also been proposed as a useful tool in wood industry [15]. Also, sophisticated techniques for plasma diagnostic can be based on microwave imaging [16]. Furthermore, inverse electromagnetic scattering can provide insights for approaching other problems of great interest

nowadays, for example, plasmonic cloaking and the synthesis of metamaterials [17].

One of the aim of an inverse electromagnetic-scattering imaging system is to find the actual position of a dielectric object inside a bounded space region, as well as its shape. The techniques applied are based on the use of a known incident field illuminating the space region containing the object. By suitably measuring the scattered field, a solution to the problem can be derived.

The main difficulties with solving an inverse electromagnetic-scattering problem result from its nonlinearity and instability. To overcome these negative features, in the scientific literature, several regularization techniques have been proposed. Furthermore, the a priori knowledge usually available could be included in the formulation of the resolving algorithm. The problem could be recast as a global nonlinear optimization problem, and stochastic, as well as deterministic approaches can be used to achieve a solution. The interested reader is referred, for example, to [18–22].

Another common technique to overcome nonlinearity is based on the transformation of the original problem into an inverse source one, by replacing the scatterer with an equivalent (induced) source. Although the equivalent source density linearizes the inverse scattering equation, the transformation of the inverse scattering problem into an inverse source one involves the solution of an integral equation of the first kind. Hence, the resulting operator is ill-posed, and its solution is usually unstable and nonunique [23]. In this particular case, nonuniqueness is due to the so-called nonradiating sources, that do not radiate outside their domain of definition and hence belong to the null space of the scattering operator [24].

In the present work, an approach to the inverse source problem that allows to clearly reformulate it in terms of both the radiating and nonradiating parts of the induced sources is used. Through a singular value decomposition (SVD) of the scattering operator, a closed-form solution to the radiating sources is reached. By using such a solution, an expression for the reconstructed scattered field inside the dielectric object can also be obtained in closed form.

While the theory that is at the base of this work was already presented and tested by numerical simulations [25, 26], the present paper is devoted to the reconstruction of the scattering properties from experimental data. Testing inversion algorithms against experimental data is a very important topic to deal with. Actually, since inverse scattering problems are ill-posed, their solutions are not as easy to be obtained as in the case of direct problems, and the risk in not validating an imaging algorithm with real world data is that the simulations could not take into account all the parameters involved in reality. Simulations can be made more and more complex, thanks to the availability of computers with continuously increasing power, however researchers must validate the model with experiments, refine it, and simulate and test again, and iteratively repeat the process until the model matches the physical data. Fortunately, in the last decade, some research groups have dealt with this lack of experimental data by performing measurements on a controlled environment and by making available the results to the inverse scattering community. The first available data were those of the so-called Ipswich database [27–30]. A larger collection of data, on both metallic and dielectric scatterers, is now available thanks to the efforts of the group at the Institut Fresnel, Marseille, France [31, 32]. In the present work, some of the data of the Fresnel database are used to test the inversion method. Since one of the interesting features of the Fresnel database is that data are provided over a wide band frequency range, also some comparisons about the behavior of the method at different frequencies have been carried out.

Although the present work is at an early stage and only some features of the theoretical model have been checked against the experimental data, the method seems to perform well, and its capabilities to reconstruct both the location and the shape of the induced sources are demonstrated. Furthermore, thanks to the closed-form formulation of the solution, results are available in a very short time that can allow for a quasi real-time imaging system.

2. Mathematical Background

In this section, the closed-form solution to the inverse scattering problem is briefly resumed. For more details the reader is referred to [25, 26].

2.1. The Electromagnetic Scattering. Let us consider an inhomogeneous object whose dielectric parameters are unknown, and which is irradiated by an electromagnetic field produced by a known source. The presence of the object leads to a total electromagnetic field that is different from the one that the same source would radiate in a free-space environment. In particular, the scattered field due to the object can be modeled by means of the volume equivalence theorem [33], that allows one to replace the dielectric object with an induced (or equivalent) source density, radiating in free space. So the object acts as a secondary source of radiated electromagnetic field. In three dimensions, the scattered field vector \mathbf{E}_s can be expressed as

$$\begin{aligned} \mathbf{E}_s(\mathbf{r}) &= \mathbf{E}_{\text{tot}}(\mathbf{r}) - \mathbf{E}_{\text{inc}}(\mathbf{r}) \\ &= \omega^2 \mu \varepsilon \iiint \mathbf{P}_{\text{eq}}^{\text{TOT}}(\mathbf{r}') \mathcal{G}(|\mathbf{r} - \mathbf{r}'|) d\mathbf{r}' \\ &\quad + \nabla \nabla \cdot \iiint \mathbf{P}_{\text{eq}}^{\text{TOT}}(\mathbf{r}') \mathcal{G}(|\mathbf{r} - \mathbf{r}'|) d\mathbf{r}', \end{aligned} \quad (1)$$

where

- (i) \mathbf{E}_{tot} is the total electrical field vector;
- (ii) \mathbf{E}_{inc} is the incident field vector, that is the known field that would be radiated without the object;
- (iii) $\mathbf{r} = \mathbf{r}(\rho, \vartheta, z)$ is the position vector of the observer;
- (iv) $\mathbf{r}' = \mathbf{r}'(\rho', \vartheta', z')$ is the position vector of any point of the scattering domain;
- (v) $\mathcal{G}(|\mathbf{r} - \mathbf{r}'|)$ is the Green's function for the electromagnetic radiation in free space;
- (vi) ε is the dielectric permittivity of the propagation medium;
- (vii) μ is the magnetic permeability of the propagation medium;
- (viii) $\mathbf{P}_{\text{eq}}^{\text{TOT}}$ is a polarization field that acts as an equivalent source for the scattered field.

Within the assumption of dealing with nonmagnetic media (i.e., $\mu = \mu_0$ both inside and outside the scatterers, μ_0 being the permeability in vacuo), we have [34]

$$\mathbf{P}_{\text{eq}}^{\text{TOT}}(\mathbf{r}) = \tau(\mathbf{r}) \mathbf{E}_{\text{tot}}(\mathbf{r}), \quad (2)$$

where

- (i) $\tau(\mathbf{r}) = (\varepsilon_r(\mathbf{r}) - 1)$ is called *scattering potential* and $\varepsilon_r(\mathbf{r})$ is the complex relative dielectric permittivity of the scatterer, with respect to the background permittivity ε .

2.2. 2D TM Model

The problem is simplified into a two-dimensional and scalar one, when

- (1) the scatterers are infinitely extended along z ;
- (2) the scattering potential does not depend on z ;
- (3) the incident electric field does not depend on z , is z directed, and propagates in a transverse direction (TM illumination).

In this case also the scattered field is directed along z and only the cross section with respect to z must be considered. The integral equation modeling the inverse scattering problem becomes [35]

$$\begin{aligned} E_s(\boldsymbol{\rho}) &= E_{\text{tot}}(\boldsymbol{\rho}) - E_{\text{inc}}(\boldsymbol{\rho}) \\ &= -j \frac{k^2}{4} \iint_{D_{\text{inv}}} \tau(\boldsymbol{\rho}') E_{\text{tot}}(\boldsymbol{\rho}') H_0^{(2)}(k|\boldsymbol{\rho} - \boldsymbol{\rho}'|) d\boldsymbol{\rho}', \end{aligned} \quad (3)$$

where, in a generic cross section of the object:

- (i) E_{tot} is the z component of the total electrical field;
- (ii) E_{inc} is the z component of the incident field;
- (iii) $\boldsymbol{\rho} = \boldsymbol{\rho}(\rho, \vartheta)$ is the position vector of the observer;
- (iv) $\boldsymbol{\rho}' = \boldsymbol{\rho}'(\rho', \vartheta')$ is the position vector of any point of the investigation domain D_{inv} ;
- (v) $H_0^{(2)}(k|\boldsymbol{\rho} - \boldsymbol{\rho}'|)$ is the second-kind and zeroth-order Hankel function;
- (vi) $k = \omega\sqrt{\mu\epsilon}$ is the wave number.

In the paper, it is assumed that scatterers are placed inside a circular region of radius R , along its circumference the scattered electromagnetic field is measured. The circular region defines the geometry of the problem and is called the domain of investigation D_{inv} , while the circle of sensors is called the domain of observation D_{obs} .

As it was already mentioned, the inverse problem given by (3) is nonlinear because such an equation contains the product of the total field $E_{\text{tot}}(\boldsymbol{\rho}')$ and the scattering potential $\tau(\boldsymbol{\rho}')$, both of which are unknown.

The problem can be linearized by using the equivalent source $P_{\text{eq}}^{\text{TOT}}$. It must be noticed that since in this way an equivalent inverse source problem is faced instead of an inverse scattering one, both the radiating and nonradiating contributions, P_{eq} and $P_{\text{eq}}^{\text{NR}}$, of the source should be accounted for. Hence $P_{\text{eq}}^{\text{TOT}}$ can be rewritten as

$$P_{\text{eq}}^{\text{TOT}}(\boldsymbol{\rho}') = \tau(\boldsymbol{\rho}') E_{\text{tot}}(\boldsymbol{\rho}') = P_{\text{eq}}(\boldsymbol{\rho}') + P_{\text{eq}}^{\text{NR}}(\boldsymbol{\rho}'), \quad \boldsymbol{\rho}' \in D_{\text{inv}} \quad (4)$$

and the inverse problem can be formulated as

$$E_s(\boldsymbol{\rho}) = -j \frac{k^2}{4} \iint_{D_{\text{inv}}} P_{\text{eq}}^{\text{TOT}}(\boldsymbol{\rho}') H_0^{(2)}(k|\boldsymbol{\rho} - \boldsymbol{\rho}'|) d\boldsymbol{\rho}'. \quad (5)$$

As compared to other nonlinear methods (see, e.g., [12, 13]) where there is no separation between radiating and nonradiating sources, in the present approach it is clearly identified which part of the reconstruction can be obtained by measurements. Further improvement can then only be obtained by means of the nonradiating sources and by using the constraint that (3) must hold also inside the investigation domain.

2.3. Radiating Source. The radiating part P_{eq} of the induced source can be computed after the derivation of the singular value decomposition of (5) and the definition of its singular system $\{w_\mu, \varphi_\mu; \sigma_\mu\}$. Detailed mathematical derivations can be found in [26]. In the present section, only the main results of the method are recalled.

For a lossless propagation medium, the singular system $\{w_\mu, \varphi_\mu; \sigma_\mu\}$ of (5) is

$$\begin{aligned} w_\mu(\vartheta) &= \frac{1}{\sqrt{2\pi R}} e^{j\mu\vartheta}, \\ \varphi_\mu(\rho, \vartheta) &= j \frac{1}{\sqrt{2\pi}} \frac{H_\mu^{(2)}(kR) J_\mu(k\rho)}{\left| H_\mu^{(2)}(kR) \right| \sqrt{(R^2/2) [J_\mu^2(kR) - J_{\mu+1}(kR) J_{\mu-1}(kR)]}} \\ &\quad \times e^{j\mu\vartheta}, \\ \sigma_\mu &= \frac{k^2 \pi \sqrt{R}}{2} \left| H_\mu^{(2)}(kR) \right| \\ &\quad \times \sqrt{\frac{R^2}{2} [J_\mu^2(kR) - J_{\mu+1}(kR) J_{\mu-1}(kR)]}, \end{aligned} \quad (6)$$

where

- (i) the functions $w_\mu(\vartheta)$ are the left singular functions of the decomposition;
- (ii) the functions $\varphi_\mu(\rho, \vartheta)$ are the right singular functions of the decomposition;
- (iii) the numbers σ_μ are the singular values,

and where $H_\mu^{(2)}$ and J_μ are the second-kind Hankel function of order μ and the first-kind Bessel function of order μ , respectively.

A solution to the radiating source contribution P_{eq} in term of singular system can be written as [36]

$$P_{\text{eq}}(\boldsymbol{\rho}) = \sum_{\mu=1}^{\infty} \frac{1}{\sigma_\mu} \varphi_\mu \int_0^{2\pi} E_{\text{scatt}} w_\mu^* R d\vartheta, \quad (7)$$

where the asterisk means complex conjugate. When the values given by (6) are substituted into (7), the following expression for the equivalent source is obtained:

$$\begin{aligned}
P_{\text{eq}}(\rho, \vartheta) &= \frac{2j}{k^2\pi} \\
&\times \sum_{\mu=-\infty}^{+\infty} c_{\mu} \frac{H_{\mu}^{(1)}(kR)}{\left|H_{\mu}^{(2)}(kR)\right|^2 (R^2/2) \left[J_{\mu}^2(kR) - J_{\mu+1}(kR)J_{\mu-1}(kR)\right]} \\
&\times J_{\mu}(k\rho) e^{j\mu\vartheta}, \tag{8}
\end{aligned}$$

where c_{μ} stand for the Fourier coefficients of $E_s(R, \vartheta)$ with respect to ϑ [26].

Since P_{eq} depends on the singular values of the scattering operator, care must be exercised in deriving an expression for the reconstructed radiating source. Actually, the nature of the involved integral equation is such that, in every case, after a certain index, the singular values sharply decrease and tend to zero. These small singular values increase the instability of the solution. In order to minimize such instability, only the singular values above a suitable threshold should be taken into account in the solution.

As for the nonradiating sources $P_{\text{eq}}^{\text{NR}}$, since they are not measurable, they are in general difficult to be reconstructed. In principle, their contributions could be found out by taking into account that they must be orthogonal to the radiating ones and do not radiate outside the domain of investigation, and by using some priors about the scatters. Some works trying to deal in a formal way with $P_{\text{eq}}^{\text{NR}}$ (see, e.g., [37, 38]) and, in particular, the method presented in [39] fits very well with the present closed-form approach. All these approaches, however, are computationally very expensive. In the most of the imaging systems, nonradiating currents are put to zero. This is a common assumption in the solution of this kind of inverse problems, and this is the line followed in the present paper, in order to have results in short time. Since the nonradiating sources contribute to the higher spatial frequencies, the price to pay for assuming $P_{\text{eq}}^{\text{NR}}$ negligible is usually a smoothing effect in the reconstruction, but the solution is anyway good enough for many purposes in electromagnetic imaging.

2.4. Scattered Field and Scattering Potential. By using the expression given by (8), approximate scattered fields both inside and outside the scatterer can be analytically obtained. Again, the approximation in deriving the scattered fields stands in using only radiating contribution of the sources, that is:

$$E_s(\rho) \approx -j \frac{k^2}{4} \int_{D_{\text{inv}}} P_{\text{eq}}(\rho') H_0^{(2)}(k|\rho - \rho'|) d\rho'. \tag{9}$$

And the scattering potential becomes

$$\begin{aligned}
\tau(\rho) &\approx \frac{P_{\text{eq}}(\rho)}{E_{\text{tot}}(\rho)} \\
&\approx \frac{P_{\text{eq}}(\rho)}{E_{\text{inc}}(\rho) - j(k^2/4) \int_{D_{\text{inv}}} P_{\text{eq}}(\rho') H_0^{(2)}(k|\rho - \rho'|) d\rho'}. \tag{10}
\end{aligned}$$

Also for these results, details about the closed-form derivation are given in [25, 26]. It should be however anticipated that, since the Fresnel database does not provide the values of the incident field inside the investigation domain, a direct implementation of (10) by using the experimental data is not possible. In some cases, the incident field inside D_{inv} has been inferred from the values in the measurement domain. However, in the present work, we have preferred to focus the attention on the reconstruction of P_{eq} , that is, anyway the first step of any inverse scattering process. It should be nevertheless noticed that reconstructing the scattering potential, not only can provide quantitative information, but also the qualitative information about the location and the shape of the scatterers is usually better than the one provided by the radiating equivalent source. Hence, attempting to reconstruct τ , by using the full procedures proposed in [26, 39], will be the core of future works involving experimental data.

3. Experimental Results

The method was tested against three sets of experimental data involving dielectric scatterers. In particular, the dielectric targets of the first Fresnel dataset [31] were considered, as well as the ‘‘FoamDieExt’’ of the second dataset [40]. Furthermore, although the method was not originally conceived to deal with conducting objects, a test was also performed by using the data of the U-shaped metallic scatterer present in the first dataset.

It should be pointed out that the present theory assumes that data are available over the full circumference. Instead, in any dataset, scattering field measures were taken over an arc of fixed radius with an angular span of only 240 degrees, whereas no data were available in the remaining 120 degrees. Hence, in order to compute the coefficients c_{μ} appearing in (8), scattering data were continued with zeros. Although this approach is not the best choice and could lead to some overshoot in the Fourier coefficients, it is the simplest one and proved sufficient to achieve reliable results in any testing case.

The tests were focused on the reconstruction of the radiating equivalent source, and, in particular, three parameters involved in the process were considered: the number of singular values used in computing P_{eq} , the operating frequency f , and the direction of arrival of the incident field ϑ_v . Furthermore, the capabilities of the method of dealing with multiview and multifrequency data were checked against some different strategies of combining the results.

Results are shown by means of normalized maps of the reconstructed domain. On the same maps also the shape and

the location of the scattering object are shown, in order to give an immediate feeling about the fairness of the result.

Although both [31, 40] suggest that the investigation domains can be restricted to a small square around a scatterer, this information is not used in the present work, and the whole circle bounded by the measurement circle is considered to belong to the investigated domain. However, to increase the legibility of the maps, only the square area of $30 \times 30 \text{ cm}^2$ around the scatterer is shown. Anyway, it should be stressed that the value of the reconstructed equivalent source outside this area is negligible in any case.

Thanks to the closed-form formulation of the solution, all the results were obtained in a very short computation time. In particular, on a single-core class PC, a single view reconstruction takes about 2s. Since no optimization of the code was performed, it is expected that this figure can become of magnitude smaller on a dedicated hardware with optimized code, hence allowing for a quasi real-time imaging system.

Since reconstructions are evaluated from the data collected by a single experiment, only a partial information is available at each view. Furthermore, inspections at different frequencies also provide different information. To enhance the overall result, three different possibilities were considered: summing the partial results over the different views at a fixed frequency, summing over the frequencies at a fixed view, and summing over both frequencies and views. These approaches are summarized by the expressions in (11), where the quantities P_F , P_V , and \mathcal{P}_{VF} are defined as

$$P_F = \sum_{v=1}^{N_v} \left| \tilde{P}_{\text{eq}}(f, \vartheta_v) \right|, \quad P_V = \sum_{f=1}^{N_f} \left| \tilde{P}_{\text{eq}}(f, \vartheta_v) \right|, \quad (11)$$

$$\mathcal{P}_{VF} = \sum_{f=1}^{N_f} P_f = \sum_{v=1}^{N_v} P_v,$$

and where the quantity $|\tilde{P}_{\text{eq}}(f, \vartheta_v)|$ is the map of the amplitude of the reconstructed equivalent source at frequency f and at view ϑ_v .

3.1. Single Circular Cylinder. The first results are about the inversion of the scattering data produced by a singular dielectric cylinder with a circular cross section of radius $a = 15 \text{ mm}$. According to [31], the relative dielectric constant is $\epsilon_r = 3 \pm 0.3$ and the center of the object is shifted, in one direction, of about 30 mm, with respect to the origin of the axes. Data are collected over a circle of radius $R = 0.76 \text{ m}$ and 48 samples per frequency are available.

A single-view, single-frequency reconstruction is shown in Figure 1. It was obtained at $\vartheta_v = 0$ and $f = 8 \text{ GHz}$, and using 8 singular values. The map clearly shows a radiating source in proximity of the true-scattering object, whose maximum value is centered at the side which gave the most significant contribution to the scattered field. Reconstructions obtained by using multiview and multiview-multifrequency gave encouraging results. In particular, in Figure 2 the quantity P_V computed at $f = 8 \text{ GHz}$ is shown. It can be seen that the circular shape of the object

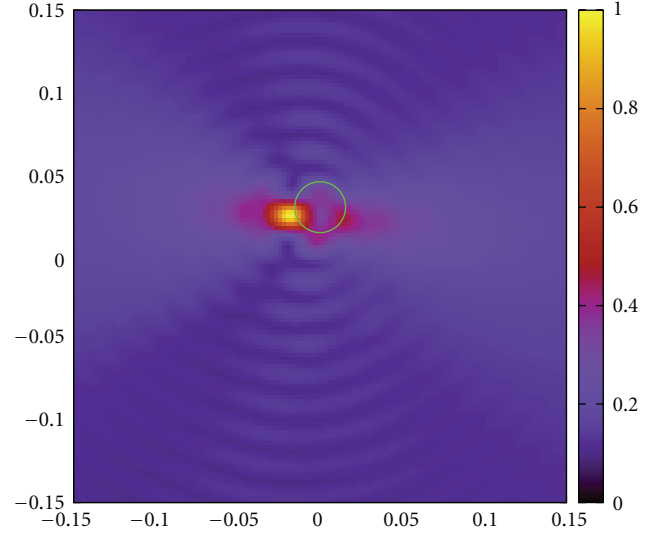


FIGURE 1: Reconstruction of the radiating source for a single dielectric cylinder. Single view $\vartheta_v = 0$ and single frequency $f = 8 \text{ GHz}$. 8 singular values were used.

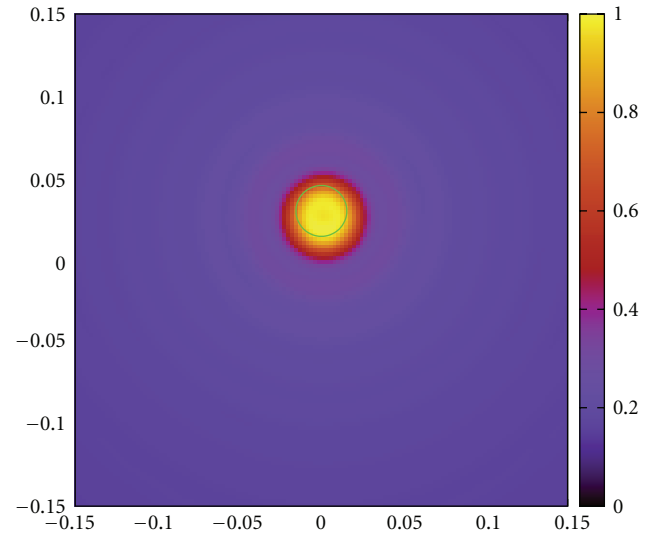


FIGURE 2: Reconstruction of a single dielectric cylinder. Multiview; map of the P_F values computed at $f = 8 \text{ GHz}$.

is clearly recognized, and also the maximum values of the reconstruction are contained inside the boundary of the true object.

The reconstruction using the multifrequency-multiview approach provided the result shown in Figure 3. Also in this case, the object is clearly reconstructed and, in comparison with Figure 2, the background is much more flat.

3.2. Pair of Circular Cylinders. This configuration was made by a couple of twin dielectric cylinders whose centers are spaced by 90 mm [31]. The dimensions of the cross-section and the dielectric constant of both cylinders were the same

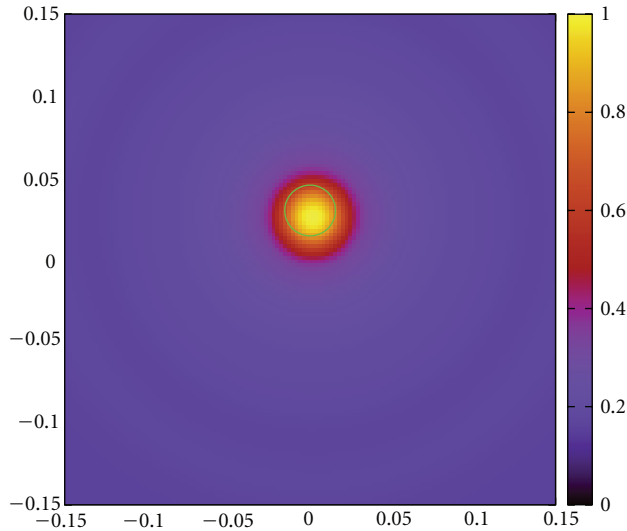


FIGURE 3: Reconstruction of a single dielectric cylinder. Multiview-multifrequency. Map of the \mathcal{P}_{VF} values.

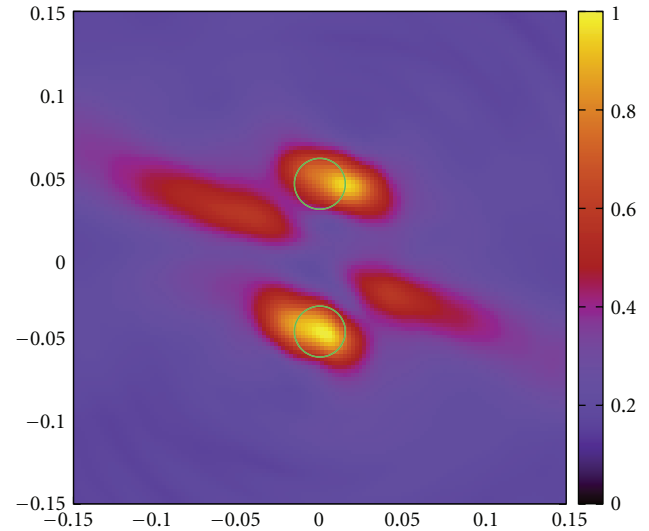


FIGURE 5: Reconstruction of a couple of twin dielectric cylinders. Multifrequency. Map of the P_V values computed at $\vartheta_v = 0$.

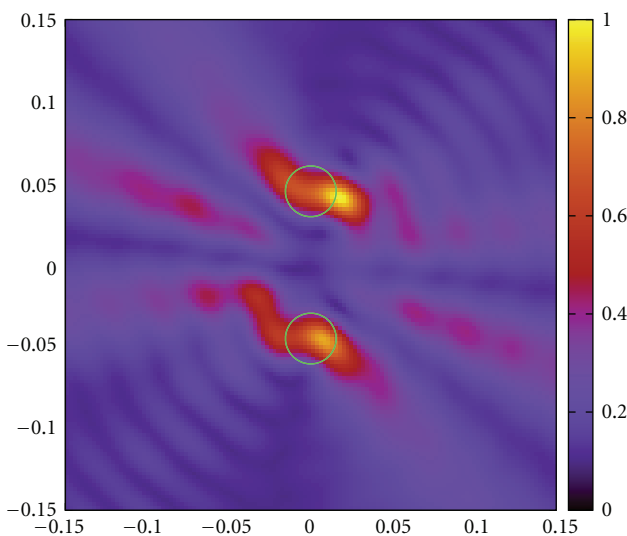


FIGURE 4: Reconstruction of the radiating source for a couple of twin dielectric cylinders. Single view $\vartheta_v = 0$ and single frequency $f = 8$ GHz. 8 singular values were used.

of the cylinder of the previous case, as well as they were the radius of the measurement region and the number of samples.

Single view reconstructions, at each frequency, clearly show the presence of two distinct objects. As an example, in Figure 4 the reconstruction at $\vartheta_v = 0$ and $f = 8$ GHz is shown. As in the previous example, 8 singular values were used. In Figure 5, instead, the multifrequency result, for the same illuminating angle $\vartheta_v = 0$, is shown. With respect to Figure 4, the object is better located and the background appears much more regular. However, also two spurious “scattering queues” are evident.

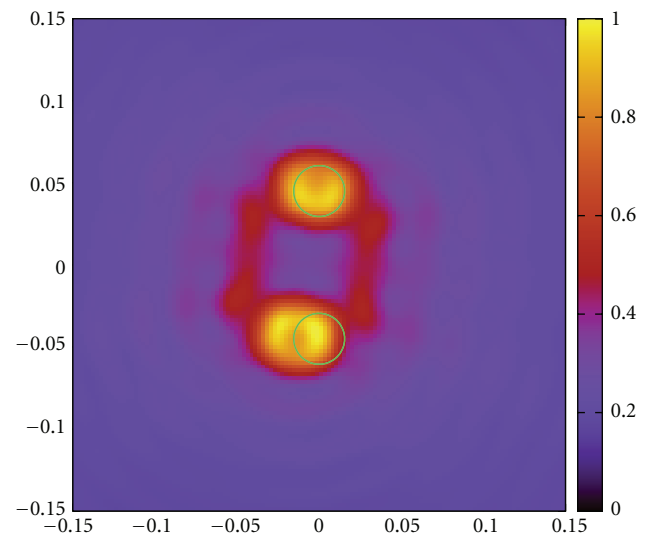


FIGURE 6: Reconstruction of a couple of twin dielectric cylinders. Multiview; map of the P_F values computed at $f = 8$ GHz.

Multiview reconstructions can provide a much more regular result, with a limited background noise. The case of $f = 8$ GHz is shown in Figure 6.

Finally, in Figure 7, the result given by the multiview-multifrequency method is shown. As it was in the case of a single cylinder, once again the combination of the results in frequency can provide a much better background.

3.3. Foam and Plastic Object. The third considered scatterer was the “FoamDielExt” object, included in the second Fresnel dataset [40]. The scatterer was made by two tangent cylinders with circular cross sections; one cylinder (radius $r_1 = 15.5$ mm) was plastic, with $\epsilon_{r,1} = 3 \pm 0.3$, while the

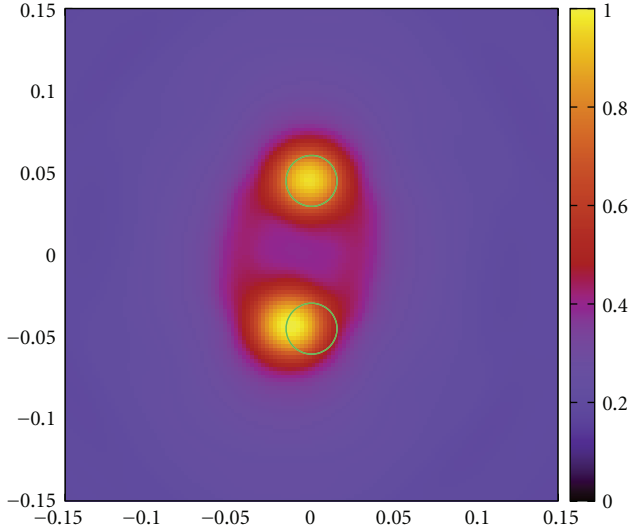


FIGURE 7: Reconstruction of a couple of twin dielectric cylinders. Multiview-multifrequency. Map of the \mathcal{P}_{VF} values.

other one (radius $r_2 = 40$ mm) was made of a foam having $\epsilon_{r,2} = 1.45 \pm 0.15$. The radius of the observation domain was $R = 1.67$ m and 240 samples were available at each frequency.

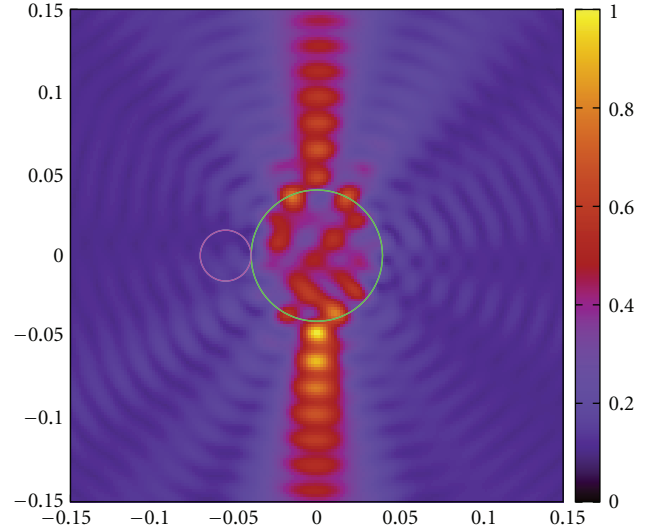
For this case, an accurate investigation about the right number of singular values was needed to achieve a good reconstruction. As an example, the limiting values of 8 and 210 singular values are considered, respectively, in Figures 8(a) and 8(b). It can be seen that, by using a small number of singular values, the scattering from the foam cylinder is much more clear and sharp than in the case of 210 singular values. However, when only 8 singular values are used, information about the dielectric cylinder gets mostly lost and hence a trade-off is in order. Actually, depending on the frequency, a variable number of singular values, ranging from 35 to 350 were used for achieving the best results.

Another example of reconstruction is given in Figure 9, where the multiview map at $f = 4$ GHz is shown. In this case, 140 singular values were used to achieve the better result. It can be seen that the different scattering given by the foam and by the plastic parts of the object can be clearly appreciated.

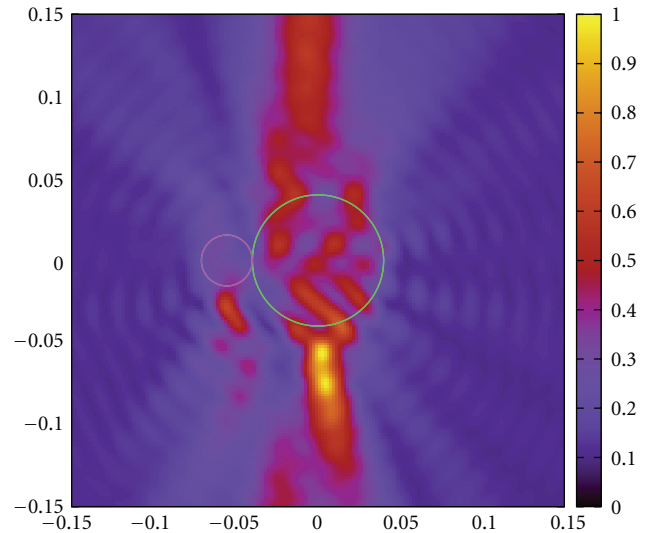
A further enhancement, with a pretty nice contrast between the two scattering cylinders, is achieved when results are combined also in frequency. The related map is shown in Figure 10.

3.4. Metallic Object. The metallic object was an U-shaped cylinder, having a cross-section with dimensions 80×50 mm², and the thickness of the metal was 5 mm [31]. Also in this case the analytical method is capable of recovering the presence of the target in the investigation domain, and a rectangular shape can be clearly recognized, when the various views are combined, especially at the higher frequencies.

Information provided by multifrequency can give a sharp reconstruction of a partial object, as it is shown in Figures 11 and 12, but fail to give a reconstruction of the whole object.



(a)



(b)

FIGURE 8: Reconstructions of the radiating source for the FoamDielExt object. Single view $\vartheta_v = 90^\circ$ and single frequency $f = 10$ GHz. (a) 8 singular values were used. (b) 210 singular values were used.

As already mentioned, instead, multiview gives a much more better overall result. In particular, in Figure 13, the map of the multiview result, computed at $f = 16$ GHz, is shown. Although some resonances seem to appear inside the U, it can be seen that the object can be recognized without any doubt, and it is worth noting that the open side is very different from the other sides.

As it was in the cases of dielectric objects, the multiview-multifrequency approach can smooth the noise in the background. However, in this case, the results is not as good as it was for dielectric objects and the true object is smoothed, too. This result is shown in Figure 14.

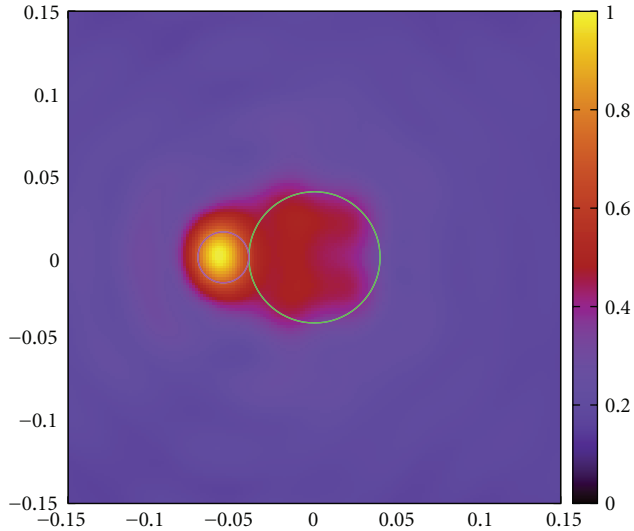


FIGURE 9: Reconstruction of a couple of the FoamDielExt object. Multiview; map of the P_F values computed at $f = 4$ GHz. At this frequency 140 singular values were used.

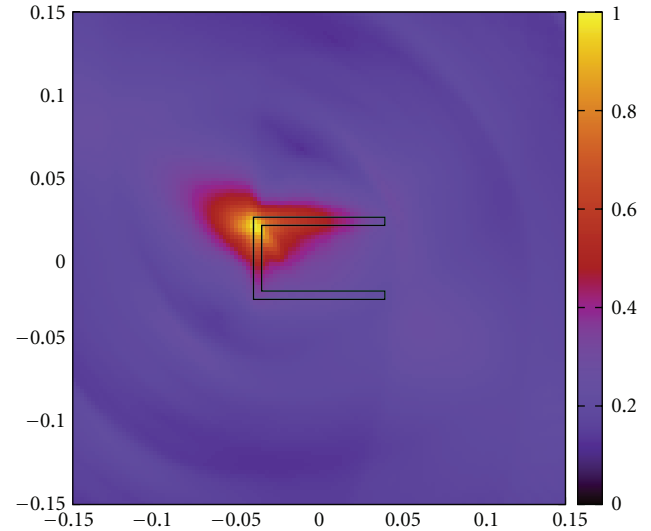


FIGURE 11: Reconstruction of a metallic U-shaped cylinder. Multi-frequency; map of the P_V values computed at $\vartheta_v = 160^\circ$.

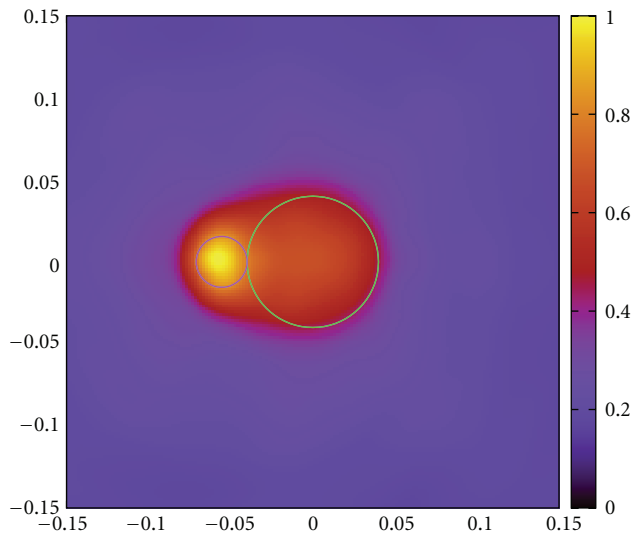


FIGURE 10: Reconstruction of a couple of twin dielectric cylinders. Multiview-multifrequency. Map of the \mathcal{P}_{VF} values.

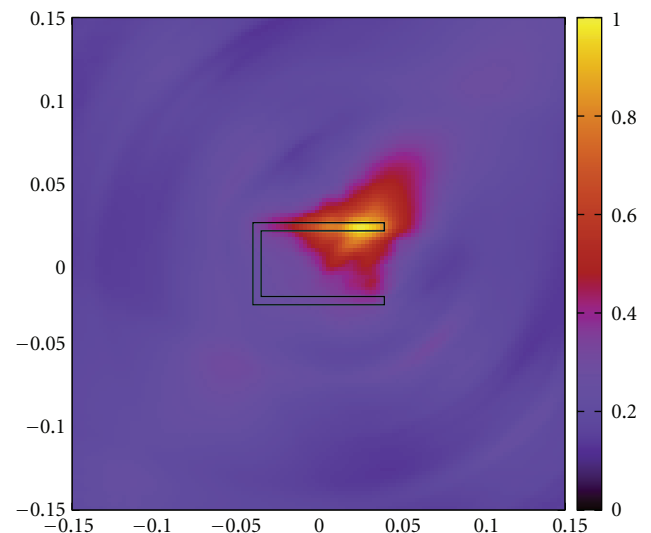


FIGURE 12: Reconstruction of a metallic U-shaped cylinder. Multi-frequency; map of the P_V values computed at $\vartheta_v = 60^\circ$.

4. Conclusions

In this work, an analytical method for inverse scattering problems was used to successfully reconstruct both homogeneous and inhomogeneous targets from multifrequency multistatic experimental data. The proposed method uses the singular values decomposition of the scattering operator to achieve a closed solution to the integral equation of the electromagnetic scattering. The derivation of the radiating source density inside the domain of investigation is the first step of the work, as well as the preliminary result useful to locate a scattering object inside such a region.

The dependence of the reconstructions on various parameters was investigated. In particular, results have shown that a correct choice of the significant number of singular values in the solution can lead to an optimal reconstruction, however; the method has proved robust enough to provide good reconstructions for a wide range of parameters.

Dielectric objects as well as objects made of conductive material were successfully tested.

As a general comment it should be stressed that the algorithm is very robust, and that, even for the very large domains used and with a suboptimal number of singular values, the object location was always clearly recovered.

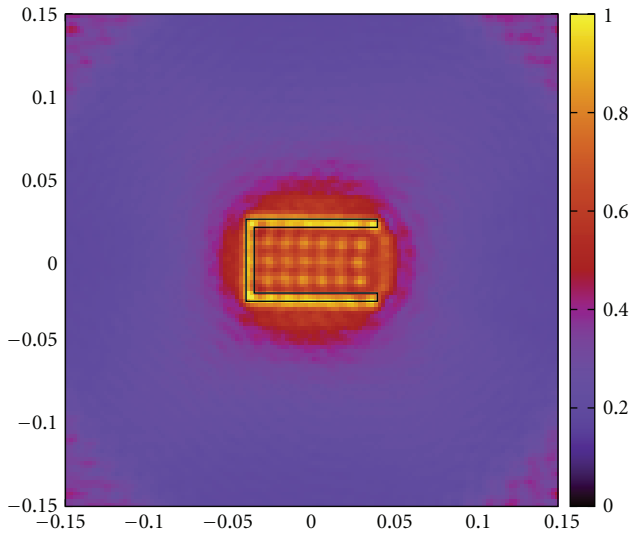


FIGURE 13: Reconstruction of a metallic U-shaped cylinder. Multi-view; map of the P_F values computed at $f = 16$ GHz.

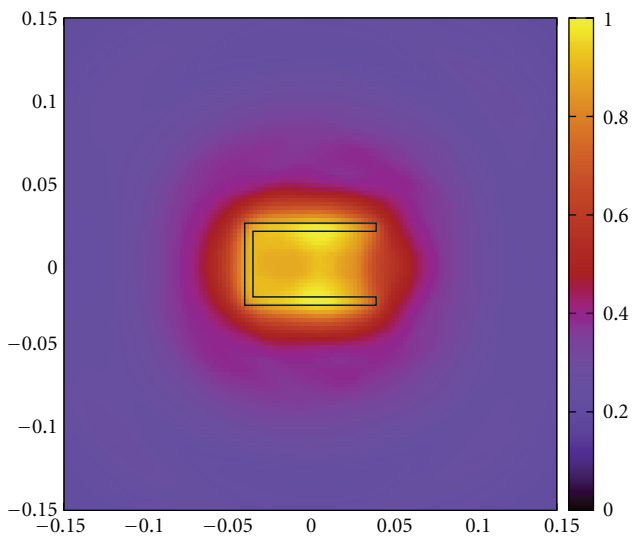


FIGURE 14: Reconstruction of the shape of a metallic U-shaped cylinder. Multiview-multifrequency. Map of the \mathcal{P}_{VF} values.

Furthermore, thanks to the closed-form formulation of the solution, all the results were obtained in a very short computation time. It must also be pointed out, in particular, that, once the operating frequency and the dimensions of the investigation domain have been chosen, the singular system of the problem can be computed “offline.” For the same reason also some other operations, for example, the inspection of the singular values, can be performed before the reconstruction process. As for the “online” part of the algorithm, also in this case things go very fast. As an extra bonus, since the closed-form virtually provides the solution at any point inside the investigation domain, high resolution maps of the reconstructed area can be obtained, without the constraints on grid dimensions and on the number of

pixels usually imposed by algorithms based on numerical discretization of the problem.

Future work will be focused on the reconstruction of the scattering potential of the objects under test and on the possible use of a set of nonradiating sources to refine the results. It is expected that these steps can provide a notable enhancement in the results, as it was already proved by numerical simulations.

A further goal will be also testing the method on other experimental datasets, for example, on the series provided by the University of Manitoba [41].

References

- [1] J. C. Bolomey and L. Jofre, “Three decades of active microwave imaging achievements, difficulties and future challenges,” in *Proceedings of the IEEE International Conference on Wireless Information Technology and Systems (ICWITS '10)*, pp. 1–4, Honolulu, Hawaii, USA, September 2010.
- [2] M. Pastorino, *Microwave Imaging*, John Wiley & Sons, New York, NY, USA, 2010.
- [3] Y. J. Kim, L. Jofre, F. De Flaviis, and M. Q. Feng, “Microwave reflection tomographic array for damage detection of civil structures,” *IEEE Transactions on Antennas and Propagation*, vol. 51, no. 11, pp. 3022–3032, 2003.
- [4] K. J. Langenberg, K. Mayer, and R. Marklein, “Nondestructive testing of concrete with electromagnetic and elastic waves: modeling and imaging,” *Cement and Concrete Composites*, vol. 28, no. 4, pp. 370–383, 2006.
- [5] M. Benedetti, M. Donelli, A. Martini, M. Pastorino, A. Rosani, and A. Massa, “An innovative microwave-imaging technique for nondestructive evaluation: applications to civil structures monitoring and biological bodies inspection,” *IEEE Transactions on Instrumentation and Measurement*, vol. 55, no. 6, pp. 1878–1884, 2006.
- [6] N. Qaddoumi, R. Zoughi, and G. W. Carriveau, “Microwave detection and depth determination of disbands in low-permittivity and low-loss thick sandwich composites,” *Re-earch in Nondestructive Evaluation*, vol. 8, no. 1, pp. 51–63, 1996.
- [7] S. Kharkovsky and R. Zoughi, “Microwave and millimeter wave nondestructive testing and evaluation,” *IEEE Instrumentation and Measurement Magazine*, vol. 10, no. 2, pp. 26–38, 2007.
- [8] R. Zoughi and S. Kharkovsky, “Microwave and millimetre wave sensors for crack detection,” *Fatigue and Fracture of Engineering Materials and Structures*, vol. 31, no. 8, pp. 695–713, 2008.
- [9] Y. Deng and X. Liu, “Electromagnetic imaging methods for nondestructive evaluation applications,” *Sensors*, vol. 11, pp. 11774–11808, 2011.
- [10] M. Pastorino, “Recent inversion procedures for microwave imaging in biomedical, subsurface detection and nondestructive evaluation applications,” *Measurement*, vol. 36, no. 3–4, pp. 257–269, 2004.
- [11] M. Bertero and M. Piana, “Inverse problems in biomedical imaging: modeling and methods of solution,” in *Complex Systems in Biomedicine*, A. Quarteroni, L. Formaggia, and A. Veneziani, Eds., pp. 1–33, Springer, Milan, Italy, 2006.
- [12] S. C. Hagness, “Microwave imaging in medicine: promises and future challenges,” in *Proceedings of the URSI General Assembly*, pp. 7–16, Chicago, Ill, USA, August 2008.

- [13] S. Semenov, "Microwave tomography: review of the progress towards clinical applications," *Philosophical Transactions of the Royal Society A*, vol. 367, no. 1900, pp. 3021–3042, 2009.
- [14] P. M. Meaney and K. D. Paulsen, "Challenges on microwave imaging supported by clinical results," in *Proceedings of the International Workshop on Biological Effects of Electromagnetic Fields*, pp. 10–14, Bodrum, Turkey, October 2010.
- [15] A. Salvadè, M. Pastorino, R. Monleone et al., "Microwave imaging of foreign bodies inside wood trunks," in *Proceedings of the IEEE Workshop on Imaging Systems and Techniques (IST '08)*, pp. 88–93, Chania, Greece, September 2008.
- [16] H. Park, C. C. Chang, B. Deng et al., "Recent advancements in microwave imaging plasma diagnostics," *Review of Scientific Instruments*, vol. 74, pp. 4239–4262, 2003.
- [17] A. Alu and N. Engheta, "Plasmonic and metamaterial cloaking: physical mechanisms and potentials," *Journal of Optics A*, vol. 10, no. 9, Article ID 093002, 2008.
- [18] S. Caorsi, A. Costa, and M. Pastorino, "Microwave imaging within the second-order born approximation: stochastic optimization by a genetic algorithm," *IEEE Transactions on Antennas and Propagation*, vol. 49, no. 1, pp. 22–31, 2001.
- [19] M. Benedetti, M. Donelli, G. Franceschini, M. Pastorino, and A. Massa, "Effective exploitation of the a priori information through a microwave imaging procedure based on the SMW for NDE/NDT applications," *IEEE Transactions on Geoscience and Remote Sensing*, vol. 43, no. 11, pp. 2584–2592, 2005.
- [20] G. Bozza, C. Estatico, M. Pastorino, and A. Randazzo, "Application of an inexact-Newton method within the second-order Born approximation to buried objects," *IEEE Geoscience and Remote Sensing Letters*, vol. 4, no. 1, pp. 51–55, 2007.
- [21] G. Bozza, C. Estatico, A. Massa, M. Pastorino, and A. Randazzo, "Short-range image-based method for the inspection of strong scatterers using microwaves," *IEEE Transactions on Instrumentation and Measurement*, vol. 56, no. 4, pp. 1181–1188, 2007.
- [22] A. Randazzo and C. Estatico, "A regularisation scheme for electromagnetic inverse problems: application to crack detection in civil structures," *Nondestructive Testing and Evaluation*. In press.
- [23] B. Hofmann, *On Ill-Posedness and Local Ill-Posedness of Operator Equations in Hilbert Spaces*, Chemnitz University of Technology, 1997.
- [24] A. J. Devaney and G. C. Sherman, "Nonuniqueness in inverse source and scattering problems," *IEEE Transactions on Antennas and Propagation*, vol. 30, pp. 1034–1042, 1982.
- [25] M. Chiappe and G. L. Gragnani, "An analytical approach to the reconstruction of the radiating currents in inverse electromagnetic scattering," *Microwave and Optical Technology Letters*, vol. 49, no. 2, pp. 354–360, 2007.
- [26] G. L. Gragnani, "Shape reconstruction of 2-D dielectric objects by an analytical method," *International Journal of Signal and Imaging Systems Engineering*, vol. 3, no. 2, pp. 81–92, 2010.
- [27] R. V. McGahan and R. E. Kleinman, "Special session on image reconstruction using real data," *IEEE Antennas and Propagation Magazine*, vol. 38, no. 3, pp. 39–40, 1996.
- [28] R. V. McGahan and R. E. Kleinman, "Second annual special session on image reconstruction using real data," *IEEE Antennas and Propagation Magazine*, vol. 39, no. 2, pp. 7–9, 1997.
- [29] R. V. McGahan and R. E. Kleinman, "The third annual special session on image reconstruction using real data, Part 1," *IEEE Antennas and Propagation Magazine*, vol. 41, no. 1, pp. 34–51, 1999.
- [30] R. V. McGahan and R. E. Kleinman, "The third annual special session on image reconstruction using real data Part 2," *IEEE Antennas and Propagation Magazine*, vol. 41, no. 1, pp. 20–40, 1999.
- [31] K. Belkebir and M. Saillard, "Special section: testing inversion algorithms against experimental data," *Inverse Problems*, vol. 17, no. 6, pp. 1565–1571, 2001.
- [32] K. Belkebir and M. Saillard, "Testing inversion algorithms against experimental data: inhomogeneous targets," *Inverse Problems*, vol. 21, pp. S1–S3, 2005.
- [33] C. A. Balanis, *Advanced Engineering Electromagnetics*, John Wiley & Sons, New York, NY, USA, 1989.
- [34] D. E. Livesay and K. M. Chen, "Electromagnetic field induced inside arbitrarily shaped biological bodies," *IEEE Transactions on Microwave Theory and Techniques*, vol. 22, no. 12, pp. 1273–80, 1974.
- [35] S. Caorsi, A. Frattoni, G. L. Gragnani, E. Nortino, and M. Pastorino, "Numerical algorithm for dielectric-permittivity microwave imaging of inhomogeneous biological bodies," *Medical and Biological Engineering and Computing*, vol. 29, no. 6, pp. NS37–NS38, 1991.
- [36] D. G. Dudley, T. M. Habashy, and E. Wolf, "Linear inverse problems in wave motion: nonsymmetric first-kind integral equations," *IEEE Transactions on Antennas and Propagation*, vol. 48, no. 10, pp. 1607–1617, 2000.
- [37] A. Gamliel, K. Kim, A. I. Nachman, and E. Wolf, "A new method for specifying nonradiating, monochromatic, scalar sources and their fields," *Journal of the Optical Society of America*, vol. 6, no. 9, pp. 1388–1393, 1989.
- [38] E. Wallacher and A. K. Louis, "Complete sets of radiating and nonradiating parts of a source and their fields with applications in inverse scattering limited-angle problems," *International Journal of Biomedical Imaging*, vol. 2006, Article ID 93074, 2006.
- [39] G. L. Gragnani and M. DiazMendez, "Improved electromagnetic inverse scattering procedure using non-radiating sources and scattering support reconstruction," *IET Microwaves Antennas & Propagation*, vol. 5, no. 15, pp. 1822–1829, 2011.
- [40] J.-M. Geffrin, P. Sabouroux, and C. Eyraud, "Free space experimental scattering database continuation: experimental set-up and measurement precision," *Inverse Problems*, vol. 21, no. 6, pp. S117–S130, 2005.
- [41] C. Gilmore, A. Zakaria, P. Mojabi, M. Ostadrahimi, S. Pistorius, and J. LoVetri, "The University of Manitoba Microwave Imaging Repository: a two-dimensional microwave scattering database for testing inversion and calibration algorithms," *IEEE Antennas and Propagation Magazine*, vol. 53, no. 5, pp. 126–133, 2011.